

MINISTÉRIO DA EDUCAÇÃO
UNIVERSIDADE FEDERAL DO RIO GRANDE DO SUL
PROGRAMA DE PÓS-GRADUAÇÃO EM ENGENHARIA MECÂNICA

NUMERICAL STUDY OF PREMIXED FLAME STABILIZATION WITHIN POROUS
INERT MEDIA EMPLOYING THE FLAMELET GENERATED MANIFOLD
TECHNIQUE

por

André Carlos Contini

Tese para obtenção do Título de
Doutor em Engenharia

Porto Alegre, Dezembro de 2021

NUMERICAL STUDY OF PREMIXED FLAME STABILIZATION WITHIN POROUS
INERT MEDIA EMPLOYING THE FLAMELET GENERATED MANIFOLD
TECHNIQUE

por

André Carlos Contini
Mestre em Engenharia Metalúrgica

Tese submetida ao Corpo Docente do Programa de Pós-Graduação em Engenharia Mecânica,
PROMEC, da Escola de Engenharia da Universidade Federal do Rio Grande do Sul, como
parte dos requisitos necessários para a obtenção do Título de

Doutor em Engenharia

Área de Concentração: Fenômenos de Transporte

Orientador: Prof. Dr. Fernando Marcelo Pereira

Aprovada por:

Prof. Dr. Rafael de Camargo Catapan POS-ECM / UFSC

Prof. Dra. Thamy Hayashi DEMEC / UFRGS

Prof. Dr. Felipe Roman Centeno PROMEC / UFRGS

Prof. Dr. Fernando Marcelo Pereira
Coordenador do PROMEC

Porto Alegre, 14 de Dezembro de 2021

À minha linda mulher Camila.

À minha mãe Ana e às minhas irmãs Caroline e Juliane.

AGRADECIMENTOS

Gostaria de agradecer ao meu orientador Dr. Fernando Marcelo Pereira pela excelente orientação e por sempre estar disposto a me ajudar a melhorar profissionalmente.

Gostaria de agradecer a minha companheira de aventuras/esposa/melhor amiga, Camila Miguel, por sempre me apoiar na direção dos meus sonhos.

Agradeço a minha mãe por me ensinar sempre pelo exemplo. Ela é a pessoa mais bondosa e batalhadora que já conheci. Agradecer as minhas duas irmãs (Juliane e Caroline) que sempre me apoiaram incondicionalmente em todas dificuldades.

Agradeço aos meus colegas do numérico Cristian, Leonardo Zimmer, Lisandro, Fredh e Gabriel por todas discussões técnicas, suporte e momentos de descontração. Um agradecimento especial ao Leonardo Donatti por toda ajuda na realização desse trabalho.

Agradeço ao Lucho, Isaias, Daniela e o Perin por todas conversas e discussões entre uma simulação e outra. Agradeço também a Larissa e a Aline pelas conversas agradáveis durante as idas e vindas ao RU. Aos demais colegas do Laboratório de Combustão e do GESTE, por todos os momentos compartilhados.

Para finalizar, agradeço a Universidade Federal do Rio Grande do Sul que me deu a oportunidade para que eu pudesse ter toda a minha formação acadêmica.

RESUMO

Atualmente, o processo de combustão é o principal responsável pelas emissões de gases do efeito estufa. Uma alternativa para uma matriz energética mais sustentável requer a utilização de combustíveis provenientes de fontes renováveis (biogás, gás de biomassa, etc.). No entanto, esses combustíveis muitas vezes são caracterizados por um baixo poder calorífico, o que torna difícil sua estabilização e controle em queimadores convencionais. Dessa forma, os queimadores porosos são uma opção viável para esse tipo de aplicação. Tal tecnologia permite a recirculação do calor das regiões próximas à frente de chama para regiões de pré-queima resultando no pré-aquecimento da mistura, trazendo como consequência: maior faixa de estabilidade, aumento da eficiência e baixa emissão de poluentes. Nesse contexto, o presente estudo avalia a estabilidade de queimadores porosos em regime estacionário e transiente para diferentes configurações usando uma abordagem numérica. Para contornar o elevado tempo computacional atualmente requerido em simulações de combustão com cinética química detalhada, a técnica *Flamelet Generated Manifold* (FGM) foi implementada e validada usando um mecanismo cinético de 22 espécies e 104 reações (DRM22) em uma chama pré-misturada estabilizada em um queimador tipo pórtico com perdas de calor. Os resultados demonstram uma boa concordância quantitativa tanto numa abordagem unidimensional quanto bidimensional nos perfis de temperatura e nas espécies avaliadas. Além disso, foi realizada uma detalhada comparação da velocidade de chama que mostraram os efeitos da perda de calor pelas bordas do queimador e os efeitos de curvatura na região da ponta da chama. Após, a técnica FGM foi implementada e validada em um queimador poroso em regime estacionário e transiente. Posteriormente, a configuração foi explorada em condições que precedem a condição de *blowoff* para diferentes propriedades da matriz porosa. Além disso, foi avaliado o comportamento do queimador quando imposto a diferentes condições de pulsos em regime transiente (período e magnitude) utilizando como condição inicial as condições que precedem o *blowoff*. Foi observado que o aumento da condutividade térmica do sólido reduz a faixa de estabilidade. Isso tem ocorrido devido a estabilização da chama no limite de *blowoff* ser mais a jusante e a diferença de temperatura entre as fases serem maior para diferentes condutividades. Na última parte, foram explorados numericamente

dois queimadores porosos axissimétricos com similar mecanismo de estabilização fluidodinâmica. No primeiro foi avaliado um queimador poroso divergente, enquanto na segunda abordagem foi mantida a mesma área de passagem transversal, alterando a porosidade e o diâmetro do poro na direção longitudinal. A segunda abordagem também recebe destaque (inclusive no âmbito industrial) devido ao desenvolvimento de tecnologias de manufatura aditiva ocorrido nos últimos anos. Dessa forma, uma comparação da faixa de estabilidade, eficiência da recirculação de calor, além de uma discussão detalhada do comportamento do escoamento na região da chama foram realizadas. Os resultados mostraram que um maior diâmetro de poro e porosidade aumenta condutividade térmica do sólido efetiva, favorecendo a recirculação do calor. Com isso, a configuração com uma variável matriz porosa apresentou uma faixa de estabilidade superior quando comparado com o queimador poroso divergente.

Palavras-chave: FGM; Perda de calor; Estabilização de chamas pré-misturadas; Combustão em meios porosos.

ABSTRACT

Currently, the combustion process is the main responsible for greenhouse gas emissions. An alternative for a more sustainable energy matrix requires the use of fuels from renewable sources (biogas, biomass, etc.). However, these renewable fuels are often characterized by a low calorific value, which makes it difficult to stabilize in traditional burners. Therefore, porous burners are a feasible alternative for this type of application. This technology allows the recirculation of heat from regions near the flame front to pre-flame regions, resulting in the pre-heating of the unburned gases. The consequences are increased stable range, increased efficiency, and low pollutant emissions. In this context, the present study evaluates the stability of porous burners in steady and transient conditions for different configurations using a numerical approach. Currently, a high computational time is necessary to solve combustion processes when detailed chemistry is required. Thus, the Flamelet Generated Manifold (FGM) technique was implemented and validated step-by-step using a mechanism with 22 species and 104 reactions (DRM22) in a slot burner with heat losses. The results demonstrate a good quantitative agreement for the temperature profile and species evaluated in one-dimensional and two-dimensional domains. In addition, a detailed evaluation of burning velocity was performed, which showed the influence of heat loss and curvature of the flame tip in the burning velocity. After, the FGM technique was also implemented and validated in a porous burner considering stationary and transient regimes. The model was explored in conditions that precede the blowoff for different porous matrix properties. These conditions were applied as initial conditions and pulses with different magnitudes and periods were evaluated. It was observed that the increase in the solid thermal conductivity reduces the stability range. This has occurred because the flame stabilization at the blowoff limit is located downstream, and the temperature difference between the phases is higher for different conductivities when compared with the porosity. In the last part, two axisymmetric porous burners with a similar fluid dynamic stabilization mechanism have been explored. One of them is a porous burner with a conical shape. The second is a porous burner with graded porosity and pore diameter that progressively maintain the same void area for the gas flow of the conical porous burner. The porous matrix with graded porosity is highlighted

(including in the industrial field) due to the recent development of additive manufacturing technologies. Thus, a comparison of stability range, convective heat exchange, and a detailed discussion of the flow behavior near the flame region has been performed.

Keywords: FGM; Heat loss; Premixed flame stabilization; Porous media combustion.

INDEX

1	INTRODUCTION	1
1.1	Objectives	6
1.2	Outline	6
1.3	Main contributions	7
2	NUMERICAL STUDY OF THE LAMINAR PREMIXED FLAME STABILIZATION ON A SLOT BURNER: COM- PARISON BETWEEN DETAILED AND FGM MODELS	10
2.1	Introduction	10
2.2	Method	12
2.2.1	Problem definition	12
2.2.2	The FGM technique with heat losses	13
2.2.3	Determination of laminar burning velocity from the two dimensional flames	17
2.3	Results	18
2.3.1	Manifold validation	18
2.3.2	Two-dimensional simulations	19
2.3.3	Evaluation of the laminar flame speed	26
2.4	Conclusions	28
3	NUMERICAL STUDY OF FLAME STABILITY WITHIN INERT POROUS MEDIA SUBJECTED TO FLOW OS- CILLATIONS	29
3.1	Introduction	29
3.2	Method	31
3.2.1	Model Description	31
3.2.2	Domain and Boundary Conditions	35
3.3	Results and Discussion	37
3.3.1	Comparison between direct integration and FGM technique	37
3.3.2	Steady State Stability	40
3.3.3	Transient response to flow perturbation	45
3.4	Conclusions	53

4	NUMERICAL STUDY OF FLAME STABILITY WITHIN INERT POROUS MEDIA WITH GRADED GEOMETRI- CAL PROPERTIES	55
4.1	Introduction	55
4.1.1	Problem Definition	58
4.1.2	Mathematical formulation	59
4.2	Results and Discussion	64
4.2.1	Flame front position and Stability range	66
4.2.2	Detailed analysis of the flame front	71
4.3	Conclusions	79
5	CONCLUSIONS AND FUTURE WORKS	80
5.1	Future work	82
	BIBLIOGRAPHY	83
	APPENDIX A Mathematical formulation of premixed laminar flames	92
	APPENDIX B Volume averaging method	98
	APPENDIX C Flamelet Generated Manifold Technique	102
	APPENDIX D Flowchart of FGM implementation in a porous burner	110
	APPENDIX E Mesh evaluation	111
	APPENDIX F Curriculum Vitae	112

LIST OF FIGURES

Figura 1.1	World’s total primary energy supply by fuel and scenario. (a) Stated Policies Scenario (STEPS) that means what measures governments have actually put in place. (b) Announced Pledges Scenario (APS) that means the commitments between more than 50 countries to meet net zero emission target. (c) IEA’s landmark Net Zero Emissions by 2050 Scenario (NZE). Adapted: [IEA, 2021].	1
Figura 1.2	SiC foam porous burner. Adapted: [Pereira et al., 2002]	2
Figura 1.3	(a) PMC and the profile of solid and gas temperature inside of porous media. (b) Representation of the total enthalpy inside of PMC (Adapted: [Hardesty and Weinberg, 1973]).	3
Figura 1.4	3D-printed porous burner. Adapted: [Ortona et al., 2017].	5
Figura 2.1	The 2D planar burner configuration.	12
Figura 2.2	Schematic representation of the 2D manifold with the different approaches for distinct regions. The range of the control variables is from -0.688 to 1.032 for the progress variable definition adopted and -1.56×10^{-5} to -3.00×10^{-6} for enthalpy. . .	16
Figura 2.3	Extraction of the burning velocity from the two-dimensional results (κ value is the ratio between $298K/315K$).	18
Figura 2.4	Manifold validation for one-dimensional adiabatic freely propagating flame of CH_4/Air at $\phi = 1.0$ and atmospheric conditions. Comparison of FGM and detailed model for (a) temperature and (b) CO mass fraction.	19
Figura 2.5	Mesh independence test for the two-dimensional simulations: (a) progress variable profile for different meshes at 3 mm from the burner nozzle exit; (b) temperature profile for different meshes at 3 mm from the burner nozzle exit.	20

Figura 2.6	Comparison between detailed chemistry and FGM results. Contours of: (a) progress variable \mathcal{Y} , (b) temperature, (c) OH, (d) CO, (e) HO ₂ , (f) HCO, (g) CH ₂ and (h) normalized heat release rate.	21
Figura 2.7	Comparison of the reaction progress variable \mathcal{Y} (a) and the temperature (b) profiles between detailed and FGM simulations at 7 mm (top), 3 mm (middle) and 1 mm (bottom) from the burner nozzle exit. Maximum reactants velocity of 1.1 m/s. . .	24
Figura 2.8	Comparison of (a) CO, OH, CO ₂ and (b) HCO, HO ₂ , CH ₂ mass fractions profiles between detailed and FGM simulations at 7 mm (top), 3 mm (middle) and 1 mm (bottom) from the burner nozzle exit. Maximum reactants velocity of 1.1 m/s.	25
Figura 2.9	Contours of temperature (a) and CO mass fraction for detailed and FGM simulations for the maximum reactants inlet velocity of 1.33 m/s.	26
Figura 2.10	Burning velocity (a;c) along the flame surface normalized by the 1D burning velocity ($S_l^o=29.72$ cm/s) and temperature (b;d) at the maximum heat release rate position normalized by the same temperature from a 1D adiabatic simulation ($T_h^o = 1721$ K). Reactants inlet velocity of 1.10 m/s (a;b) and of 1.33 m/s (c;d).	27
Figura 3.1	Representations of the two-dimensional manifold \mathcal{Y} versus h . Symbols represents points mapped on the database according to the method for controlling the enthalpy. Red circle represents case PMC used when the FGM simulation with $u_{in} = 0.41$ m/s was preformed ($\varepsilon = 0.8$, $k_s = 10$ W/m.K).	34
Figura 3.2	Three-dimensional manifold (a) gas temperature (b) CO mass fraction.	34
Figura 3.3	Schematic transient boundary inlet condition imposed in the present study.	35

Figura 3.4	(Left column) Comparison of FGM technique and DI method for the T_g (top panel), T_s (middle panel) and Y_{CO} (bottom panel) ($v_{in} = 0.28$ m/s and $v_{in} = 0.41$ m/s). (Right column) Comparison of FGM technique and DI method for the gas temperature for time = 0 s, 0.02 s and 0.1 s. The initial condition with 0.41 m/s. The porosity considered is equals to 0.7, solid thermal conductivity equals to 1 W/m.K and F^* equals to 0.2.	39
Figura 3.5	Heat release rate position normalized and convective heat exchange between gas and solid phase ($k_s = 5$ W/m.K, $\varepsilon = 0.8$, $v_{in}/s_F^0 = 1.41$). Burning velocity (s_F^0) is assumed equals to 29.72 cm/s ($Le = 1$) when the temperature is equals to 300 K (DRM22).	41
Figura 3.6	(a) Effects of porosity ($k_s = 1$ W/m.K) and (b) solid thermal conductivity ($\varepsilon = 0.8$) on the T_g and T_s and their respective values (c and d) of η_{rec} and η_{rad} . The mass flux rate is maintained equals to 0.28 $kg/m^2.s$	42
Figura 3.7	Effects of ε on the εHRR , gas temperature, velocity, and $\varepsilon \dot{\omega}_{CH_4}$ with mass flux rate = 0.28 $kg/m^2.s$ and $k_s = 1$ W/m.K.	43
Figura 3.8	Effects of porosity ($k_s = 1$ W/m.K) and (b) solid thermal conductivity ($\varepsilon = 0.8$) on the T_g and T_s	44
Figura 3.9	Evaluation of (a) the blowoff limit (voided symbols correspond to v_{in}/s_F^0 and filled symbols correspond to x_f^*) and (b) η_{rec} (filled symbols) and η_{rad} (voided symbols) for ε equals to 0.8, 0.7 and 0.6.	45
Figura 3.10	Transient behavior of gas temperature (a and b) solid temperature (c and d) and CO mass fraction (d and e), respectively. The case presented is $\varepsilon = 0.8$, $k_s = 1$ W/m.K, $F^* = 0.925$ and $T = 0.5$ s. On the left, perspective view of variable as function of position and time. On the right, the projection of the time sequential on the variable position plane.	47

Figura 3.11	Evaluation of (a) s_c and u_{in} . (b) x_f and maximum solid temperature position ($x_{T_s,max}$), displacement velocity (s_d), $x_{T_s,max}$ and ($\dot{x}_{T_s,max}$) for $\varepsilon = 0.8$, $k_s = 1$ W/m.K, $F^* = 0.925$ and $T = 0.5$ s.	49
Figura 3.12	(a) Convective heat exchange between gas and solid phase and, (b) gas-to-solid convection efficiency and radiation efficiency ($\varepsilon = 0.8$, $k_s = 1$ W/m.K, $F^* = 0.925$ and $T = 0.5$ s).	51
Figura 3.13	(a) Displacement velocity (s_d) evaluation along the time for different multiplicative factor (F^*) for the $\varepsilon = 0.8$ and $k_s = 1$ W/m.K.	52
Figura 3.14	Comparison of s_d during on the time equals 0.25 s (R2) and 0.75 s (R4) for different (a) k_s ($\varepsilon = 0.8$) and (b) for different ε ($k_s = 1$ W/m.K).	52
Figura 3.15	Evaluation of the blowoff limit for different (a) k_s ($\varepsilon = 0.8$) and (b) for different ε ($k_s = 1$ W/m.K).	53
Figura 4.1	Scheme of the numerical domains.	58
Figura 4.2	Pore diameter, porosity and void area.	59
Figura 4.3	C and m of correlation $Nu = CRe^m$ [Younis and Viskanta, 1993].	61
Figura 4.4	Comparisons of gas temperature and solid temperature between the present study and previous studies (Barra et al. [2003]; Liu et al. [2010]).	64
Figura 4.5	Comparison between VPB, VAB and UGB for $v_{in}/S_L = 2.91$ and $\phi = 1$. (a) Normalized temperature contours for the gas and solid phase. (b) Normalized gas and solid temperature and heat release rate (HRR), and (c) normalized gas velocity on the centerline.	65
Figura 4.6	Evaluation of (a) flame front position (x_f) for different inlet velocity, (b) turn down ratio and power range for VPB, VAB and FPV for $\phi = 0.65$ and 1.0.	67
Figura 4.7	(a) Contour of two dimensional convective heat exchange (q_v). VPB imposing $\phi = 0.65$, and velocity equals to $v_{in}/S_l = 1.20$ (c) q_v , θ_g and θ_s evaluated on the wall and axis.	68

Figura 4.8	Heat recirculation efficiency as a function of inlet velocity for equivalence ratio equals to 0.65 and 1.0.	69
Figura 4.9	Evaluation on the centerline of gas temperature (θ_g), solid temperature (θ_s), convective heat exchange (q_v), and effective solid thermal conductivity normalized (k_{eff}/k_s) for the (a) VPB considering $v_{in}/S_l = 3.35$ (- solid line) and $v_{in}/S_l = 5.33$ (- - dashed line) and (b) VAB considering $v_{in}/S_l = 3.35$ (- solid line) and $v_{in}/S_l = 3.70$ (- - dashed line). The equivalence ratio evaluated is 0.65.	70
Figura 4.10	Contour of two dimensional convective heat exchange (q_v), streamlines (black dashed line - -), level curve of solid temperature (black solid lines -), solid-phase heat flux lines (red solid lines -). The bold streamlines (S1, S2 and S3) correspond to conditions for which temperature (θ_g and θ_s) and heat release rate (HRR) profiles are presented in Figure 4.12. VPB (a) $\phi = 0.65$ and $v_{in}/S_l = 3.7$ m/s. (b) $\phi = 1$ and $v_{in}/S_l = 3.41$ m/s. VAB (c) $\phi = 0.65$ and $v_{in}/S_l = 3.7$ m/s. (d) $\phi = 1$ and $v_{in}/S_l = 3.41$ m/s ($q_{v,max} = 1.1261 \times 10^8$ W/m ³ K).	73
Figura 4.11	Flame arc length (L_f) as a function of inlet velocity for ϕ equals 0.65 and 1.0.	74
Figura 4.12	Temperature (θ_g and θ_s) and heat release rate (HRR) from the streamlines S1, S2 and S3 highlighted in Figure 4.10. (a) VPB and (b) VAB with $\phi = 0.65$ and $v_{in}/S_l = 3.7$ m/s. (c) VPB and (d) VAB with $\phi = 1$ and $v_{in}/S_l = 3.41$ m/s.	76
Figura 4.13	Evaluation of contour normalized mass flow rate in axial (m_x) and radial direction (m_r). Streamlines (black dashed line - -), level curve of gas temperature normalized (black solid lines -), flow line of solid heat transfer (red solid lines -). The bold streamlines (S1, S2 and S3) correspond to conditions for which m_x and m_r profiles are presented in Figure 4.14. The present case is VPB considering $\phi = 1$ and $v_{in}/S_L = 3.41$	77

Figura 4.14	Mass flow rate on the S1, S2 and S3 along the VPB and VAB for (a) $\phi = 0.65$ and $v_{in}/S_l = 3.41$. (b) $\phi = 1$ and $v_{in}/S_l = 3.7$. . .	78
Figura C.1	Flowchart of the implemented methodology.	104
Figura C.2	Schematic representation of space of generic thermochemical variable ξ as a function of progress variable (\mathcal{Y}) and enthalpy (h).	106
Figura C.3	Schematic representation of 2D manifold with the different approaches for distinct regions.	108
Figura C.4	Illustration of bi-dimensional interpolation.	108
Figura D.1	Flowchart of FGM implementation.	110
Figura E.1	Mesh evaluation, (a) generated mesh with 35000 volumes, (b) gas temperature results imposing different mesh refinement. Simulation test with VPB imposing $v_{in}/S_l = 4.30$ and $\phi = 0.65$. . .	111

LIST OF TABLES

Tabela 2.1	Boundaries condition of laminar premixed flame.	13
Tabela 2.2	Boundary conditions imposed for \mathcal{Y} and h transport equations. . .	16
Tabela 3.1	Boundary conditions imposed for T_s , \mathcal{Y} and h transport equations.	36
Tabela 3.2	Computational time evaluated for each method in steady state regime. Each unity correponds to 1270 seconds [†]	38
Tabela 4.1	Boundary conditions imposed for momentum, T_s , \mathcal{Y} and h transport equations.	62
Tabela C.1	Boundaries condition imposed to solve a free flame.	105
Tabela C.2	FGM database structure.	107

LIST OF ABBREVIATIONS

3D DPLS	3D Direct Pore Level Simulation
CFD	Computational Fluid Dynamics
CHEM1D	One-dimensional laminar flame code
CV	Control Variable
EPE	Empresa de Pesquisa Energética
FGM	Flamelet Generated Manifold
FLUENT	CFD software
FPI	Flame Propagation of the ILDM
FPV	Flamelet/Progress Variable Model
HRR	Heat release rate
IEA	International Energy Agency
ILDM	Intrinsic-Low Dimensional Manifold
LHV	Lower Heating value
MEF	Método dos Elementos Finitos
PIM	Porous Inert Media
PM	Porous Media
PMC	Porous Media Combustor
PPC	Pores Per Centimeter
PROMEC	Programa de Pós-Graduação em Engenharia Mecânica
SI	Sistema Internacional
SIMPLE	Semi-Implicit Method for Pressure Linked Equations
UDF	User Defined Function
UDS	User Defined Scalar
UFRGS	Universidade Federal do Rio Grande do Sul

LIST OF SYMBOLS

A	Pre-exponential factor
C_2	Inertial resistance factor, $[1/m^2]$
c_p, C	Specific heat, $[J/kgK]$
d_{eff}	Equivalent porous cavity diameter, $[m]$
$D_{i,M}$	Mixture averaged diffusion coefficient, $[m^2/s]$
E_a	Activation energy, $[J]$
h	Specific enthalpy, $[J/kg]$
h_i	Partial specific enthalpy, $[J/kg]$
h_v	Volumetric heat transfer coefficient, $[W/m^3K]$
$\Delta h_i(T)$	Sensible enthalpy, $[J/kg]$
$\dot{j}_{k,i}$	Mass diffusion flux, $[mol/m^2s]$
k	Thermal conductivity, $[W/mK]$
k_r	Radiative conductivity of solid, $[W/mK]$
κ	Effective radiative extinction coefficient, $[1/m]$
L	Length $[m]$
Le	Lewis number, -
\mathcal{M}_i	Species symbol, -
M	Average molar mass, $[kg/mol]$
M_i	Molar mass, $[kg/mol]$
m	Mass burning rate, $[kg/m^2s]$
\dot{m}''	Mass flux rate, $[kg/m^2s]$
N_s	Number of species, -
N_r	Number of reactions, -
n_i	Number of the mols of the species i , -
n_t	Total number of mols of the system, -
p	Pressure, $[Pa]$
Pe	Peclet number, -
\dot{Q}	Total heat recirculation

q_k	Heat flux, $[W/m^2]$
\dot{q}_v	Heat source term between the gas and the solid, $[W/m^3]$
R_o	Ideal gas constant, $[J/molK]$
r_j	Reaction rate for reaction j , $[mol/m^3s]$
S_L	Laminar flame speed, $[m/s]$
s_F^0	Burning velocity, $[m/s]$
S_u	External forces, $[N/m^3]$
S_h	Heat source term, $[W/m^3]$
S	Pressure loss term, $[N/m^3]$
s	arc lengt, $[m]$
T	Temperature, $[K]$
t	Time, $[s]$
u	Velocity, $[m/s]$
V	Volume, $[m^3]$
X_i	Species mole fraction, -
x_f	Flame front position, $[m]$
x	Space coordinate, $[m]$
\mathcal{Y}	Reaction progress variable, $[mol/kg]$
Y_i	Species mass fraction, -

Greek

α	Thermal diffusivity of the gas, $[m^2/s]$
α	Permeability, $[m^2]$
α_i	Species weight factor, $[mol/kg]$
β	Temperature exponent, -
δ	Kronecker delta, -
ϵ	Emissivity, -
λ	Thermal conductivity, $[W/mK]$
μ	Dynamic viscosity, $[Pa.s]$
ν	Stoichiometry coefficients, -
ρ	Density, $[kg/m^3]$
σ	Stefan–Boltzmann constant, $[W/m^2K^4]$

τ	Tensor stress, [N/m^3]
θ	Normalized temperature
ε	Porosity, -
η	efficiency, -
ϕ	Equivalence ratio, -
$\dot{\omega}_i$	Species source term, [kg/m^3s]

Subscripts

<i>ad</i>	adiabatic
<i>bl</i>	blowoff
<i>c</i>	combustion reaction
<i>d</i>	displacement
<i>est</i>	stoichmetric
<i>f</i>	fuel
<i>g</i>	gas
<i>i</i>	initial
<i>in</i>	inlet
<i>hr</i>	heat recirculation
<i>o</i>	oxidant
<i>out</i>	outlet
<i>ph</i>	preheating
<i>rad, r</i>	radiation
<i>rec</i>	heat recirculation
<i>ref</i>	reference
<i>res</i>	resident time
<i>s</i>	solid
<i>sur</i>	surrounding
<i>u</i>	unburnt
<i>i, k, j</i>	index
∞	environment

Superscripts

<i>f</i>	foward
<i>b</i>	backward
o	formation
'	products
"	reactants
<i>c</i>	heat diffusion
<i>d</i>	mass diffusion
<i>D</i>	dufour effect

1 INTRODUCTION

The combustion processes play a central role in today's energy-intensive society especially in household heating, transport, power generation, industrial processes and many others. Although the available renewable energy source (hydroelectric dam, solar and wind parks, geothermal energy and renewable fuels) has increased during the last decades, the combustion of oil, coal and natural gas will represent an important portion according to the three projected scenarios presented in the last report of International Energy Agency (IEA) (Figure 1.1). Currently, there is full agreement that the use of fossil fuels affects the Earth's climate due to the products of combustion such as CO_2 , CO , SO_x , NO_x and other greenhouse gases released in the atmosphere. This is considered the main source of the global warming process. To restrain its advance, government regulatory agencies impose limits on pollutants emissions. They have suggested initiatives such as the carbon capture and sequestration, renewable fuels and increase the efficiency in energy use.

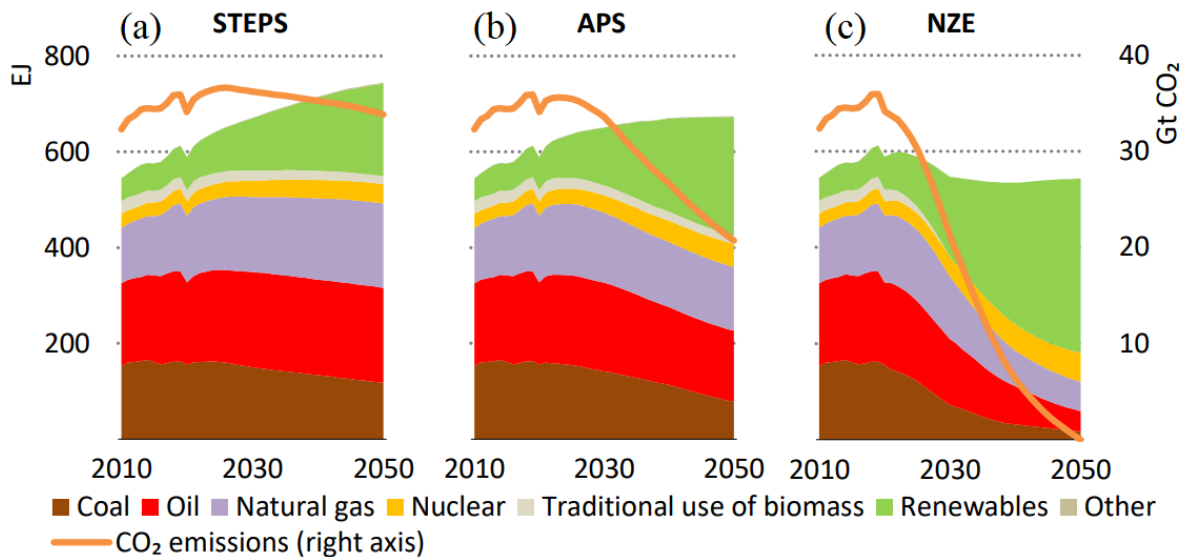


Figure 1.1 – World's total primary energy supply by fuel and scenario. (a) Stated Policies Scenario (STEPS) that means what measures governments have actually put in place. (b) Announced Pledges Scenario (APS) that means the commitments between more than 50 countries to meet net zero emission target. (c) IEA's landmark Net Zero Emissions by 2050 Scenario (NZE). Adapted: [IEA, 2021].

One of the possibilities to increase the combustion efficiency of gaseous fuels and

produce low NO_x and CO emissions is to use the porous media combustion (PMC) technology (Figure 1.2). PMC also contributes to the reduction of greenhouse gases due to its enhanced range of flammability, which allows for the burning of very lean mixtures. This feature of porous burners is also important for some renewable fuels like biogas and syngas, since they are characterized by a low caloric value and, depending on the composition, their stable application may be unfeasible without a technology such as PMC. In PMC, the reactant mixture is injected into a three-dimensional porous structure made of ceramic or metallic materials. The flame is stabilized inside the cavities inside the porous medium and interacts with the solid phase. An unidimensional steady-state configuration is presented in Figure 1.3a. The premixed gas (fuel/air) is imposed at the left side of the porous domain. Inside of PM, the gas reaches the flame front (x_f) and it is burned. Downstream from x_f , the gas temperature decreases due to heat exchange by convection with the solid. Part of heat there turns to the upstream region of the domain through the porous matrix by conduction and radiation. The consequence is a region with $T_s > T_g$ before the flame, which allows the reactants to be preheated and flame the temperature higher than the adiabatic flame temperature (T_{ad}).



Figure 1.2 – SiC foam porous burner. Adapted: [Pereira et al., 2002]

Another form to evaluate the heat recirculation of the porous media is by looking at the local enthalpy level (Figure 1.3b). When the premixed gas enters in the porous media the initial sensible enthalpy (H_i) is at its lower value. However, as a result of the heat recirculation (Q_{hr}), the enthalpy increases to $H_i + Q_{hr}$ before the flame. When the gas enters in the flame region, the enthalpy increases again due to the addition of the heat

released by the combustion reaction (H_c), achieving its maximum value ($H_i + Q_{hr} + H_c$). Downstream from the flame, the gas-phase loses heat (Q_{hr}) to the solid-phase and the sensible enthalpy decreases to its thermodynamic limit ($H_i + H_c$). Thus, it is possible to see that the gas experiences an intermediary state of excess enthalpy ($H_i + Q_{hr} + H_c$) which can lead to temperatures higher than the adiabatic flame temperature. At the outlet condition, the gas cannot leave the porous medium above the thermodynamic limit ($H_i + H_c$), but it can leave below this limit due to radiative heat losses.

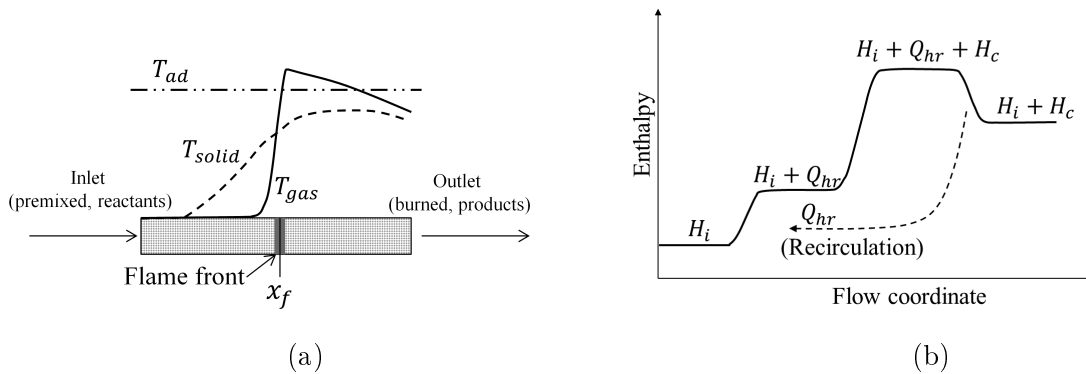


Figure 1.3 – (a) PMC and the profile of solid and gas temperature inside of porous media. (b) Representation of the total enthalpy inside of PMC (Adapted: [Hardesty and Weinberg, 1973]).

The excess enthalpy provides some benefits. The first is the reduction of emissions of gases from incomplete combustion, for example, CO. The higher temperature in the combustion region enables higher reaction rates increasing the conversion of hydrocarbons to CO_2 . The second is that with higher reaction rates the burning velocity is increased, which enhances the power density of the device compared to other laminar burners. In contrast, the higher temperature can increase the pollutants as NO_x , a problem that can be reduced by using lean mixtures. An advantage is that porous burners can be designed to sustain very poor mixtures or burn fuels of very low heat content that would not be flammable in other devices. With PMC, efficient radiant burners can also be designed taking advantage from the high temperatures of the solid phase at the outlet surface.

PMC have applications in different fields as curing and drying processes at many materials (paint, paper, ceramic, grains, metals, resins) and still are subject of study in areas as lighting [Qiu and Hayden, 2006], domestic cooking stoves [Pantangi et al.,

2011; Kaushik et al., 2020], boilers [Yu et al., 2013], heat exchangers [Amatachaya and Krittacom, 2017], turbines [Djordjevic et al., 2012] and microcombustors [Wang et al., 2019b]. Recently, Banerjee and Paul [2021] presents a review with developments and more applications involving of porous medium combustion. The vast range of possible configurations allowed by PMC (burner geometry, material, porosity, etc) opens up the opportunity of designing specific burners tailored to meet high performance in terms of flame stability and heat transfer characteristics. Because of the wide range of applicability of this technology and the possibility of building burners with very different configurations, it is essential to have a detailed knowledge of the phenomena involved in the stabilization of flames within porous burners. Blow-off and flashback are now dependent on the global geometry of the porous medium, geometrical details of the porous structure, and on thermal properties of the solid matrix like heat capacity, thermal conductivity, and surface emissivity. Since it is not possible to cover all important variables for flame stabilization within porous burner, this work will concentrate on some key aspects, namely the flame stability near blow-off conditions and how the stability range for burner with graded geometrical properties.

The present work explores a porous burner in the condition that precedes the blowoff for a range of porosity and solid thermal conductivity. Thereafter, the results are used as initial conditions to evaluate the behavior in transient regime of solid and gas phases when imposed to pulses in the inlet mass flux rate. These conditions could happen in a non-desired oscillation on the gas supply line due to some control failure, for example. Although, there are many studies involving porous burner evaluating transient regime [Lammers and De Goey, 2003; Zheng et al., 2011; Chen et al., 2018; Yakovlev and Zambalov, 2019] and some recent studies evaluating the fluctuation of gas supply [Habib et al., 2021a,b]. It has not been found any detailed numerical evaluation exploring a mass flow oscillation with the flame stabilized inside the porous matrix.

In addition, a porous burners evaluation with variable porosity and pore diameter is carried out given the advance of additive manufacturing technologies (Figure 1.4). This approach replaces porous media that are commonly designed using stochastic foams. [Sobhani et al., 2018] evaluated experimentally and numerically a porous burner, having a spatially graded using a combination of traditional porous matrix with different porous diameter and porosity. Results from the 1D volume averaged simulations model presented

an important improvement in flame stability between step and graded topology matrix. The graded matrix was tested experimentally, and the results qualitatively confirmed an enhancement of the flame stability compared to the traditional design. Recently, the same group explored the feasibility of three tailored PMBs experimentally [Sobhani et al., 2021]. The porous matrix were developed using additive manufacturing technologies. The results has shown that the model with graded pore diameter and fixed porosity presents wide stable range when compared with a traditional design.

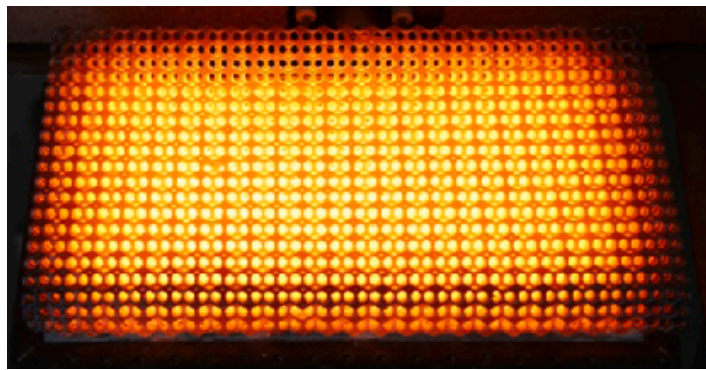


Figure 1.4 – 3D-printed porous burner. Adapted: [Ortona et al., 2017].

Despite of the extensive research on porous burner, there is a lack of studies presenting an evaluation of porous burner with graded porosity and pore diameter in a multidimensional configuration. This way, to expand the discussion of this subject, this study evaluates the differences between two forms of creating a similar hydrodynamic stabilization mechanism. One of them is by using a porous burner with graded porosity that progressively increases the void area for the gas flow. The other is a porous burner of constant porosity, but with a conical shape with the same increasing void area for the gas flow. Besides, a detailed discussion about the flame region is explored in details in an attempt to explain the flame profile. In the literature, the approach applied has not been used to evaluate flame behavior in porous burners. It was observed that it could bring relevant informations in the knowledge of physics involving porous burners.

As the numerical modeling of combustion systems still represents a great challenge in multidimensional configurations with detailed kinetics. Thus, the present study carried out the implementation of a reduced kinetic technique called Flamelet-Generated Manifold (FGM) method. Although, the FGM method presents a satisfactory agreement to capture heat loss effects, few studies has been found exploring porous burner [Van Oijen

et al., 2001; Lammers and De Goey, 2004]. Such method is not immediate to implement, it has been gradually performed and carefully validated. As first, the one-dimensional free-flame imposing FGM technique is evaluated and compared with detailed chemistry. Subsequently, the heat loss effects are included and validated in a two-dimensional slot burner. Thereafter, the porous burner formulation is implemented and validated in a steady and transient regime considering a one-dimensional domain.

1.1 Objectives

The objective of the present thesis is to explore two aspects of flame stability within inert porous media: the effect of flow oscillations for near blow-off conditions and the stability range for burners with graded geometrical properties. A secondary objective is to model the combustion in porous media with the FGM reduction technique, to reduce the cost of transient and two-dimensional simulations.

To achieve the main objective the following goals are defined:

1. To implement and validate the FGM technique with heat loss.
2. To adapt and validate the FGM technique for application in porous burners.
3. To evaluate the flame stability within inert porous media subjected to flow oscillations.
4. To evaluate the flame stability within porous media with graded geometrical properties.

1.2 Outline

After the introduction chapter, the present thesis is organized in more three chapters written in the form of articles. They are presented in their final form as follows:

1. **Chapter 2 (article 1):** Numerical study of the laminar premixed flame stabilization on a slot burner: comparison between detailed and FGM models (published in 2020. *J Braz. Soc. Mech. Sci. Eng.* 42, 189. doi: <https://doi.org/10.1007/s40430-020-2267-9>).

2. **Chapter 3 (article 2):** Numerical study of flame stability within inert porous media subjected to flow oscillations (*to be submitted*).
3. **Chapter 4 (article 3):** Numerical study of flame stability within porous media with graded geometrical properties (*to be submitted*).

Throughout these three chapters, a framework for the simulation of the combustion process in a porous burner with graded geometrical properties is created step-by-step. The development of such methodology needs to be achieved through many careful implementations. Thereby, Chapter 2 presents an implementation and validation of the FGM technique for premixed laminar flames with heat loss. This flamelet technique is implemented to include a detailed chemistry and to avoid a high computational time. Chapter 3 performs the implementation and validation of the FGM technique in a one-dimensional porous domain where the porous matrix parameters (porosity and pore diameter) is maintained constant and solved in steady-state and transient regime. Here, it is necessary to increase the maximum enthalpy level in order to capture the effects of gas preheating that occurs in the porous burner. In the same chapter, it is included heat exchange between the gas and solid phase. In the chapter 4, the development of the model is extended to an axisymmetric domain. Furthermore, the porous matrix parameters are no longer kept constant as well as a model to represent the radiation is implemented. The final implementation incorporates most of the complexities of physics involved in a porous burner, ready to be employed in many others configurations, including industrial scenarios.

Because of the mathematical formulation of premixed laminar flames has already been widely discussed in other studies, its presentation is only made in their final form in appendix A of the present work.

1.3 Main contributions

The three articles highlighted in the previous sections of this work intend to bring the following contributions to the literature: Firstly, an implementation of the FGM technique for premixed laminar flames using detailed chemistry in a slot burner. Although, the case of study is a flame in a box similar to those studied by van Oijen et al. [2001]. Two stoichiometric flames are investigated, one of them close to the blow-off limit. The results of temperature, progress variable, and mass fraction of selected species, and the

prediction of the burning velocity distribution along the flame surface are presented and discussed in detail. To further verify the agreement between the FGM and the detailed model, the flame temperature along the surface of maximum heat release rate are also compared. This type of detailed comparison is not found in previous studies de Goey and ten Thijs Boonkamp [1999]; van Oijen et al. [2001]; van Oijen and de Goey [2002]; Fiorina et al. [2003]; Donini et al. [2015a].

Secondly, an implementation of the FGM technique within the porous matrix is developed and validated. Similar approach using the FGM technique has been found in the literature [Van Oijen et al., 2001; Lammers and De Goey, 2004], but the flame is stabilized at the porous burner outlet while in the present study the flame is stabilized completely inside of the porous matrix. It brings a necessity of increasing the enthalpy levels to reach higher values. Such demand has not been reported in previous studies. Completed the implementation and validation, the model is assessed in the condition that precedes the blowoff. After, a detailed numerical evaluation is presented to assess the behavior of gas and solid phase when imposed to flow oscillations. The study was performed for a range of porosity and solid thermal conductivity. Results of flame position, heat recirculation, and radiation emission was also presented in the transient regime. Evaluating relevant reviews [Mujeebu et al., 2009; Ellzey et al., 2019; Banerjee and Paul, 2021], it was observed that the majority of studies on combustion in porous media are concentrated on steady-state conditions. Narrowing to studies with oscillations on the gas supply line, only two recent experimental studies have been found [Habib et al., 2021a,b]. Thereby, the present chapter brings a unique discussion about the behavior of the flame when subjected to flow oscillations.

In the last article, after the methodology for porous burners has been tested and validated, it was performed a numerical evaluation of a porous burner with graded porosity. The comparison has been motivated by the recent advance of additive manufacturing (AM) technologies. Although a recent review has suggested that AM would create possibilities of research and manufacture of new reactors [Ellzey et al., 2019], only two studies have been found exploring this configuration in the porous burner at current time [Sobhani et al., 2018, 2021]. However, both approaches tested numerically are one-dimensional. Thereby, one of the contributions of the present study is to evaluate a porous burner with graded porosity in an axisymmetric domain with a new distribution of porosity and pore

diameter. In order to compare the stable range with a traditional porous matrix, it has been proposed a divergent domain. This configuration has been chosen to maintain the same void area, and consequently, to obtain a similar hydrodynamic stabilization mechanism. Moreover, divergent domain is a known geometry that have been explored in some studies [Hashemi and Hashemi, 2017; Bedoya et al., 2015; Bakry et al., 2011]. To finalize, the present study evaluated in detail the flow and heat exchange near flame. Even though this approach has been performed in propagation of premixed flames [Kim and Maruta, 2006], it was not found studies that applied this evaluation in a porous burner.

2 NUMERICAL STUDY OF THE LAMINAR PREMIXED FLAME STABILIZATION ON A SLOT BURNER: COMPARISON BETWEEN DETAILED AND FGM MODELS

2.1 Introduction

Many efforts have been made worldwide to reduce the fossil fuels consumption, even so, they will remain as the main energy source for the next decades IEA [2017]. In Brazil, where the production of renewable energy is significantly higher compared with other countries, the energy from fossil fuel represented 52.5% of the energy matrix in 2016 EPE [2017]. These numbers lead to the development of new technologies and studies to enhance the combustion process efficiency.

Combustion presents a strong coupling with high non-linear dependence among chemical, fluid dynamic, thermodynamics and heat transfer processes. Thus, modeling flames in practical industrial applications using detailed reaction mechanisms are still prohibitive due to the high CPU-time required to solve a large number of species and reactions. For this reason there is a long-standing interest to develop reliable combustion models with high accuracy at low computation time. Chemical reduction techniques intend to meet these requirements for numerical simulations of flames. One alternative is to conduct a reduction of chemical mechanisms assuming quasi steady state assumption (QSSA) and partial equilibrium assumption (PEQ) Peters [1985]; Peters and Rogg [1993]. Another approach are tabulation techniques, e.g. Piecewise Reusable Implementation of Solution Mapping (PRISM) Tonse et al. [1999] and In Situ Adaptive Tabulation (ISAT) Pope [1997]. These techniques store simulation results for *a posteriori* use. Recently, Cailler et al. [2017] has proposed building a chemical mechanism from scratch instead of reducing a detailed scheme. Using a novel idea, the authors rely on the use of virtual species and optimization procedure to capture the coupling between combustion and the flow field.

Other reduction methods assume that the flow time scale is much higher than the chemical time scales, hence flow and chemistry can be decoupled. Two of the most popular applications of this assumption is the Intrinsic Low-Dimensional Manifold (ILDM) developed by Maas and Pope [1992] and the steady laminar flamelet model developed by Peters [1984]. However, the former is pointed out to lose accuracy in colder regions of

the flame Oijen and Goey [2000] whereas the later does not have the ability to describe ignition or extinction processes.

Thereby, Oijen and Goey [2000] proposed the Flamelet-Generated Model (FGM) technique to overcome these problems. In the FGM framework, a database representing the combustion process is built from storing a set of laminar one-dimensional flames solved with detailed chemical kinetic (*flamelets*) as function of some control variables. In some cases, this methodology can be a hundred times faster than the direct integration of the conservation equation van Oijen [2002] without losing much accuracy. Similar approaches as the FGM are Flamelet/Progress Variable Model (FPV) proposed by Pierce and Moin [2004] and the Flame Prolongation ILDM (FPI) proposed by Fiorina et al. [2003].

The solution of premixed flame with heat loss using the FGM technique has been initially studied by van Oijen et al. [2001]. The authors have explored a 2D laminar premixed flame and validated their results with a detailed model. Then, the authors explored their model in a radiating furnace with a ceramic-foam surface burner on the upper wall. The numerical simulation using FGM agreed well with experimental measurements. Donini et al. [2015b] has presented numerical results for the DLR burner with heat loss at the walls using the FGM technique.

In the present work, the heat loss model is implemented in the FGM technique and validated by comparison with the direct integration of the full set of conservation equations. The case of study is a flame in a box similar to those studied by van Oijen et al. [2001]. Two stoichiometric flames are investigated, one of them close to the blow-off limit. The results of temperature, progress variable and mass fraction of selected species, and the prediction of the burning velocity distribution along the flame surface are presented and discussed in detail. A comparison of the predicted burning velocity along the flame surface. To further verify the agreement between the FGM and the detailed model, and compared the flame temperature along the surface of maximum heat release rate. This type of detailed comparison is not found in previous studies de Goey and ten Thijs Boonkamp [1999]; van Oijen et al. [2001]; van Oijen and de Goey [2002]; Fiorina et al. [2003]; Donini et al. [2015a].

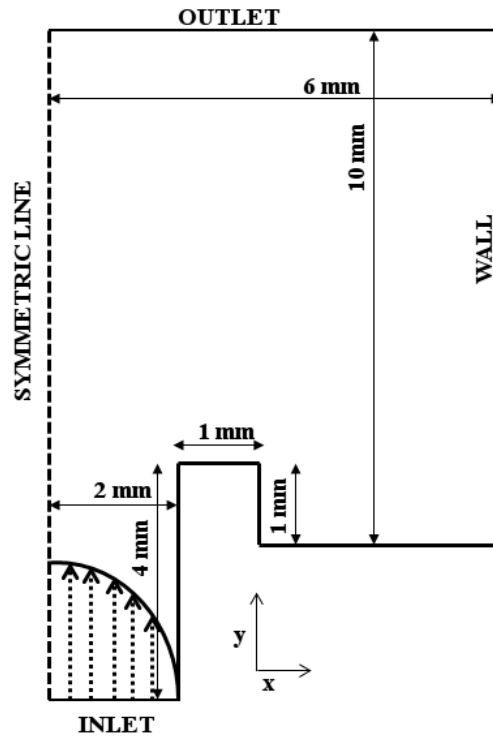


Figure 2.1 – The 2D planar burner configuration.

2.2 Method

2.2.1 Problem definition

In this work, premixed laminar flames of CH_4/Air are modeled with the FGM technique considering heat losses. Two-dimensional planar simulations are performed. The computational domain is shown in Figure 2.1 and represents a slot burner in an enclosure with an outlet at the top. The inlet is 4 mm wide channel and the outlet 12 mm wide. The walls and the gas inlet are at a constant temperature (T) of 298 K. The fresh gas velocity has a parabolic profile with a maximum value of 1.1 m/s and 1.33 m/s (the velocity that precedes the blow off), equivalent to a velocity gradient at the equal to 1100 s^{-1} and 1330 s^{-1} , respectively. The outlet surface is assumed to be at 1 atm. The problem is the same test case already described by Somers and De Goey [1995] and Fiorina et al. [2003].

Table 2.1 – Boundaries condition of laminar premixed flame.

Unburnt Side	Burnt Side
$Y_i(-\infty) = Y_i$	$\partial Y_i / \partial s(+\infty) = 0$
$h(-\infty) = h$	$\partial h / \partial s(+\infty) = 0$

2.2.2 The FGM technique with heat losses

The general methodology of the FGM technique is described as follows. Flamelet solutions, for a specific equivalence ratio, are obtained for different levels of enthalpy and, then, stored in a database (a manifold) as a function of some control variables. After the manifold construction is finished, multidimensional simulations are conducted solving only the conservation of total mass, momentum and the transport equations for the control variables. Therefore, the solution of the conservation equations of each chemical species is not required as in detailed simulations. Once the convergence is achieved, the multidimensional structure of the flame is reconstructed from the manifold with the control variables solution. The flamelet equations, the appropriate definition of control variables, and the manifold generation are described in the next sections.

2.2.2.1 Manifold construction

The initial step of the FGM methodology is to solve a set of one-dimensional flames to map the thermo-chemical space. The method to account for the enthalpy changes on the flames will be clearly described in Sec. 2.2.2.1.1. First, the system of conservation equations describing detailed one-dimensional laminar freely propagating premixed flames is solved through laminar flame code Chem1D. The equation system accounts for conservation of total mass, chemical species mass fraction and mixture specific enthalpy. The conservation equations - neglecting curvature, stretch, and tangential diffusion - are solved for the steady-state regime. The boundary conditions are presented in the Table 2.1.

Flames are computed with the DRM22 kinetic mechanism (formed by 22 species and 104 reactions) Kazakov and Frenklach [1995]. Transport properties are simplified by the unity Lewis number assumption. A diffusion velocity correction is considered for N_2 to ensure the total mass conservation. Mixture thermal conductivity and dynamic viscosity are obtained from simplified polynomial expressions as function of mixture specific heat

and temperature following Smooke and Giovangigli [1991b]. Species specific heat is obtained according to McBride et al. [1993]; Burcat and C. Gardiner Jr [2000]. It was found that a computational domain of 2.5 cm discretized in 100 volumes with an adaptative mesh routine was sufficient to achieve mesh independent solutions.

Then, any scalar ψ from the flamelet solutions can be tabulated as function of the control variables. The control variables, in the present case, are the progress variable (\mathcal{Y}) and enthalpy (h); forming a 2D manifold where $\psi = \psi(\mathcal{Y}, h)$. The progress variable describes the chemistry evolution from unburnt reactants to combustion products. According to Oijen and Goey [2000], a progress variable can be represented by a linear combination of species mass fraction, Y_i .

In this work it was sought from literature the \mathcal{Y} definition used by Donini et al. [2015a]:

$$\mathcal{Y} = -\alpha_{O_2}Y_{O_2} + \alpha_{CO_2}Y_{CO_2} + \alpha_{H_2O}Y_{H_2O} + \alpha_{H_2}Y_{H_2} \quad (2.1)$$

where the weighting factor (α_i) is given by the inverse of the species i molar mass ($\alpha_i = 1/MW_i$). The mixture enthalpy, on its turn, maps different thermodynamic states due to heat losses to the burner walls and to the environment when radiative heat losses are taken into account. Finally, the full set of flamelet solutions are linearly interpolated into the manifold as a function of the control variables. The final manifold is discretized in 200 points in the \mathcal{Y} direction and 70 points in the h direction, with all points being equally spaced. The reader is referred to van Oijen and de Goey [2000] for more details about the storing retrieving procedure.

2.2.2.1.1 Inclusion of heat losses in the manifold

For predicting heat losses, the flamelets were solved for a range of enthalpies values, which implies that enthalpy becomes a control variable. The easiest way to change the mixture enthalpy is by changing the inlet boundary initial temperature. Thus, the flamelets were calculated for initial temperatures varying from 390 K to 240 K in steps of 30 K (following Oijen and Goey [2000]). This manifold includes conditions of heat gain (initial temperature bigger than 298 K) and heat loss (initial temperature smaller than 298 K). However, computing flamelets for even higher heat losses by continuously decreasing the

initial reactants temperature may lead to unrealistic conditions. In the literature, there is not just one method to overcome this problem Fiorina et al. [2003]. In this paper, it is considered the approach of converting part of the reactants into the corresponding products but maintaining the elementary composition unaltered.

In the present work, it is followed the approach of converting a fraction of the reactants (CH_4 and O_2) into the corresponding products (CO_2 and H_2O) at the same initial temperature (240 K). This conversion of species respects the fuel/oxidant stoichiometric proportion whereas the mixture enthalpy (due to the low enthalpy of formation of the saturated products) and the pool of atoms of the mixture is preserved. Hence, we changed the initial reactants composition by increasing the molar fraction of CO_2 and H_2O in steps of 0.01 and 0.02, respectively, (with a proportional reduction of CH_4 and O_2 molar fraction) until the flame extinguishes.

A scheme of the manifold including heat losses is shown in Figure 2.2. Unfortunately, these two methods are not able to reproduce the cold states close to the walls, where there are combustion products at low temperatures. For this region an extrapolation procedure is necessary Oijen and Goey [2000]. Here, the lowest enthalpy composition is approximated for the one obtained from equilibrium calculations at 298 K and imposing the initial composition equal to that obtained for the last flamelet solution for the maximum progress variable (Figure 2.2).

2.2.2.2 Multi-dimensional simulations

FGM simulations in multi-dimensional geometries are conducted after the database (manifold) is constructed. These simulations consist in solving laminar steady-state conservation equations of total mass, momentum and a conservation equation for each control variable. Assuming unity Lewis number, the transport equations of the control variables area given by:

$$\nabla \cdot (\rho \vec{u} \mathcal{Y}) - \nabla \cdot \left(\frac{\lambda}{c_p} \nabla \mathcal{Y} \right) = \dot{\omega}_{\mathcal{Y}} \quad (2.2)$$

$$\nabla \cdot (\rho \vec{u} h) - \nabla \cdot \left(\frac{\lambda}{c_p} \nabla h \right) = 0 \quad (2.3)$$

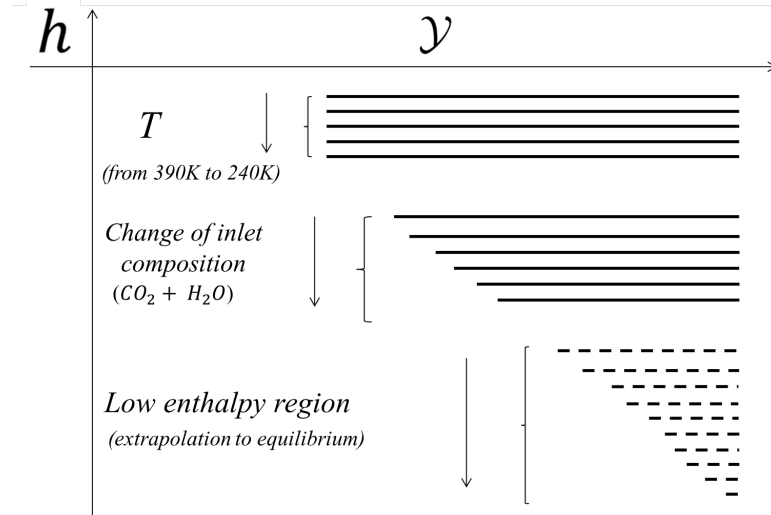


Figure 2.2 – Schematic representation of the 2D manifold with the different approaches for distinct regions. The range of the control variables is from -0.688 to 1.032 for the progress variable definition adopted and -1.56×10^{-5} to -3.00×10^{-6} for enthalpy.

Table 2.2 – Boundary conditions imposed for \mathcal{Y} and h transport equations.

Boundaries	\mathcal{Y}	h
Inlet	$\min(\mathcal{Y})$	$h(T = 298 K)$
Outlet	$\frac{\partial \mathcal{Y}}{\partial x_i} = 0$	$\frac{\partial h}{\partial x_i} = 0$
Walls	$\frac{\partial \mathcal{Y}}{\partial x_i} = 0$	$h(T = 298 K)$

where λ [W/mK] and c_p [J/kgK] are the thermal conductivity and the specific heat of the mixture, respectively. The variable $\dot{\omega}_{\mathcal{Y}}$ is the source term of the progress variable, \vec{u} [m/s] is the velocity vector and ρ [kg/m³] is the mixture density. The progress variable source term is defined as a linear combination of the chemical species source term that defines the progress variable.

$$\dot{\omega}_{\mathcal{Y}} = \sum \alpha_i \dot{\omega}_i \quad (2.4)$$

The equation system for multidimensional simulations is solved by the Fluent 16.1 software. The pressure-velocity coupling is treated by the SIMPLE method, the convective and diffusive terms are discretized by second-order schemes and a residual error of 10^{-6} is assumed as convergence criterion. The FGM technique is implemented in the software via user-defined functions, including the procedure of retrieving the information from the

manifold. The boundaries conditions are presented in the Table 2.2. Mixture thermodynamic and transport properties (as viscosity conductivity and specific heat) required for the solution of the equation system are retrieved from the manifold during run-time. After the solution of the equation system, the flame structure is reconstructed from the solution of control variables retrieving the temperature and the species mass fractions from the manifold. The look-up/retrieval scheme is based on bilinear interpolations (see APPENDIX C) between the closest values of \mathcal{Y} and h solution at each control volume of the computational domain.

2.2.3 Determination of laminar burning velocity from the two dimensional flames

The two-dimensional flame analyzed in the present work is more complex than the idealized one-dimensional canonical planar adiabatic flame. It has been shown that stretch and curvature effects may significantly change the burning velocity [Law, 2006]. Additionally, heat losses reduce the flame temperature, which has an exponential effect on the reaction rates and, consequently, on the burning velocity [Law, 2006]. In this work, the laminar burning velocity along the flame surface are extracted in order to compare the FGM and the detailed solutions. Both results are compared with the one-dimensional laminar adiabatic flame velocity.

The laminar burning velocity (S_L) is defined at the unburnt region of the flame (cold boundary). In the two-dimensional results this region is approximated by an isothermal surface with temperature equal to 315 K (which represents, approximately, 1% of the adiabatic flame temperature). Points on this isothermal surface are collected by following the temperature evolution along a certain number of streamlines as shown in Figure 2.3. Then, the points are used to reconstruct the surface by a polynomial fit. At this surface, the flow velocity (\vec{v}) is determined on its projection on the normal surface direction (\vec{n}) is obtained. This velocity multiplied by a temperature correction ($298K/315K$) is equal to the laminar burning velocity S_L .

In order to reveal the heat loss effects, a similar procedure is developed for the flame temperature. In this case, the position of the maximum heat release rate is found for each of those streamlines and the flame temperature is collected at position. Note that this temperature is not the maximum value reached by the flame, instead it is a

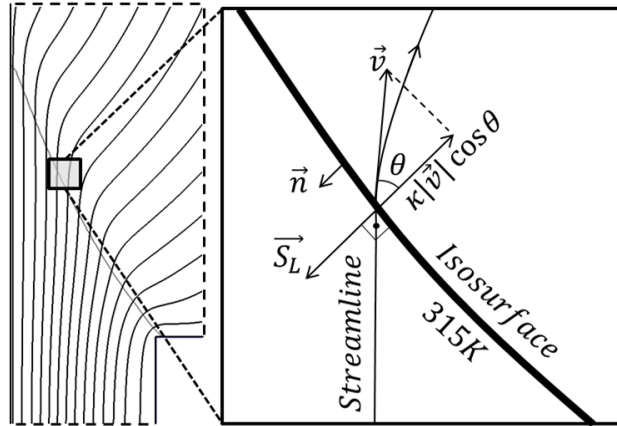


Figure 2.3 – Extraction of the burning velocity from the two-dimensional results (κ value is the ratio between $298K/315K$).

temperature that characterizes the inner structure of the flame, where most reactions are happening.

2.3 Results

In order to certify a correct implementation of FGM technique including heat losses, the Sec.2.3.1 presents a set of one-dimensional simulations of freely propagating CH_4/Air flames to validate the FGM technique with a detailed chemistry. In Sec.2.3.2, two-dimensional results are presented. The last part, a discussion about laminar burning velocity predictions is presented to verify the capabilities of the FGM technique in predicting non-adiabatic premixed flames.

2.3.1 Manifold validation

Figure 3.4 shows the validation of the present implementation in the one-dimensional freely propagating flame of CH_4/Air with stoichiometric equivalence ratio. The inlet temperature of the mixture is 298 K and atmospheric pressure is imposed. FGM results are compared with the detailed simulation (i.e, with the direct integration of the chemical kinetics and the solution of all chemical species). As explained in Section 2.2.2.1, the DRM22 kinetics mechanism is also assumed for detailed simulations. The FGM results present discrepancies in order of the 1% for both temperature and CO mass fraction when compared with the detailed simulation, suggesting that the FGM technique can

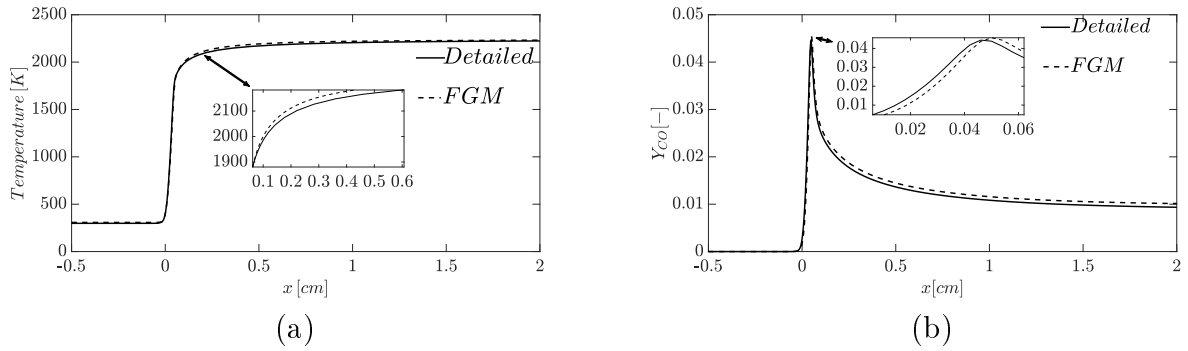


Figure 2.4 – Manifold validation for one-dimensional adiabatic freely propagating flame of CH_4/Air at $\phi = 1.0$ and atmospheric conditions. Comparison of FGM and detailed model for (a) temperature and (b) CO mass fraction.

adequately solve the flame and that the assumed progress variable definition is suitable to map the thermo-chemical space of the analyzed flame.

2.3.2 Two-dimensional simulations

Two-dimensional simulations were conducted for the configuration presented in Figure 2.1 following the FGM methodology explained in Section 2.2.2

2.3.2.1 Mesh independence test

A mesh independence test for the two-dimensional domain is performed using the FGM technique. The computational domain is discretized with equally sized quadrilateral cells. The analysis is conducted for six different meshes from 260 to 104000 volumes. Progress variable (Figure 2.5.a) and flame temperature (Figure 2.5.b) are chosen as parameter to evaluate the mesh independence. Maximum discrepancies are observed at 4.5 mm from the symmetry line. The progress variable is a scalar actually solved in the computational domain (along with enthalpy) and, consequently, have to be mesh-independent. Temperature is a scalar retrieved from the manifold.

2.3.2.2 Comparison of flame structure between detailed and FGM simulations

A comparison between detailed and FGM simulations is presented in Figure 2.6 for the maximum reactants injection velocity of 1.1 m/s. In general, a good agreement

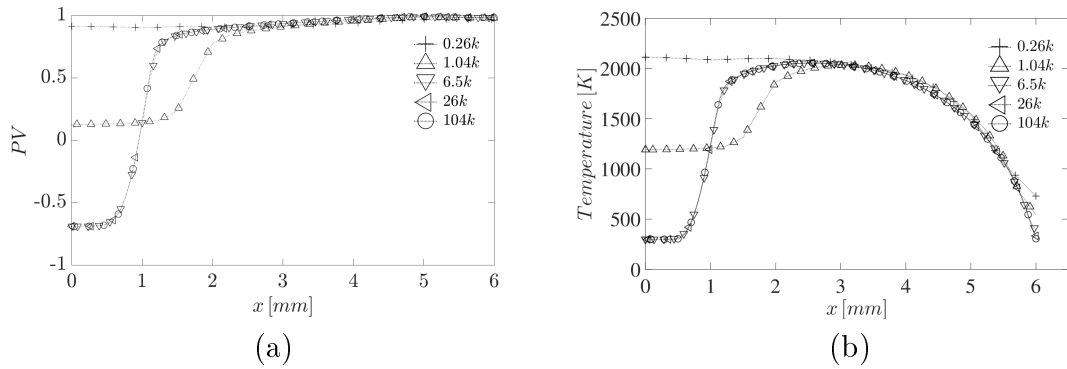


Figure 2.5 – Mesh independence test for the two-dimensional simulations: (a) progress variable profile for different meshes at 3 mm from the burner nozzle exit; (b) temperature profile for different meshes at 3 mm from the burner nozzle exit.

between the two combustion models is found. Contours of the reaction progress variable (\mathcal{Y}) presents only small differences at the flame base close to the burner (Figure 2.6.a). At this position, the FGM simulation predicted slightly lower \mathcal{Y} values. Those differences are not so evident for the contour of temperature (Figure 2.6.b), but they becomes more apparent for the OH mass fraction (Figure 2.6.c). In fact, the FGM results predicted slightly wider distributions of OH and CO (Figure 2.6.d) mass fractions in the thermally affected region. Despite that, scalars' maximum values and flame height are well predicted by the reduced kinetic mechanism approach.

Major discrepancies are found for chemically slower species as can be seen in the contours of the CO mass fraction presented in Figure 2.6.d. It is observed a significant difference in the spacial distribution of the CO mass fractions at low temperatures close to the burner rim where the flame stabilizes. At this region, the flame extinguishes due to low temperatures next to the wall and the reactants can leak through the flame envelope without being completely burnt. The detailed simulation predicted a non negligible concentration of CO around the burner, which is not predicted by the FGM simulations.

Ganter et al. [2018] performed a numerical analysis of laminar methane/air side-wall-quenching. It was found that the CO prediction using the FGM method also presented deviations close the wall. In the same work, they evaluated the CO transport applying the Lagrangian analysis and showed that higher CO concentrations close the wall are due to diffusive transport towards that location. With the intention to capture this phenomena using the reduced technique, Efimov et al. [2019] proposed a new method

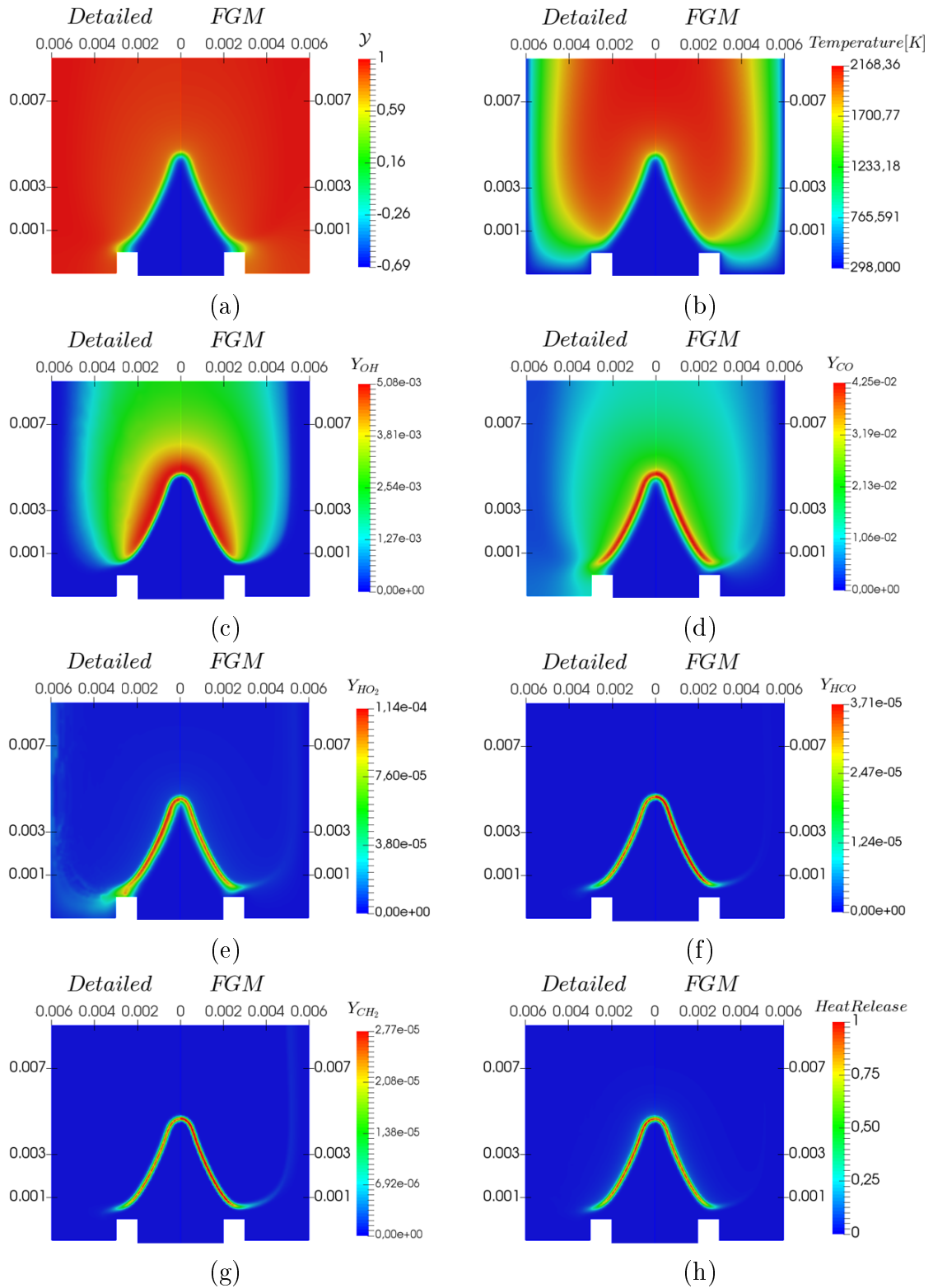


Figure 2.6 – Comparison between detailed chemistry and FGM results. Contours of: (a) progress variable \mathcal{Y} , (b) temperature, (c) OH, (d) CO, (e) HO₂, (f) HCO, (g) CH₂ and (h) normalized heat release rate.

to evaluate the flame-wall interactions (FWI) using the FGM. Referred to as Quenching Flamelet-Generated Manifold (QFM), the focus of the study was to improve the accuracy for the prediction of CO near the wall in a similar geometry of the present study. They observed a strong dependence of the CO concentrations on the enthalpy gradients close to the wall. In order to take this dependence into account, an additional degree of freedom was included in the FGM using a second reaction progress variable. Therefore, to correctly map some species on the quenching region (near to the walls) is necessary to extend the FGM technique with additional controlling variable.

Figure 2.6.e. presents the HO_2 mass fraction. Clearly some discrepancies are noticed close to the burner rim. Popp and Baum [1997] concluded that very close to the wall, in the cold region, the production HO_2 occurs via the chain-breaking $H + O_2 + M = HO_2 + M$. This reaction competes with the chain-branching reaction $H + O_2 = OH + O$ for the H radical. However, the chain-breaking reaction described above requires no activation energy and the probability of ternary collisions is increased due to high water concentration at the wall, which has very high efficiency to promote the ternary reaction. This scenario also suggests that a quenching mechanism close to the wall acting on HO_2 reactions could be captured using additional dimensions in the manifold in a similar way to the CO as described in Efimov et al. [2019].

The minor species HCO and CH_2 are presented in Figure 2.6.f. and Figure 2.6.g., respectively. The former plays a central role in hydrocarbon combustion whereas the latter is related *PAH* and NO_x formation. These species are well predicted by the FGM at the hot regions of the flame but, again, present important discrepancies at the cold regions with cold products showing once more the difficulty of the method in solving this condition. However, these discrepancies are non-essential to the overall flame behavior, since the FGM technique depends on the progress variable (and enthalpy) which is well-mapping the hot flame region as can be seen in Figure 2.6.h. for the heat release rate.

A better insight of the FGM agreement with the detailed simulation is obtained from radial profiles. Results are compared for profiles of progress variable (\mathcal{Y}), temperature and species mass fraction at 1 mm, 3 mm and 7 mm from the burner nozzle exit in Figure 2.7. These positions approximately indicate the bottom, the middle of the flame and the post-flame region. Radial profiles of the progress variable and the temperature confirms the good agreement of the FGM with the detailed simulations. A negligible dis-

placement of the FGM results is observed at the regions with higher gradients and very small differences can be observed for the progress variable (\mathcal{Y}) at the maximum radial position at 1 mm from the burner nozzle.

A good quantitative and qualitative agreement is also observed for the major chemical species (CO_2). Figure 2.8.a. confirms the capabilities of the FGM, as simplified kinetic mechanism treatment, in predicting the major chemical species with a good accuracy. As previously reported, more important differences are observed for the CO mass fraction closer to the burner nozzle and the computational domain walls. Those regions are characterized by the strong heat transfer from the flame and, therefore, by the lower temperatures. Figure 2.8.b. presents the minor chemical species. In general, a good agreement are found. The main difference is presented by HO_2 due to the cold region close to the wall, as previously discussed.

Simulations were also performed for a slightly higher for maximum reactants injection velocity of 1.33 m/s, equivalent to a velocity gradient at wall equal to 1330 1/s. This maximum velocity was found to be the limit to the occurrence the flame blow-off from performing simulations increasing the maximum inlet velocity in steps of 0.01 m/s until reach numerical instabilities. The subsequent increase of the maximum inlet velocity reduces the heat transfer from the flame to the burner until it reaches the point where the burner does not sustain the flame anymore. A comparison between detailed and FGM simulations is presented for this higher maximum inlet velocity in Figure 2.9. The flame structure of this limiting case is found to be similar to the one presented in Figure 2.6 but with a slightly higher flame length. The comparison between detailed and FGM simulations also shows a similar trend as already assumed.

Despite some discrepancies for CO and HO_2 mass fractions, the results achieved with the FGM approach presented a very good agreement with the detailed simulation but demanding only a fraction of the computational time. While detailed simulation required roughly 48 hours to converge, the FGM methodology needed only 2.4 hours (20 times faster) including the pre-processing step, i.e., the flamelet simulations and the manifold construction. Also, it should be noted that the manifold needs to be created just once for each equivalence ratio under consideration. In other words, the same manifold can be used to perform simulations of different burners subjected to different heat loss conditions.

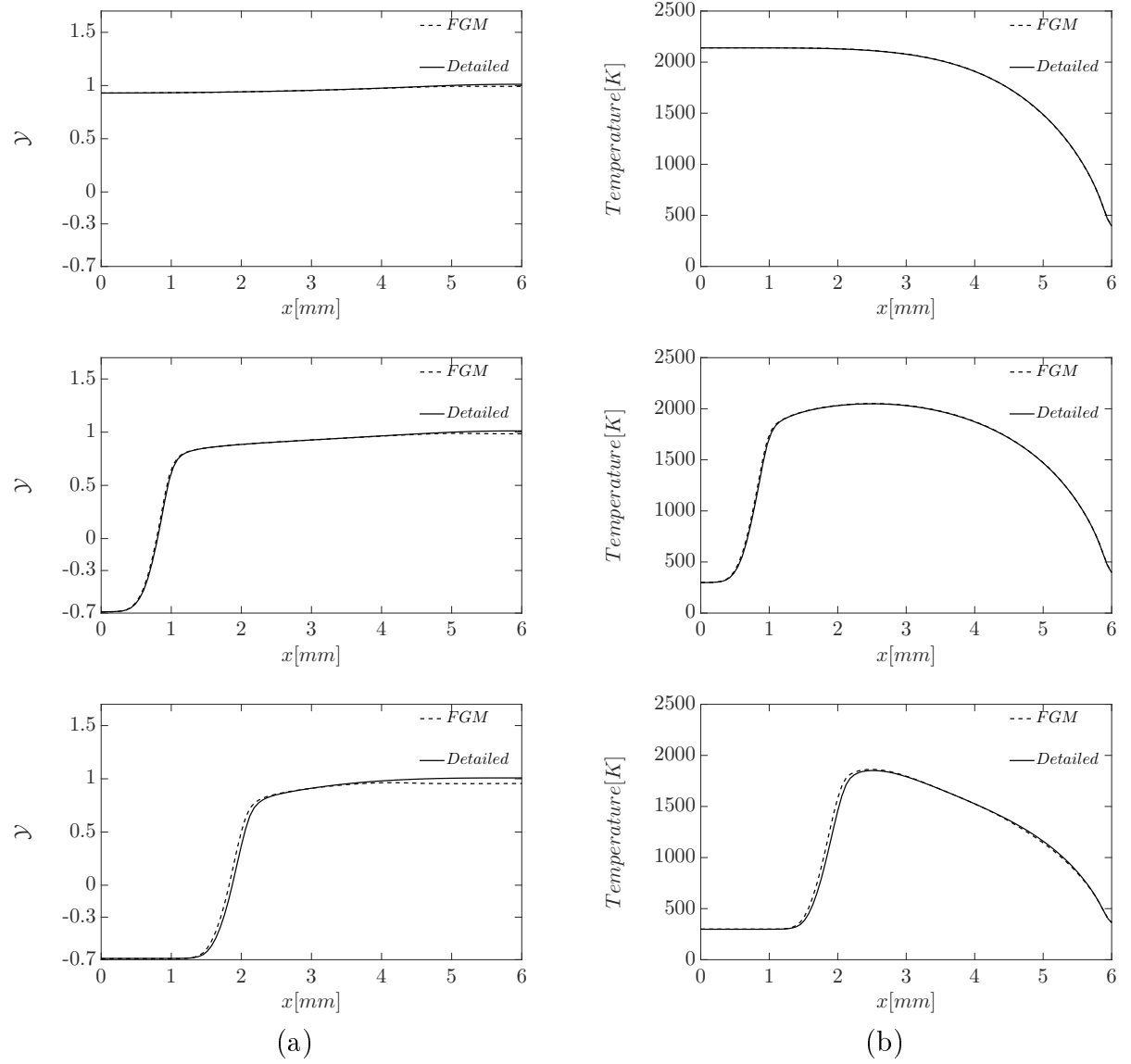


Figure 2.7 – Comparison of the reaction progress variable \mathcal{Y} (a) and the temperature (b) profiles between detailed and FGM simulations at 7 mm (top), 3 mm (middle) and 1 mm (bottom) from the burner nozzle exit. Maximum reactants velocity of 1.1 m/s.

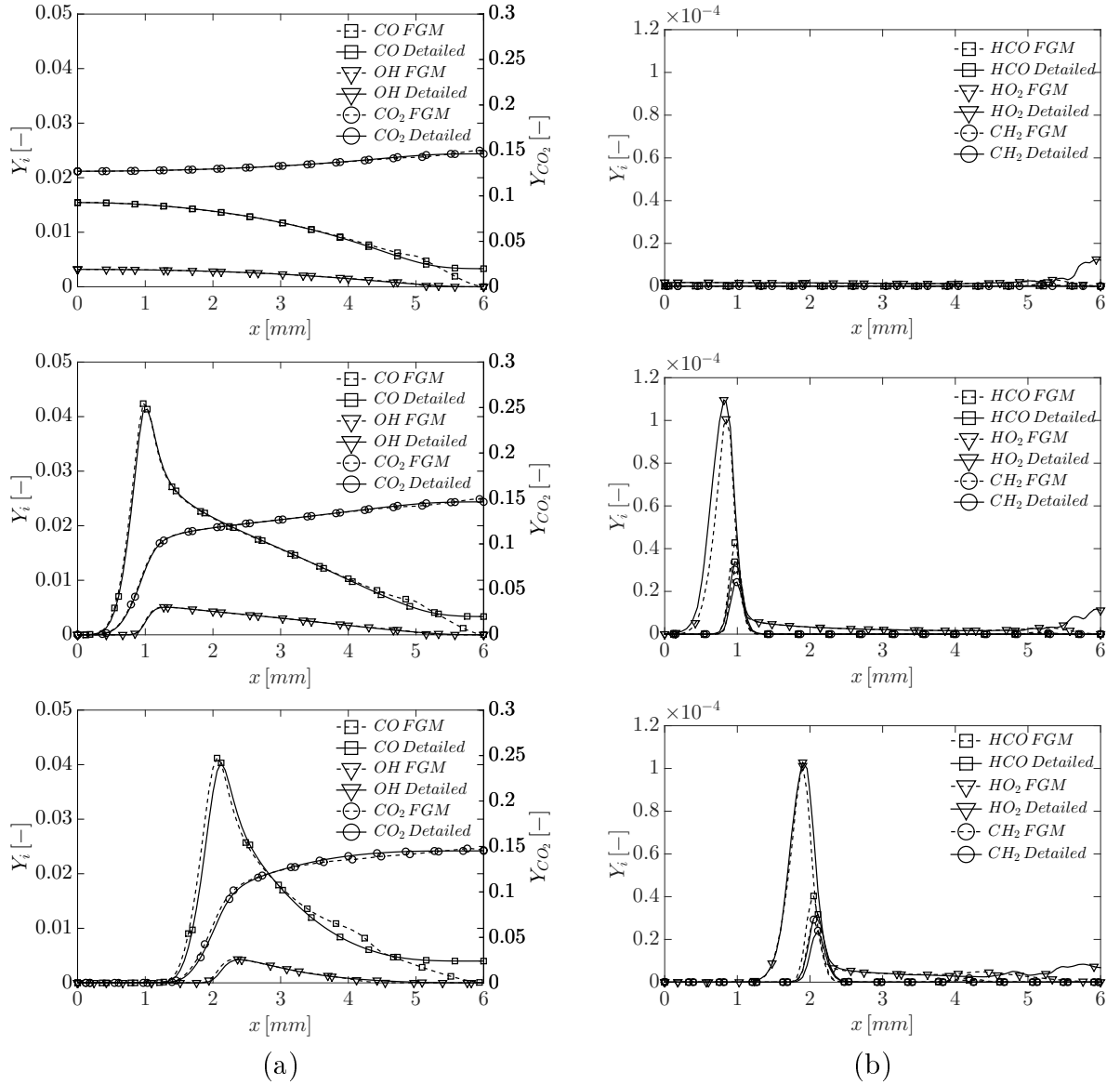


Figure 2.8 – Comparison of (a) CO, OH, CO₂ and (b) HCO, HO₂, CH₂ mass fractions profiles between detailed and FGM simulations at 7 mm (top), 3 mm (middle) and 1 mm (bottom) from the burner nozzle exit. Maximum reactants velocity of 1.1 m/s.

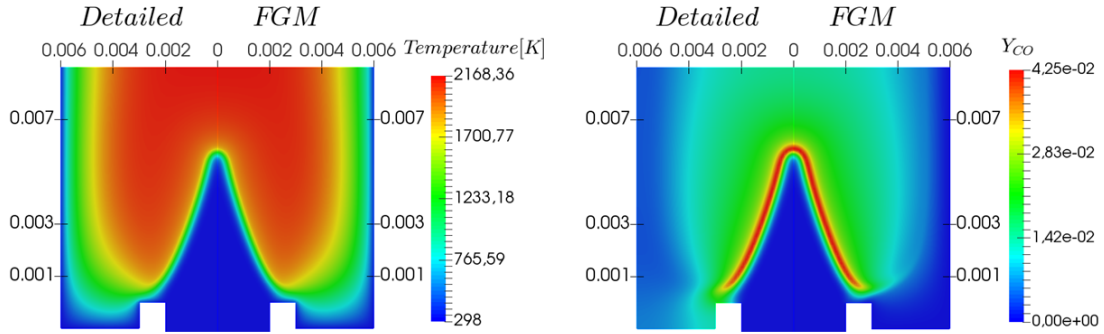


Figure 2.9 – Contours of temperature (a) and CO mass fraction for detailed and FGM simulations for the maximum reactants inlet velocity of 1.33 m/s.

2.3.3 Evaluation of the laminar flame speed

Figure 2.10.a shows the burning velocity along the flame surface (the coordinate x is the horizontal axis) for the maximum inlet velocity of 1.1 m/s. Three distinct regions are observed: one close to the burner rim, which is affected by heat losses, an intermediary region, which approaches the 1D results and a third region close to the centerline, where the flame is affected by curvature effects. The FGM and the detailed results are very similar showing, again, the good approximation obtained with the reduced technique. The behavior at the flame tip can be explained by the analysis of the Law [2006] for the burning velocity at low stretch rates which show that

$$\frac{S_l}{S_l^o} = 1 - \delta_u^o \nabla \cdot n \quad (2.5)$$

where δ_u^o is the flame thickness and $\nabla \cdot n$ represents the flame curvature (which is equal to $-2/R_f$, where R_f is the flame surface radius). Thus, the burning velocity is increased at the tip of the conical flame due to pure curvature effects. Note that stretch effects are not present since in our simulations, and it was imposed unitary Lewis number.

Figure 2.10.b presents the flame temperature at the maximum heat release rate position. It can be seen that as the distance increases, the temperature at the reaction region is reduced due to heat losses to the burner rim. This explains the decrease of the burning velocity in this region. Far from the burner walls the temperature of the reaction region reaches a plateau close to its adiabatic value. This is why the burning velocity approaches S_l^o at the intermediary region and increases due to pure curvature effects at the flame tip.

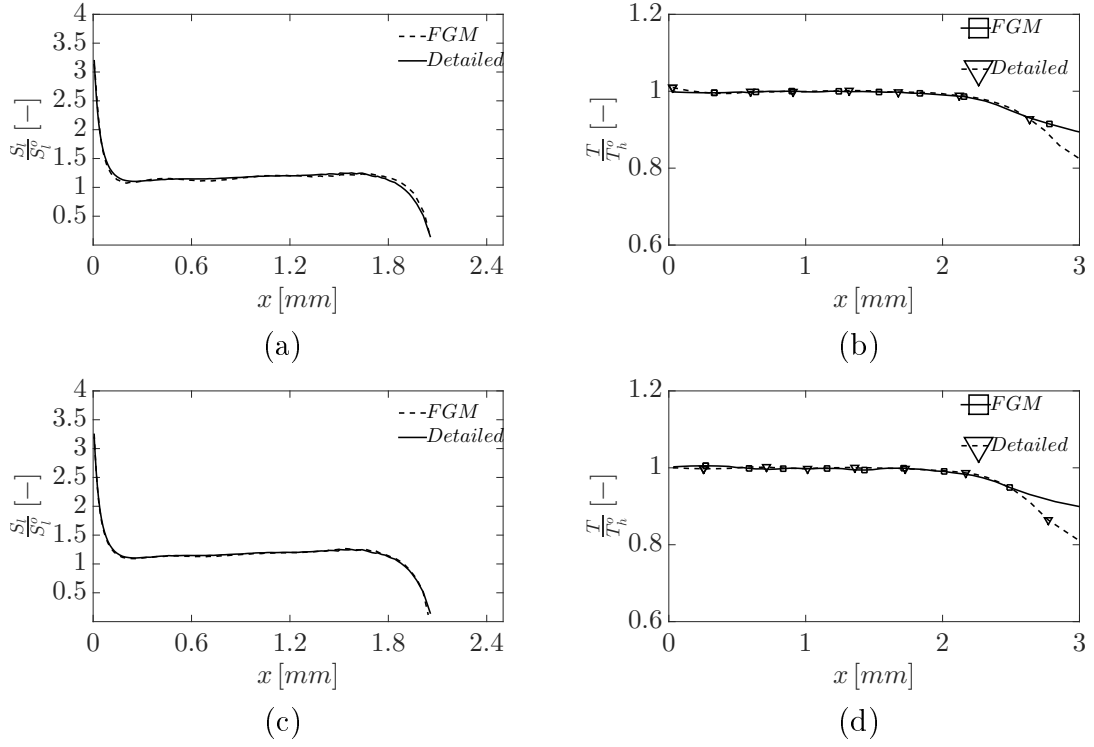


Figure 2.10 – Burning velocity (a;c) along the flame surface normalized by the 1D burning velocity ($S_l^0=29.72 \text{ cm/s}$) and temperature (b;d) at the maximum heat release rate position normalized by the same temperature from a 1D adiabatic simulation ($T_h^0 = 1721 \text{ K}$). Reactants inlet velocity of 1.10 m/s (a;b) and of 1.33 m/s (c;d).

In Figure 2.10.b it is possible to see some important differences between both numerical methods. The temperature decrease near the cold wall is more intense for the detailed simulation because the flame edge stabilizes closer to the burner rim when compared to the FGM model. From Figure 2.6.h is possible to verify that the flame envelope for the detailed formulation is anchored closer to the burner rim. It can be occurring due to recurring difficulty of the FGM in capture regions where large gradients of enthalpy are present, as discussed by Efimov et al. [2019].

Figures 2.10.c and 2.10.d show the same results for the maximum inlet velocity of 1.33 m/s. The FGM is still capable of reproducing the detailed results with very good accuracy. The flame behavior at this limiting stabilization point presents the same characteristics already discussed.

2.4 Conclusions

In this paper an implementation of the FGM technique for premixed flames with heat losses is compared to the detailed solution of the conservation equations. The problem is a premixed laminar flame stabilized on a slot burner. The FGM technique presented very good qualitative and quantitative results when compared to the reference model even for a flame close to the blow-off limit. The many discrepancies occurred due to difficulties in mapping the thermochemical state of the system near the walls where combustion products at low temperature are found.

A detailed comparison of the burning velocity along the flame surface revealed the effects of the heat loss to the burner rim and the pure curvature effect at the flame tip. The present study explores the $Le = 1$ condition. For fuels with Lewis numbers far from the unity, another formulation of the FGM would be necessary to take preferential diffusion into account. In the present case, the FGM technique was able to capture the flame behavior with good agreement with the detailed model.

3 NUMERICAL STUDY OF FLAME STABILITY WITHIN INERT POROUS MEDIA SUBJECTED TO FLOW OSCILLATIONS

3.1 Introduction

Porous Media Combustion (PMC) technology have applications in different fields as curing and drying processes at many materials (paint, paper, ceramic, grains, metals, resins) and still are subject of study in areas as micro combustors [Giovannoni et al., 2016], gas turbine [Djordjevic et al., 2012], domestics cooking stoves [Pantangi et al., 2011; Zeng et al., 2017], lighting [Qiu and Hayden, 2006], boilers [Yu et al., 2013], heat exchangers [Amatachaya and Krittacom, 2017]. In Mujeebu et al. [2009] is possible to find a comprehensive review about applications using PMC. In PMC, the flame is stabilized within a porous matrix generating a heat recirculation from the post-flame to the pre-flame zone through conduction and solid-to-solid radiation, which creates an excess enthalpy at the reaction region [Takeno and Sato, 1979; Hsu et al., 1993]. This regenerative heat mechanism brings a favorable set of characteristics as the potential to operate in ultra-lean combustion regime, low pollutant emissions, and high power densities.

Moreover, a porous burner is typically characterized by a large turn-down ratio [Keramiotis et al., 2012], i.e., a wide range of reactant flow rates for which the flame can be stabilized within the solid matrix. This happens because the interphase heat transfer changes as the flame moves inside the matrix modulating the heat recirculation which leads to different burning velocities. This characteristic allows for multiple points of equilibrium between the flow velocity and the burning velocity. In a typical configuration a porous burner is formed by two layers of ceramic foams. A first layer, called preheating region, with small pores and a second layer, called combustion region, with larger pores. The flame is usually stabilized at the interface. Some studies that numerically explored the stability using this configuration are Barra et al. [2003]; Smucker and Ellzey [2004]; Liu et al. [2010]; Horsman and Daun [2011]. Flame stability in others configurations were studied as well as graded porosity [Sobhani et al., 2018], divergent domain [Hashemi and Hashemi, 2017; Bakry et al., 2011], and gap between the porous layers [Gao et al., 2017]. Recently, Ellzey et al. [2019] presented a comprehensive review about heat recirculating reactors research with an emphasis on the most important designs and applications.

Many authors explored PMC numerically in transient regime. Lammers and

De Goey [2003] studied 1D stationary and unsteady calculations to evaluate the flashback on surface porous burners, and stabilization maps were obtained for submerged and surface flames. They showed that when the outlet surface of the burner faces a hot environment, the flames may move upstream to find a new stable position. Zheng et al. [2011] evaluated the flame and the mechanism of inclinational instability of filtration combustion. The 2D simulation with a one-step mechanism was used, and the results showed that the development of inclinational instability can result in a separation of the flame front in multiple flames zones. Chen et al. [2018] evaluated experimentally and numerically (2D model) the transient effects of initial inhomogeneous preheating distribution on the flame inclination instability in porous media burner. To reduce computational time, a single-step reaction mechanism of CH_4/air was used. The results suggested that smaller equivalence ratio, high gas inlet velocity, and initial preheating temperature perturbation can increase the inclination profile. Yakovlev and Zambalov [2019], implemented a sophisticated three-dimensional model considering pore-scale in an inert porous media under the condition of downstream combustion wave. The representation of a non-uniform packed bed was simulated using particles falling under the gravity force. The model considered a detailed kinetics and solid-to-solid radiation in a transient approach. The results showed that the radiation contributes to the heat transfer in the bed region where there is a large temperature gradient. The combustion wave propagation is quasi-steady, however different subregions of the flame propagated differently depending on the porous distribution.

Although transient studies are found, they are relatively rare for stabilized flames within porous media. For example, it has not been found studies imposing an oscillation of the mass flux rate of reactants at the inlet boundary condition in PMC simulations. This condition could happen in a non-desired oscillation on the gas supply line due to some control failure. The porous matrix is expected to increase the thermal inertia of the system, but the time and the limits for flame re-stabilization have not been investigated yet. Thus, the objective of the present work is to explore the transient response of stabilized flames within porous media to pulses in the inlet mass flux rate. To this purpose, a one-dimensional model is employed assuming non-equilibrium between gas and solid phases. The chemical kinetics is taken into account with the Flamelet Generated Manifold (FGM) reduction technique, which is able to include information from detailed

kinetic models with reduced computational time.

3.2 Method

3.2.1 Model Description

With the purpose to evaluate the transient response of porous burners to flow perturbations, a one-dimensional volume averaged model is built considering non-equilibrium between the phases. Transport equations for the total mass, solid-phase energy, gas-phase energy and progress variable are solved as will be shown next. Imposing one-dimensional approach, the momentum equation can be omitted to close the system of equations and the pressure drop across the porous matrix is ignored. The pore-level Reynolds number is of the order of 100, characterizing a laminar regime. The continuity equation is given by

$$\frac{\partial \rho_g}{\partial t} + \frac{\partial \rho_g u}{\partial x} = 0, \quad (3.1)$$

where ρ_g [kg/m^3] and u [m/s] represent the density and velocity of the gas phase, respectively. Gas density has been obtained from ideal gas equation state $\rho_g = PMW_{mix}/R_u T_g$, in which P [Pa] is the pressure assumed to be equal to 1 *atm*, the MW_{mix} [kg/mol] is the average molar mass, R_u [$J/mol.K$] and T_g [K] are gas constant and gas temperature, respectively.

For the solid phase, the energy transport is described by

$$(1 - \varepsilon)\rho_s C_s \frac{\partial T_s}{\partial t} - \frac{\partial}{\partial x} \left(k_{eff} \frac{\partial T_s}{\partial x} \right) = h_v (T_g - T_s), \quad (3.2)$$

where ε is the porosity, h_v [$W/m^3 K$] is the volumetric heat transfer coefficient between the solid and the gas. The correlation used to estimate h_v is $h_v = k_g Nu/d_p^2$, where the k_g [$W/m.K$] is the gas thermal conductivity, and the Nusselt number is given by $Nu = CRe^m$ [Younis and Viskanta, 1993] and pore diameter (d_p) is equals to 1.52 mm. The $k_{eff} = (1 - \varepsilon)k_s$ [$W/m.K$] is the effective solid thermal conductivity of the porous medium. For a first order approximation, it is assumed that the solid thermal conductivity (k_s) does not vary with temperature. Besides, the solid-solid radiation is neglected. Although neglecting the intra-phase radiation heat transfer for the solid is an important simplification assumed in the present model, it leads to an easier interpretation of the results since heat recirculation depends only on the solid-phase heat diffusion. For optically

thick media, the radiation may also be approximated as a diffusion process. This approach is known as the Rosseland model, and it has been implemented by many authors [Bouma and De Goey, 1999; Yang et al., 2009; Liu et al., 2015; Li et al., 2016] that increases the local effective thermal conductivity of the matrix. So, as a qualitative first approximation, many levels of the solid-phase conductivity are evaluated in order to find the effect on the flame stability of the heat recirculation enhancement (that may be thought as being related to the increase of the intra-phase radiation effect or the effect of a high thermal conductivity material). The $\rho_s = 510 [kg/m^3]$ in the Equação 4.4 is the solid density, $C_s = 824 [J/kg.K]$ is the solid specific heat and $T_s [K]$ is the solid temperature.

The gas phase energy transport is implemented using the enthalpy ($h [J/kg]$) formulation due to the ease of handling when the reduced technique FGM is implemented. Thus, the final form imposing unity Lewis for all species is described as

$$\frac{\partial(\varepsilon\rho_g h)}{\partial t} + \frac{\partial(\varepsilon\rho_g u h)}{\partial x} - \frac{\partial}{\partial x} \left(\varepsilon \frac{k_g}{C_g} \frac{\partial h}{\partial x} \right) = h_v(T_s - T_g). \quad (3.3)$$

where $C_g [J/kg.K]$ is the gas specific heat and k_g is the gas thermal conductivity.

To model the flame chemistry it is employed the FGM technique [van Oijen et al., 2001]. Although it has been widely used the model premixed flames [Van Oijen et al., 2016], studies the FGM in PMC are scarcely found in literature [van Oijen et al., 2001; Lammers and De Goey, 2004]. In the present study, flamelet solutions are obtained for different levels of gas enthalpy and stored in a database (a manifold) as a function of h and progress variable (\mathcal{Y}). After the manifold construction is obtained, simulations are conducted solving only the conservation of total mass, solid temperature, and the transport equations for h and \mathcal{Y} . Thereby, the solution of the conservation equations of each chemical species is not required as in detailed simulations. Once the convergence is achieved, the structure of the flame is reconstructed from the manifold with the control variables solution.

The conservation equation for the \mathcal{Y} is described by:

$$\frac{\partial(\varepsilon\rho_g \mathcal{Y})}{\partial t} + \frac{\partial(\varepsilon\rho_g u \mathcal{Y})}{\partial x} - \frac{\partial}{\partial x} \left(\varepsilon \frac{k_g}{C_g} \frac{\partial \mathcal{Y}}{\partial x} \right) = \varepsilon \dot{\omega}_{\mathcal{Y}}. \quad (3.4)$$

In present study a definition used to describe \mathcal{Y} [Donini et al., 2015a] is

$$\mathcal{Y} = -\alpha_{O_2} Y_{O_2} + \alpha_{CH_4} Y_{CH_4} + \alpha_{H_2O} Y_{H_2O} + \alpha_{H_2} Y_{H_2}, \quad (3.5)$$

where the α_i is equals to $10^{-2}/MW_i$. The progress variable source term ($\dot{\omega}_Y$) is determined as a linear combination of the chemical species source terms (ω_i) following the progress variable definition: $\dot{\omega}_Y = \sum_i \alpha_i \omega_i$. This parameter is also stored in the database and it is retrieved during the simulation. To calculate k_g with reduced computational cost, the following equation is considered [Smooke and Giovangigli, 1991a]:

$$k_g/C_g = 2.58 \times 10^{-5} (T_g/298)^{0.69}. \quad (3.6)$$

Flamelet libraries

The flamelet library is generated from adiabatic one-dimensional free flame solutions for a specific equivalence ratio. They are obtained for different levels of enthalpy (h) using Chem1d software. In order to guarantee that the database includes all enthalpy levels, it is necessary to create flamelets using three distinct procedures as shown in the Figure 3.1. First, the flamelets are calculated for initial temperatures varying from 780 K to 240 K in steps of 30 K. The upper limit is necessary due to the excess enthalpy typical of porous media with submerged flames. The lower limit is defined by the burner heat losses. In the region close to the outlet boundary, there is a mixture of burnt gases with a reduced temperature due to the exchange heat of solid phase. To achieve the low enthalpies of this region a second approach is employed in which a fraction of the reactants (CH_4 and O_2) is converted into the corresponding products (CO_2 and H_2O) at the same initial temperature (240 K) respecting the fuel/oxidant stoichiometric proportion. Hence, we changed the composition of the initial reactants by increasing the molar fraction of CO_2 and H_2O in steps of 0.01 and 0.02, respectively, (with a proportional reduction of CH_4 and O_2 molar fraction) until the flame extinguishes. Finally, an extrapolation between the last flamelet converged and an equilibrium condition for the burnt gases at 300 K is required. This methodology is proposed by van Oijen and de Goey [2000].

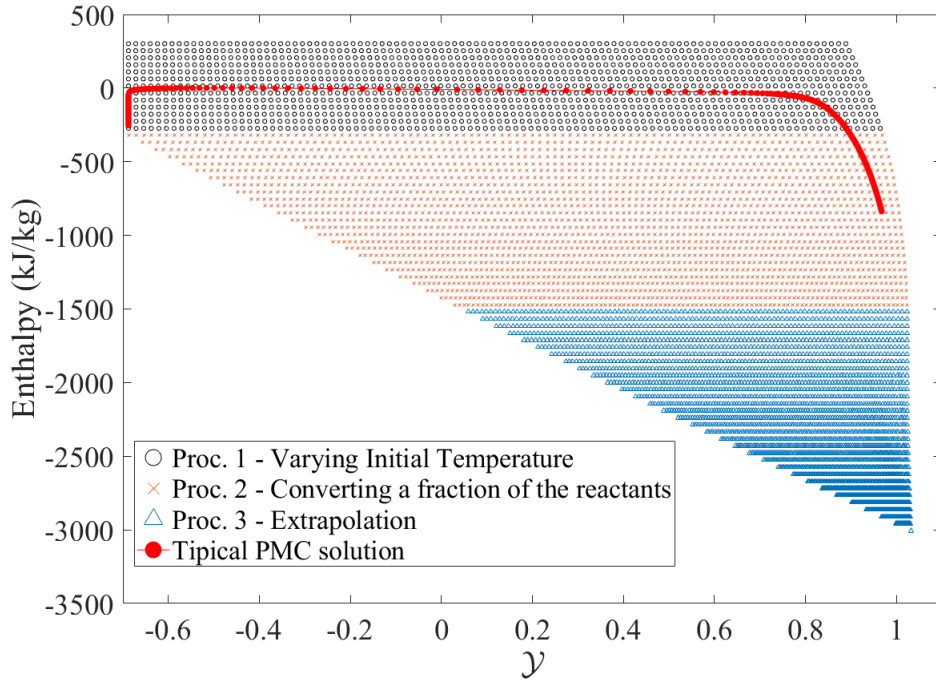


Figure 3.1 – Representations of the two-dimensional manifold \mathcal{Y} versus h . Symbols represents points mapped on the database according to the method for controlling the enthalpy. Red circle represents case PMC used when the FGM simulation with $u_{in} = 0.41$ m/s was performed ($\varepsilon = 0.8$, $k_s = 10$ W/m.K).

Finally, the thermophysical properties C_g , k_g , μ_g , ρ_g , $\dot{\omega}_Y$ and variables of interest (T_g and CO) are stored in the manifold as a function of \mathcal{Y} and h (Figure 3.2).

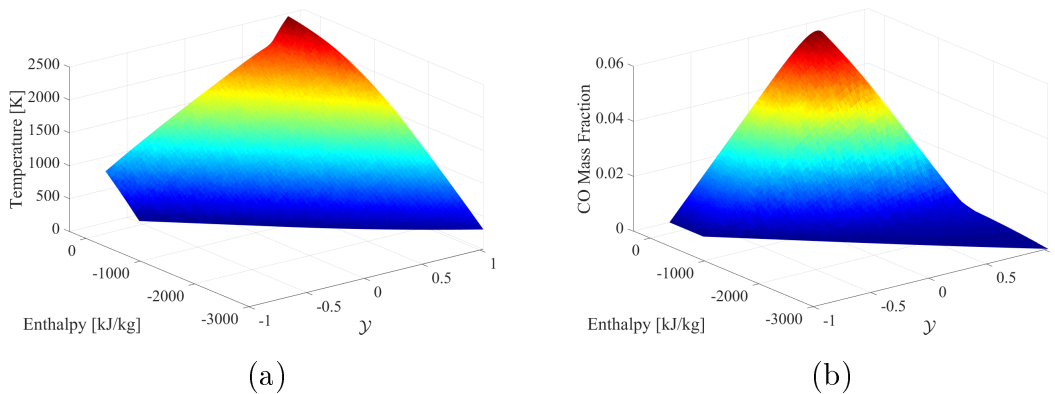


Figure 3.2 – Three-dimensional manifold (a) gas temperature (b) CO mass fraction.

3.2.2 Domain and Boundary Conditions

The present study solves a one-dimensional PM with 10 mm in length. Three levels of porosity (ε) are evaluated, 0.6, 0.7, and 0.8. The solid thermal conductivity (k_s) is also evaluated in three levels 0.1, 1.0 and 10.0 W/m.K. The inlet gas flow temperature and the environment temperature (T_∞) are both assumed to be 300 K. The emissivity at the boundaries is assumed equal to 1.0.

The transient oscillation of the inlet mass flux rate evaluated is based on a step function as defined as follows (Figure 3.3). The initial mass flux rate condition (IC) for each case is the blowoff limit, and the step function (A) is imposed after 1×10^{-3} seconds (D) for all cases. During the present study, A is determined by $A = F^* \times IC$, where F^* is a multiplicative factor, and T is the time of the pulse. In order to evaluate the blowoff limit in a steady state, the mass flux rate has been increased with steps of $0.01 \text{ kg/m}^2.s$ until the flame is pushed through the outlet surface of the burner. The blowoff limit is the last stable flame obtained in steady state.

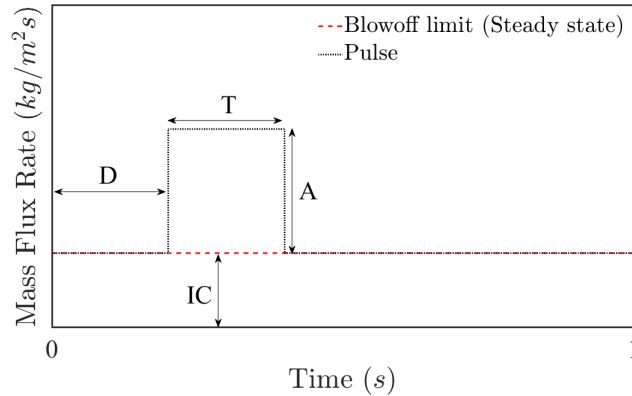


Figure 3.3 – Schematic transient boundary inlet condition imposed in the present study.

All cases were evaluated for one second. The CH_4/air equivalence ratio imposed is 1.0. The remaining boundary conditions are presented in Table 4.1. For \mathcal{Y} and h a prescribed value are imposed at the inlet and zero derivative at the outlet. For T_s , the radiative heat losses are imposed at both boundaries. The Dirichlet conditions is imposed for the gas-phase at the inlet surface. This simplification is possible because this study evaluates conditions near the blowoff limit, when the flame is far from the inlet. Implementing the gas-phase diffusion flux at the inlet results is a difference of the

inlet temperature that is less than 1 %.

The FGM technique is implemented employing the DRM22 mechanism (22 species and 104 reactions) [Kazakov and Frenklach, 1995]. In order to validate the FGM implementation, the chemistry was also carried out using the same mechanism with the Direct Integration (DI) method.

Table 3.1 – Boundary conditions imposed for T_s , \mathcal{Y} and h transport equations.

Boundary	Inlet	Outlet
T_s	$-k_{eff} \frac{\partial T_s}{\partial x} = \sigma(T_s^4 - T_\infty^4)$	$-k_{eff} \frac{\partial T_s}{\partial x} = \sigma(T_s^4 - T_\infty^4)$
\mathcal{Y}	$\min(\mathcal{Y})$	$\frac{\partial \mathcal{Y}}{\partial x} = 0$
h	$h(T_g = 300 \text{ K})$	$\frac{\partial h}{\partial x} = 0$

Numerical Solution

The equation system is solved by the commercial software package Ansys Fluent 16.1. The following transport equation for T_s , h , and \mathcal{Y} have been implemented using User-Defined Scalar (UDS). The FGM technique's implementation is via User-Defined Functions (UDF), including the procedure of retrieving the information from the manifold. The h_v modeling and the source term $h_v(T_s - T_g)$ were also implemented using UDF approach.

The convective and diffusive terms are discretized by second-order, and the transient term is discretized by the first-order scheme. A residual error of 10^{-6} is assumed as the convergence criterion except for the energy equations (T_s and h) that were imposed 10^{-8} . Both methodologies (DI and FGM) are started imposing T_s equals to 1600 K to obtain the steady-state convergence. For the detailed formulation the initial gas temperature imposed is 2000 K, and to FGM technique the initial value of progress variable and enthalpy are $\mathcal{Y} = \mathcal{Y}_{max}$ and $h = -25.4 \text{ kJ/kg}$. The under-relaxation factor necessary to start correctly the FGM method is 0.9 for \mathcal{Y} , h and T_s to avoid divergence in the first iterations. The other parameters used to obtain the solution are standard values of software.

3.3 Results and Discussion

The results and discussion are divided in three subsections. The first subsection compares the FGM technique and a direct integration (DI) formulation in steady state and transient simulations. The second subsection presents a study in steady state conditions evaluating the effects of porous medium properties and flames stabilized on the blowoff limit. The last subsection evaluates the behavior of porous burners when subjected the inlet flow oscillations.

3.3.1 Comparison between direct integration and FGM technique

A steady-state comparison between DI and FGM technique is depicted in the left column of Figure 3.4. It is presented two different steady-state conditions. A good quantitative agreement is obtained for T_g , T_s and CO. In the right column of Figure 3.4 it is presented a simulation in transient regime. The initial condition imposed is a converged flame in steady-state with $v_{in} = 0.41$ m/s. Then, it is imposed a pulse with $F^* = 0.2$. The total time considered is 0.1 s with the pulse starting at in 10^{-3} s. The results present a good agreement even with this sudden change in the inlet boundary condition.

A computational time comparison between DI and FGM is presented in table 3.2. Firstly, a test was performed considering a constant profile with gas and solid temperature equal to 1500 K and the mass fraction along with the domain of $\phi_{CH_4/air} = 1$ as the initial guess. It is emphasized that a high initial temperature (T_g and T_s) is necessary for flame ignition (even for steady-state regime). Secondly, the computational time was evaluated by imposing a previous solution as the initial guess and reducing the mass flux inlet by 10 %. The DI with a one-step mechanism was also included in table 3.2 for comparison purposes. The FGM presents significant gains relative to the two other approaches, which is an important advantage for transient simulations. It is noteworthy that the computational time spends to generate the flamelets was not taken into account.

Table 3.2 – Computational time evaluated for each method in steady state regime. Each unity correponds to 1270 seconds [†].

Method	Constant profile	Previous solution
FGM (DRM22)	1.0	0.6
DI (1-step)	14.1	10.7
DI (DRM22)	31.4	19.0

[†] The tests were performed imposing a serial processors.

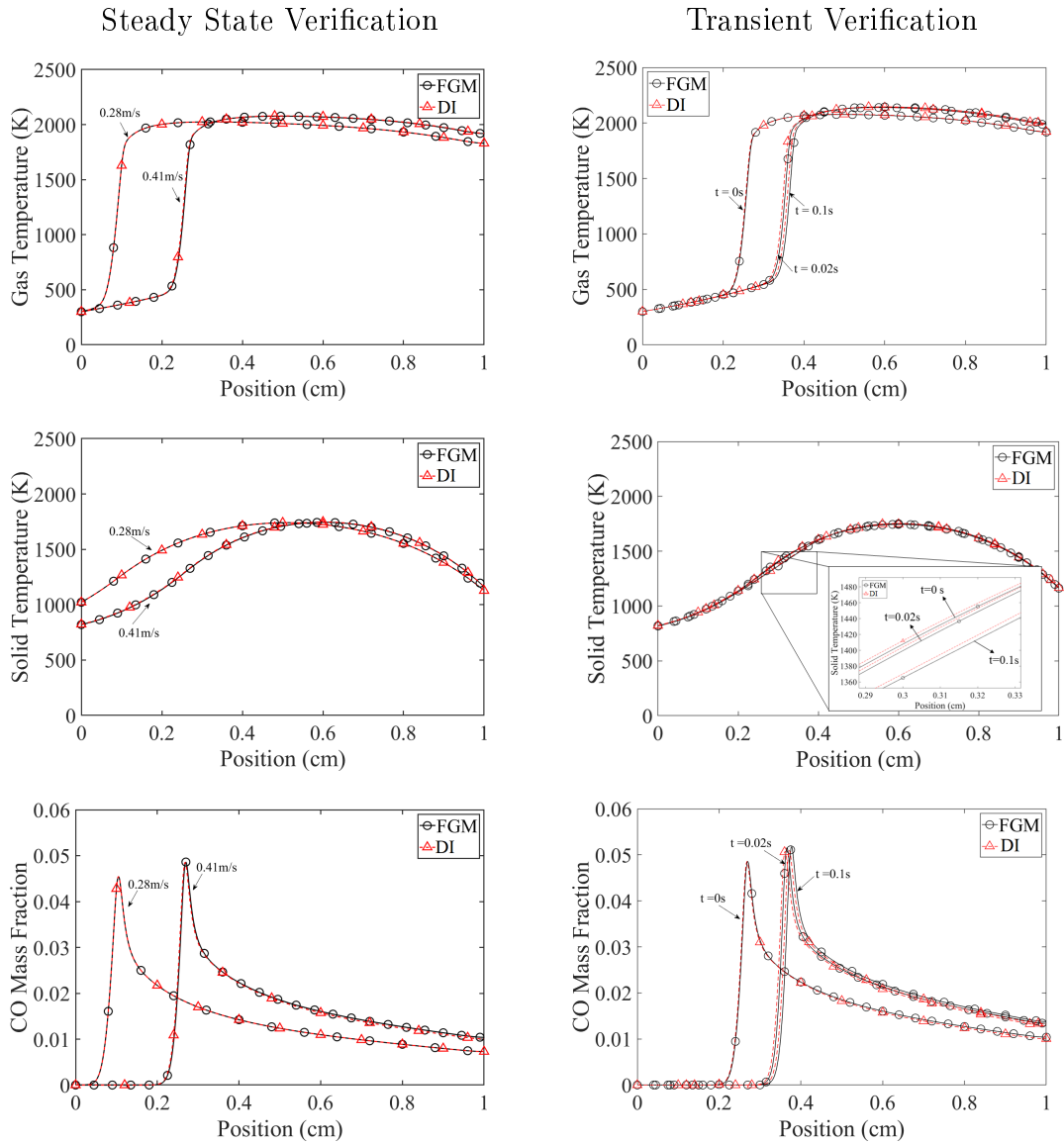


Figure 3.4 – (Left column) Comparison of FGM technique and DI method for the T_g (top panel), T_s (middle panel) and Y_{CO} (bottom panel) ($v_{in} = 0.28$ m/s and $v_{in} = 0.41$ m/s). (Right column) Comparison of FGM technique and DI method for the gas

temperature for time = 0 s, 0.02 s and 0.1 s. The initial condition with 0.41 m/s. The porosity considered is equals to 0.7, solid thermal conductivity equals to 1 W/m.K and

F^{*} equals to 0.2.

3.3.2 Steady State Stability

3.3.2.1 Evaluation of porous medium properties

To characterize the radiation heat losses at the outlet surface, a radiation efficiency (η_{rad}) is defined as

$$\eta_{rad} [\%] = 100 \left| \frac{\sigma(T_{s,surf}^4 - T_{\infty}^4)}{\dot{m}_{CH_4}'' LHV} \right|, \quad (3.7)$$

where the LHV is lower heating value and \dot{m}_{CH_4}'' is the CH_4 mass flux rate. $T_{s,surf}$ is the solid's surface temperature on the outlet boundary. The flame front position (x_f) is defined at the maximum heat release rate (HRR_{max}) as shown in Figure 3.5. The region of gas-phase preheating by solid-phase is defined as the region between the inlet and the point where the solid and gas temperature are equal. The volumetric heat convection source term ($q_v = h_v(T_g - T_s)$) and highlights corresponding to the total heat recirculated by the porous matrix ($\dot{Q}_{rec} = \int_0^{x(T_g=T_s)} q_v dx$). The heat recirculation efficiency (η_{rec}) is determined as

$$\eta_{rec} [\%] = 100 \left| \frac{\dot{Q}_{rec}}{\dot{m}_{CH_4}'' LHV} \right|. \quad (3.8)$$

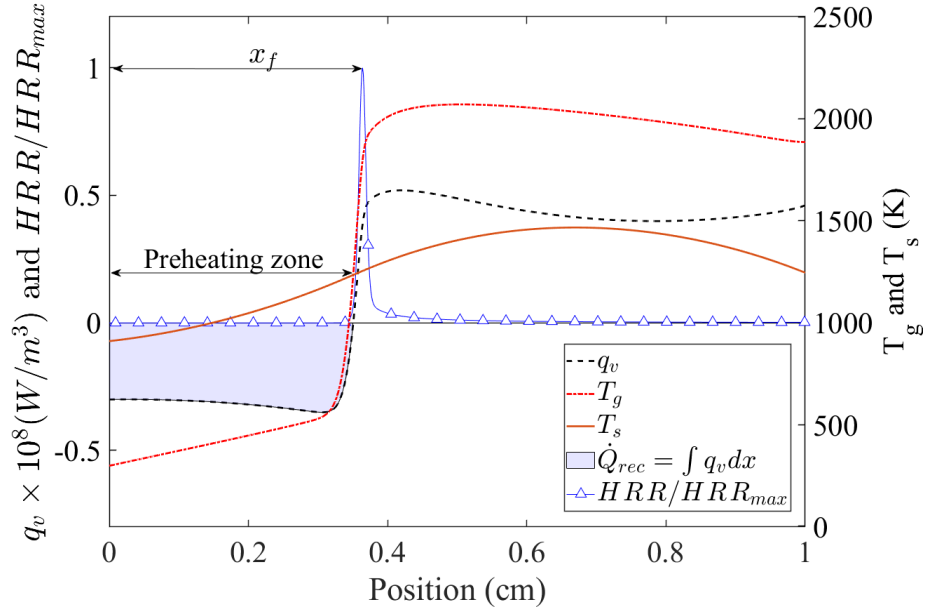


Figure 3.5 – Heat release rate position normalized and convective heat exchange between gas and solid phase ($k_s = 5 \text{ W/m.K}$, $\varepsilon = 0.8$, $v_{in}/s_F^0 = 1.41$). Burning velocity (s_F^0) is assumed equals to 29.72 cm/s ($Le = 1$) when the temperature is equals to 300 K (DRM22).

Figure 3.6 (a) presents the effect of porosity on the gas and solid temperature. Varying the porosity from 0.8 to 0.6, the location of the flame front moves downstream. For a constant mass flux rate, the pore-level velocity increases with the reduction of porosity. Thereby, the gas phase needs a greater preheating to become stable again which is achieved at a position further downstream. Figure 3.6 (b) is presented the effect of k_s on the T_g and T_s profile considering the same mass flow rate. T_g presents a lower temperature downstream of the flame front when k_s is increased. It occurs due to the T_s profile presenting lower temperature and being more homogenous when the k_s increases. Figure 3.6 (c) shows that the lower porosity requires a higher η_{rec} for achieving a stable flame while the Figure 3.6 (d) shows that a similar η_{rec} is necessary to stabilize the flame when k_s is increased.

An interesting behavior to be analyzed is that of the peak of T_g . It has a small difference when the porosity is changed although the gas preheating is higher when the ε is reduced (Figure 3.6 (a)). Figure 3.7 presents the methane source term ($\varepsilon\dot{\omega}_{CH_4}$) and the heat release rate (εHRR) for the case 0.6 and 0.8. The minimum value of $\varepsilon\dot{\omega}_{CH_4}$ is

centralized in zero to facilitate the comparison. The $\varepsilon\dot{\omega}_{CH_4}$ peak is higher for $\varepsilon = 0.6$ showing that a higher preheating brings a narrow and higher peak. However, a higher velocity due to the reduced void area ($h_v(\text{Re})$) increases the heat exchange between the gas and the solid phase after x_f resulting in a lower gas temperature difference between 0.6 and 0.8 when compared with the pre-flame region. Moreover, the effective solid thermal conductivity increases when the ε is reduced ($k_{eff} = k_s(1 - \varepsilon)$). It increases the solid-to-solid heat transfer reducing the solid temperature downstream from the flame and increasing the heat exchange between the phases.

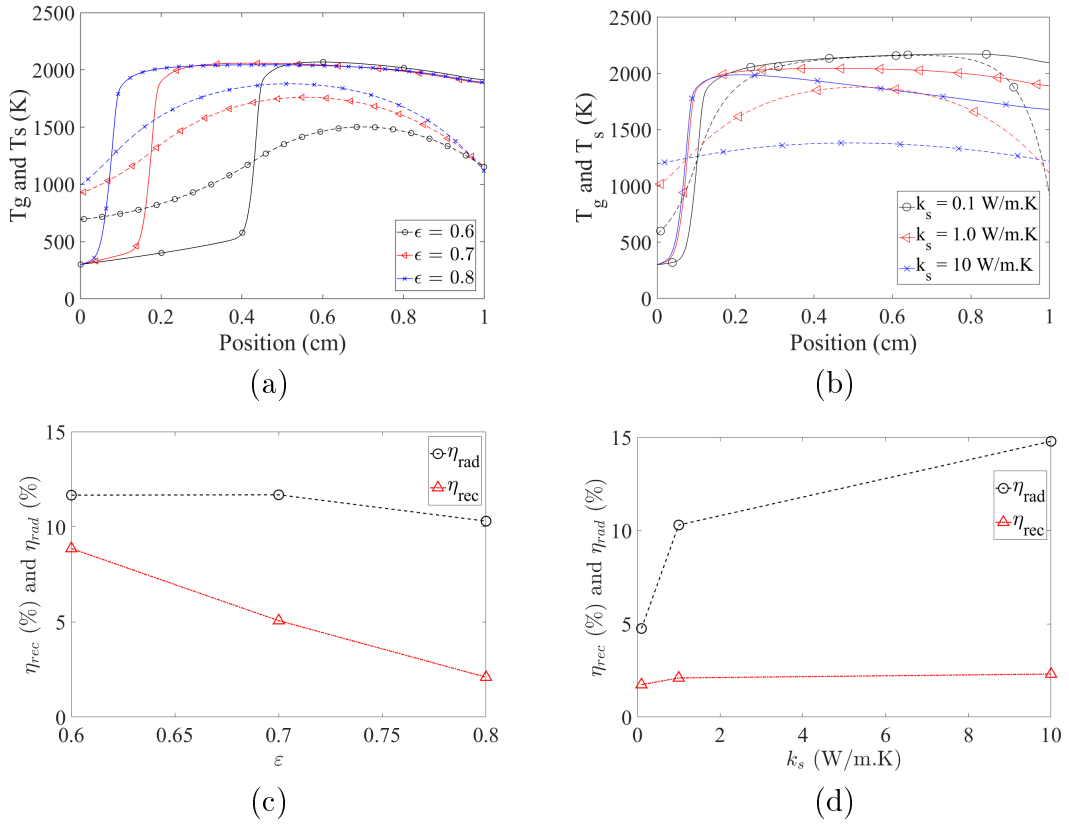


Figure 3.6 – (a) Effects of porosity ($k_s = 1$ W/m.K) and (b) solid thermal conductivity ($\varepsilon = 0.8$) on the T_g and T_s and their respective values (c and d) of η_{rec} and η_{rad} . The mass flux rate is maintained equals to $0.28 \text{ kg/m}^2.s$

The effect of k_s at the temperature profile is presented in Figure 3.6 (b). When k_s increases, T_s profile becomes more homogeneous due to the more effective solid thermal diffusion. This smoothing of T_s gradients increases the solid temperature close to the inlet region, which increases the preheating zone of the gas phase (Figure 3.6 (d)). The result is a flame front closer to the inlet boundary for larger thermal conductivity, since it requires

less space to reach the necessary preheating level. For $k_s = 0.1$ W/m.K an increase of T_g is observed after x_f . This occurs due to high values of T_s at the post-flame region, which reduce the inter-phase heat transfer, and the long tail of the HRR (not shown), which are due to the slow conversion of CO and CO₂. For large values of k_s , this small heat release rate is overcome by the inter-phase heat transfer. When k_s is increased, the η_{rad} also goes up due to more effective solid thermal diffusion. The consequence is a lower temperature of the gas phase. In contrast, the T_g profile close to the outlet is similar when the porosity is varied (Figure 3.6 (a)), following the η_{rad} that presented a smooth variation (Figure 3.6 (c)).

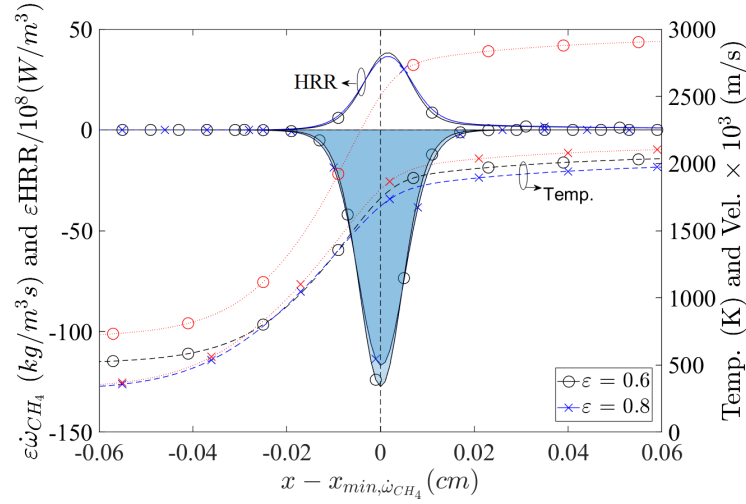


Figure 3.7 – Effects of ε on the ε HRR, gas temperature, velocity, and $\varepsilon\dot{\omega}_{CH_4}$ with mass flux rate = 0.28 kg/m².s and $k_s = 1$ W/m.K.

3.3.2.2 Flame structure on the blowoff limit

In this section, the steady state flame structure on the blowoff limit is evaluated as a function of the matrix properties. Figure 3.8 brings the T_g and T_s profiles for different k_s and for different ε . It is observed that a larger k_s moves the flame front to the downstream position. Increasing the k_s increases the heat recirculation, enhancing the preheating of gas upstream of the combustion zone. Higher k_s allows for the flame to find a stable condition for larger mass flux rates. In order to achieve this stable condition, the flame has to move downstream to increase the residence time of the gas in the region where ($T_s > T_g$). Evaluating the porosity effect, the flame front position tends to keep closer to the inlet when the porosity is increased because of reduction of k_{eff} . Moreover, a higher

ε reduces the h_v leading to a reduction of preheating.

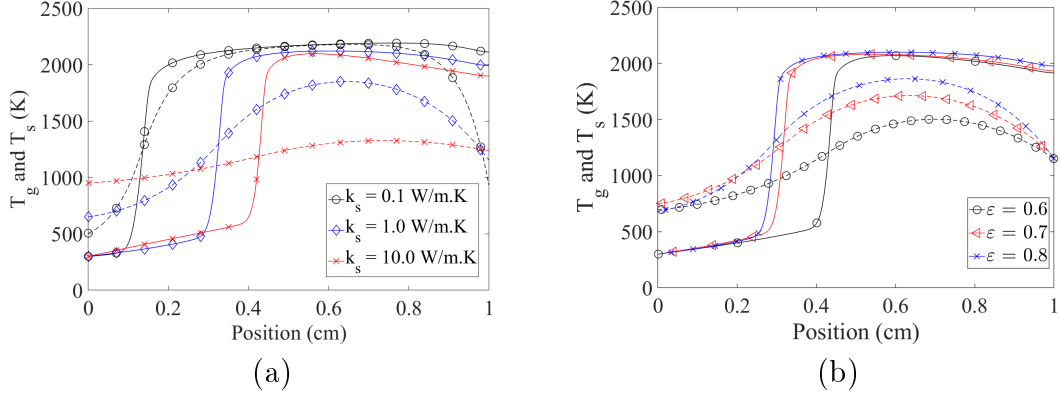


Figure 3.8 – Effects of porosity ($k_s = 1$ W/m.K) and (b) solid thermal conductivity ($\varepsilon = 0.8$) on the T_g and T_s .

In Figure 3.9 (a) it is evaluated the inlet local velocity (v_{in}) and flame front position x_f at the steady-state on the blowoff limit for different ε and k_s . The increase of k_s increases the maximum limit velocity for all evaluated porosities. It occurs because larger solid conductivities increase the heat recirculation from the post-flame to the pre-flame zone, resulting in an increase of the burning velocity. The ε also influences the stability range at the flame. When the ε is increased, the effective thermal solid conductivity ($k_{eff} = k_s(1 - \varepsilon)$) decreases leading to a reduction of the flame stable limit. The heat recirculation also contributes to the x_f stabilizes downstream of the domain.

The η_{rec} in condition of blowoff limit is presented in Figure 3.9 (b). The increase of k_s leads to the rise of η_{rec} , while the increase ε reduces to η_{rec} . Figure 3.9 (b) also compares the η_{rad} in condition of blowoff limit. When the ε decreases, the \dot{m}''_{CH_4} limit is reduced (although the v_{in} increases due to $v_{in} \propto \dot{m}''/\varepsilon$), and the $T_{s,surf}$ presents a small difference among different porosities. Thus, the increase of porosity reduces the η_{rad} . Another interesting observation is drawn from Figure 3.9 (b) where a maximum radiant efficiency in each ε is observed. Although the \dot{m}'' on the blowoff limit rise when k_s increases reducing the η_{rad} , the radiation emission ($\dot{q}_{rad} = -k_{eff} \frac{\partial T_s}{\partial x} |_{x=L} = \sigma(T_s^4 - T_{env}^4)$) has a sufficient magnitude to maintain the profile trend. It is observed that $\dot{q}_{rad} \rightarrow 0$ when $k_{eff} \rightarrow 0$, and when $k_{eff} \rightarrow \infty$, the T_s average along the domain is reduced. The present study is unknown if we are close to these limits, but it contributes to the profile observed.

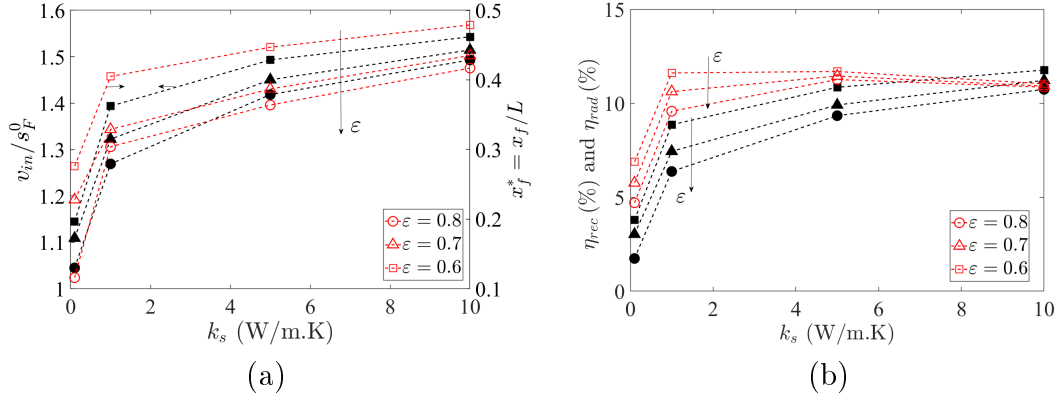


Figure 3.9 – Evaluation of (a) the blowoff limit (voided symbols correspond to v_{in}/s_F^0 and filled symbols correspond to x_f^*) and (b) η_{rec} (filled symbols) and η_{rad} (voided symbols) for ϵ equals to 0.8, 0.7 and 0.6.

3.3.3 Transient response to flow perturbation

In Figure 3.10 it presents the T_g , T_s and CO profiles of a flame initially at the blowoff limit and subject to an abrupt variation of the inlet mass flux rate, as described in Figure 3.3. The present case represent a situation in which the flame remains within the domain during the entire simulation. The flame abruptly moves downstream when the pulse is started ($D = 0.001$ s). The flame displacement velocity (relative to a stationary reference) is reduced when the flame front found a more elevated T_s . The solid at higher temperatures increases the gas preheating region, which increases burning velocity, reducing the flame displacement velocity towards the burner exit. When the pulse is finished, the flame front moves upstream, initially with high displacement velocity. As the flame gets into a colder solid region, the burning velocity is reduced. The flame front slowly moves to its initial position at low displacement velocities due to high thermal inertia of the solid phase (3.10 (c) and (d)). In Figure 3.10 (e) and (f), it is presented the dynamic CO behavior and its equilibrium value. As the consumption velocity increases the peak of CO also increases because more fuel is being consumed. The small dimension of the domain and the progressive displacement of the flame in the outlet direction reduces the consumption of CO within the porous media.

The flame takes a very long time to return to its initial position. Although it is a smaller perturbation more favorable condition (lower amplitude) and a longer time, the

gas and solid profile do not return to the initial position during the time imposed. The flame takes a very long time to return to its initial position. This occurs because the thermal inertia of the solid phase has a characteristic time ($\Delta t \sim \rho_s C_s L^2 / k_s$) between $4 \lesssim \Delta t \lesssim 4 \times 10^2$ s depending on the solid thermal conductivity . For example, a test case was evaluated considering $F^* = 0.5$, $k_s = 1$ W/m.K and $T = 0.5$ s, takes more than 10 s for the gas and solid phases to return to their initial profiles (figure was omitted).

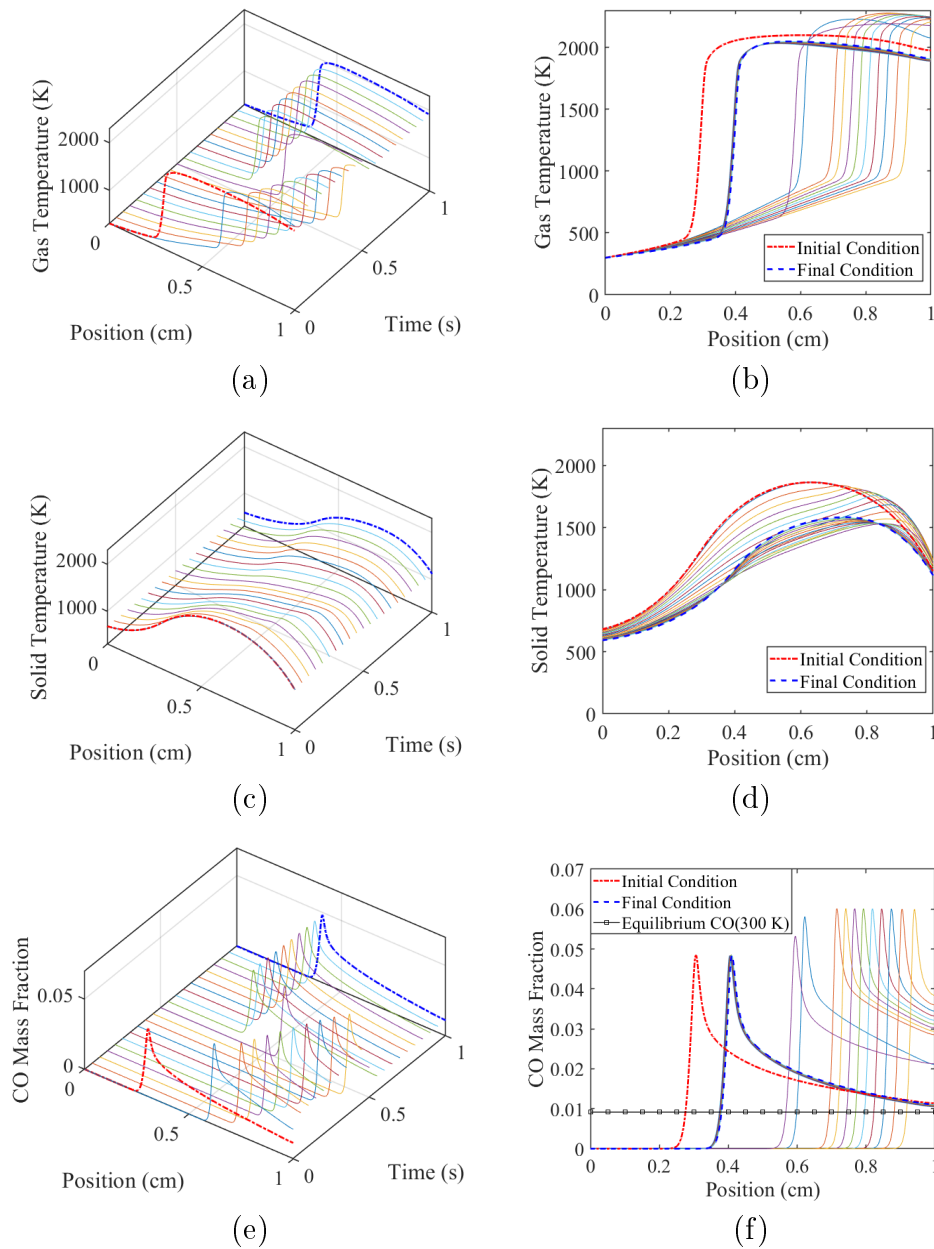


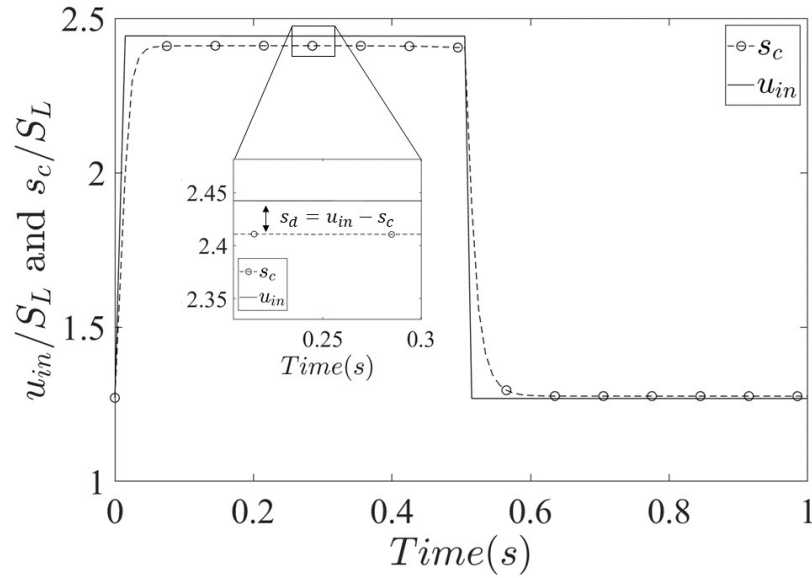
Figure 3.10 – Transient behavior of gas temperature (a and b) solid temperature (c and d) and CO mass fraction (d and e), respectively. The case presented is $\varepsilon = 0.8$, $k_s = 1$ W/m.K, $F^* = 0.925$ and $T = 0.5$ s. On the left, perspective view of variable as function of position and time. On the right, the projection of the time sequential on the variable position plane.

To evaluate the flame behavior during the pulse, it is calculated the consumption speed (s_c [m/s]) that measures the speed at which the flame burns the reactants. For lean

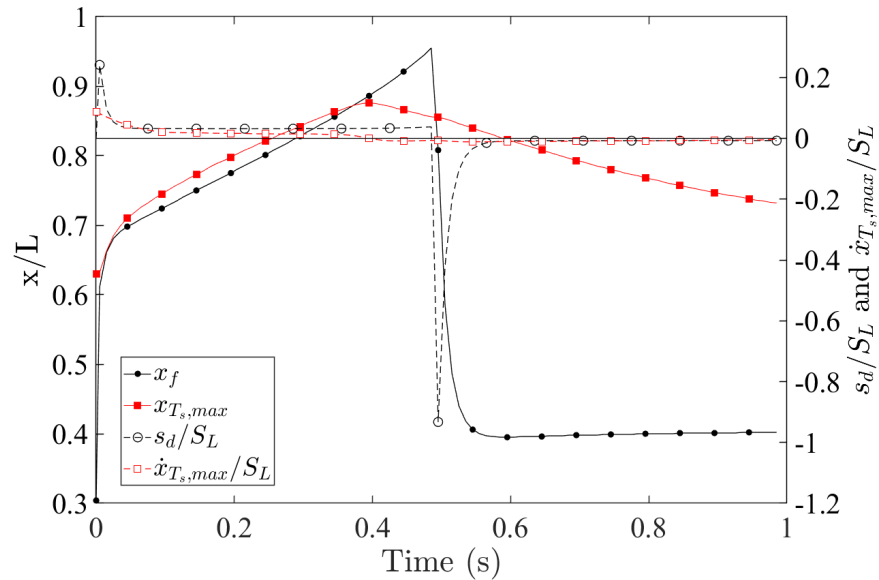
to stoichiometric mixtures it is defined by

$$s_c = -\frac{1}{\rho_u Y_{f,u}} \int_0^L \dot{\omega}_{CH_4} dx \quad (3.9)$$

where ρ_u [kg/m^3] is the inlet density, $Y_{f,u}$ is the fuel unburnt mass fraction, and $\dot{\omega}_{CH_4}$ [$kg/m^3.s$] is the methane consumption rate. The displacement velocity is calculated by $s_d = u_{in} - s_c$. Figure 3.11 (a) presents s_c behavior during a pulse. It observed that during the pulse, the $u_{in} > s_c$. It results in flame front propagating downstream. After the pulse period, the $u_{in} < s_c$ means the flame front is moving upstream. Figure 3.11 (b) presents the s_d . After the pulse starts, the s_d is positive and increases abruptly. Then, it reduces to a plateau that remains practically constant during the pulse period. After the pulse finishes, the s_d is negative, passing through an intense peak and again stabilizing at a low value that remains practically constant during the remaining time. It is expected $s_d = 0$ when the solid temperature also stabilizes. In Figure 3.10 (c) and (d) the solid temperature profile is presented. It is noted that the profile response is slower when compared with the gas temperature profile. In an attempt to track the solid temperature displacement, in Figure 3.11 (b) is depicted the position of the maximum solid temperature ($x_{T_s,max}$) and its time derivative ($\dot{x}_{T_s,max} = dx_{T_s,max}/dt$). The high thermal inertia of the solid phase is revealed by the smooth curve of $x_{T_s,max}$ during the time evaluated. Note that a much longer time would be required to allow the solid-phase to return its initial condition. The displacement velocity of the maximum solid temperature ($\dot{x}_{T_s,max}$) presents lower values compared to s_d .



(a)

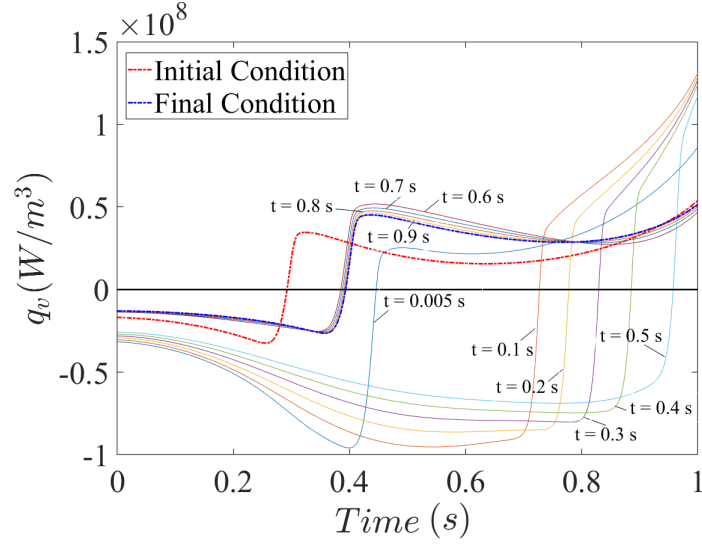


(b)

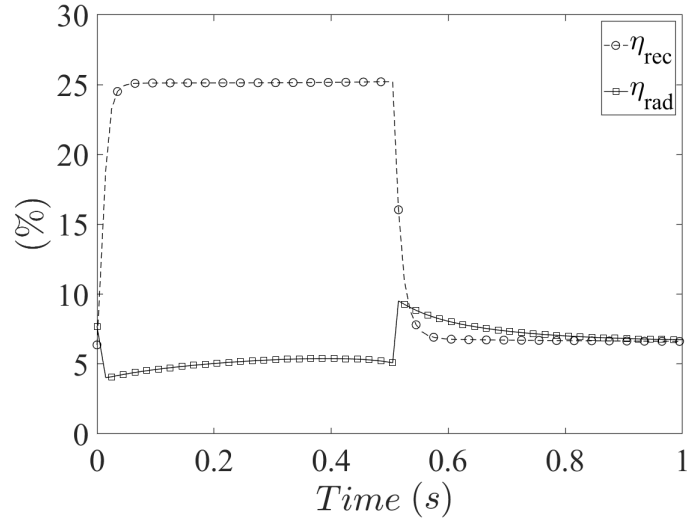
Figure 3.11 – Evaluation of (a) s_c and u_{in} . (b) x_f and maximum solid temperature position ($x_{T_s,max}$), displacement velocity (s_d), $x_{T_s,max}$ and ($\dot{x}_{T_s,max}$) for $\varepsilon = 0.8$, $k_s = 1$ W/m.K, $F^* = 0.925$ and $T = 0.5$ s.

Figure 3.12 (a) presents the convective heat exchange between gas and solid phase (q_v). It is observed an immediate change of profile when the pulse is initiated. The preheating gas region increases, and it progressively covers a larger portion the burner. When the pulse ends, the preheating zone is abruptly reduced. Figure 3.12 (b) presents the η_{rec} and η_{rad} . The behavior of η_{rec} follows from the q_v curves. As the flame moves to

regions of high solid temperature the heat recirculation efficiency increases approximately 5 times, which on its turn increases the flame temperature and consumption velocity. This mechanism renders the flame more resistant to blowoff due to fluctuation of the incoming flow of reactants, when compared to burner stabilized flames. When the pulse ends, η_{rec} returns to its initial value. The η_{rad} initially decreases due to the abrupt increase of mass flux rate ($\eta_{rad} \propto \dot{m}''^{-1}$) and to the high thermal inertia of the solid phase, which keeps the T_s outlet temperature basically constant. During the pulse, the smooth increase of η_{rad} follows the approximation of flame front to the outlet surface, which increases the solid phase temperature in that region. The η_{rad} also tends to the initial value when the pulse is extinguish. The combined effect of η_{rad} decrease and η_{rec} increase during the pulse corroborates to avoid the flame front follow to the outlet after the pulse to be extinguished. Although not presented here, all flames that remained in the domain during the pulse period, returned to their original position after the pulse was finalized.



(a)



(b)

Figure 3.12 – (a) Convective heat exchange between gas and solid phase and, (b) gas-to-solid convection efficiency and radiation efficiency ($\varepsilon = 0.8$, $k_s = 1$ W/m.K, $F^* = 0.925$ and $T = 0.5$ s).

Figure 3.13 presents s_d considering different F^* . The region R1 shows that the increase of F^* results in a higher peak of s_d . In the same way, when the pulse is extinguished (R3), a higher F^* also implies in a higher negative peak of s_d . The s_d in the R2 and R4 follows constant behavior. In R2, s_d always reach a constant value that increases with F^* . In R4 all cases reach the same velocity since upstream condition is similar.

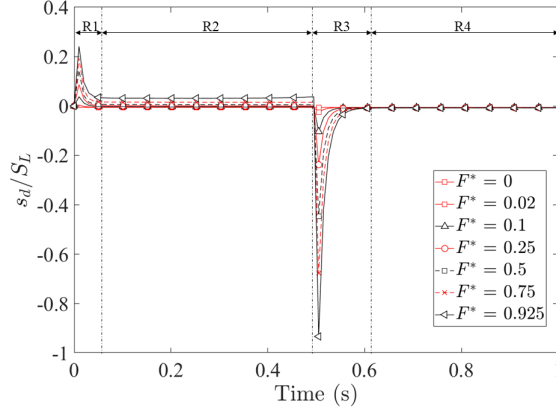


Figure 3.13 – (a) Displacement velocity (s_d) evaluation along the time for different multiplicative factor (F^*) for the $\varepsilon = 0.8$ and $k_s = 1$ W/m.K.

Figure 3.14 compares s_d in R2 and R4 for different k_s and ε . As the behavior of R2 and R4 is practically constant for each F^* tested, one time position have been chosen on the region R2 (0.25 s) and R4 (0.75 s). In the R2, a non-linear behavior is observed. In R4, the pulse period is finished and the T_s and T_g already present a profile close to the initial position. Thus, the flame asymptotically converges to its initial condition justifying the linear behavior.

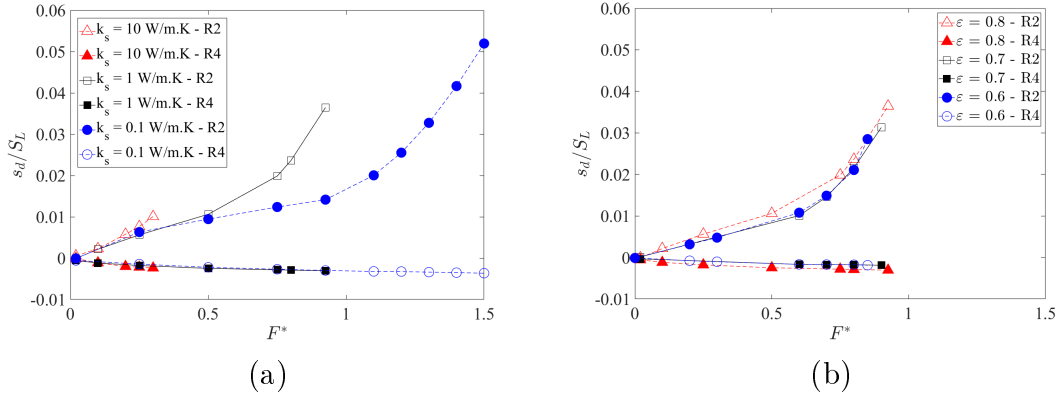


Figure 3.14 – Comparison of s_d during on the time equals 0.25 s (R2) and 0.75 s (R4) for different (a) k_s ($\varepsilon = 0.8$) and (b) for different ε ($k_s = 1$ W/m.K).

The blowoff maps as a function of period, k_s , and ε are depicted in Figure 3.15. A characteristic residence time is estimated by $t_{res} = L/v_{in,bl}$, where $v_{in,bl}$ is the inlet velocity at the blowoff limit, and a non-dimensional pulse period is defined as $T^* = T/t_{res}$. It is observed that larger values of k_s significantly reduce the stable range of operation. It

occurs because the flame stabilizes downstream when k_s increase. On the other hand, the stable range is almost insensitive to variations of porosity due to the close position of the blowoff limit.

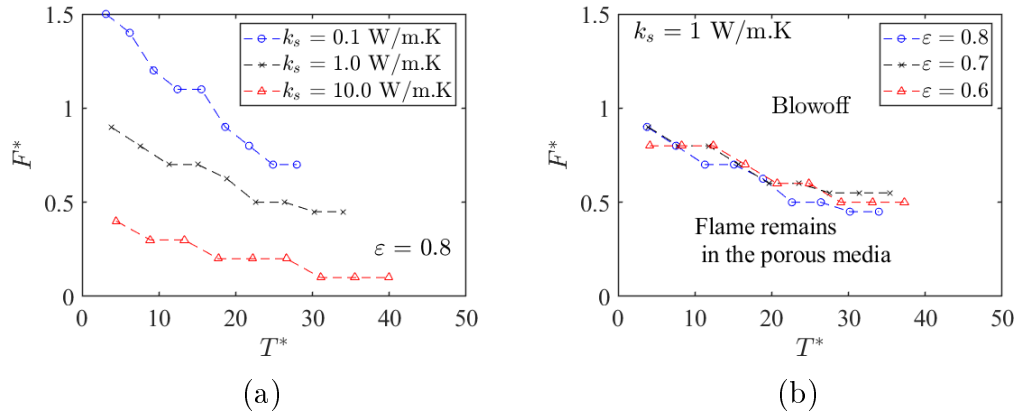


Figure 3.15 – Evaluation of the blowoff limit for different (a) k_s ($\varepsilon = 0.8$) and (b) for different ε ($k_s = 1$ W/m.K).

3.4 Conclusions

In this study, a one-dimensional model of a PMC was employed, assuming detailed chemistry and non-equilibrium heat exchange between the solid and gas phase. The chemistry was implemented with the FGM technique and presented good quantitative results compared to direct integration in steady-state and transient tests.

The study evaluated stable flames that precede the blowoff limit of the burner imposing different porosities and solid thermal conductivities. These results were considered as the initial condition to evaluate the behavior of the solid and gas phase when a pulse of mass flow is imposed at the inlet. The results show a different response time for each phase and a complex behavior that was evaluated in detail. A characteristic displacement velocity of the flame front, which determines the time for blowoff, is identified and explored as a function of the burner parameters.

A stability map showed the influence of the pulse under different ε , k_s , and pulse periods. It was observed that larger values of k_s significantly reduce the stable range of operation while ε is almost insensitive.

Future studies can be explored considering more complex geometry and increasing the time and length scale of the present configuration. Variations on the pulse as pe-

riod and inlet mass flux profile can be analyzed to improve the understanding of flame oscillations.

4 NUMERICAL STUDY OF FLAME STABILITY WITHIN INERT POROUS MEDIA WITH GRADED GEOMETRICAL PROPERTIES

4.1 Introduction

Porous media burner has been an attractive alternative in industrial applications due to the lower pollutants emission, large turndown ratio, high radiant efficiency, and good flame stability. Many applications have been developed as micro combustors [Giovannoni et al., 2016], gas turbine [Djordjevic et al., 2012], domestic cooking stoves [Pantangi et al., 2011; Kaushik et al., 2020], and many others [Banerjee and Paul, 2021]. The porous matrix allows the recirculation of heat from the post-flame products to the incoming reactants through conduction and solid-to-solid radiation leading to an excess of enthalpy at the reaction region [Takeno and Sato, 1979; Sathe et al., 1990; Hsu et al., 1993]. As a result, the flames reach higher temperatures and higher burning velocities. The heat transfer between gas and solid phases creates an additional degree of freedom for the flame to find a stable condition, increasing the burner turn down ratio. The hot solid phase brings a thermal inertia to the burner that makes it less sensitive to oscillations in the reactants supply. Higher flame temperatures promote the conversion of reactants into saturated products of combustion and the flame thickness tends to be smaller than free flames at the same equivalence ratio.

Barra et al. [2003] studied a configuration using a combination of two sections of porous media in a one-dimensional domain. They evaluated some effects of material properties (solid conductivity, volumetric heat transfer coefficient, and radiative extinction coefficient) on the flame stabilization. The results showed that the properties evaluated affect the stable operating range of the burner. In order to maximize the flame stability in the two-section burner, they concluded that the downstream section should have a high conductivity, an intermediate radiative extinction coefficient, and a high volumetric transfer coefficient. On the other hand, the first porous layer should have a high radiative extinction coefficient, a low volumetric heat transfer coefficient and a low conductivity. Liu et al. [2010] evaluated the same configuration explored by Barra et al. [2003] considering a two-dimensional domain but imposing one-step chemistry. They explored the influence of the equivalence ratio, the extinction coefficient, and the thermal conductivity of the solid matrix. They concluded the solid and gas temperature profile are affected by the

thermal conductivity and extinction coefficient of the solid phase. Horsman and Daun [2011] also evaluated an identical porous burner proposed by Barra et al. [2003] using a optimization technique. This technique was applied to find porosity and pore diameter that maximizes the radiant efficiency of the burner. The better combination of porosity (0.95) and pore diameter (1.21 mm) achieved an improvement of around 30 %.

Other studies have explored alternative geometric configurations. For example, Catapan et al. [2011] evaluated the flame stabilization in axisymmetric porous media burner using a single large injector. They observed three possible flame stabilization mechanisms: (1) the first one is the thermal stabilization mechanism imposed by the presence of a solid matrix. It provides an internal heat recirculation and a heat loss to the environment. A second mechanism is present when two layers of different pore size distributions were used together, a flat flame stabilized close to this interface. The flat flame position is influenced by inlet flow velocity, equivalence ratio, pore size distribution and upstream and downstream porous media material. The third mechanism was due to the inlet velocity profile at the injection region, which resulted in a conical flames anchored at the rim of the injection. This third mechanism is responsible for a significant increase in the stability range. Bakry et al. [2011] experimentally evaluated a conical PM burner under high pressure and temperature. The increase of the burner cross-section area in the downstream direction reduces the flow velocity, creating a fluidynamic stabilization mechanism that adds to the thermal mechanism of porous media combustion. When the flame is pushed downstream by the flow, it reaches a region of low flow velocity and it is able to reach a new equilibrium position. The results presented the flame temperature and NO_x emission increased with increasing pressure. Hashemi and Hashemi [2017] studied the same geometry numerically in a two-dimensional model using a one-step chemical mechanism. By performing a parametric study, it was proved that the alteration of divergence angle can change the flame stability limit. The highest limit of flame stability was obtained with a divergence angle equal to 60° . Voss et al. [2013] also evaluates a conical configuration imposing a lean premixed combustion of H_2/CO . A good agreement was verified between experimental tests and numerical results obtained from a quasi-1D model. Furthermore, it was evaluated the flame structure in different operating conditions. They shows that gas-phase thermal flame thickness is one order of magnitude lower than the solid-phase thermal flame thickness. Gao et al. [2017] experimentally evaluated a

PM burner with alumina pellets in the preheating zone and silicon carbide foams with different in the combustion region. The gap was evaluated in different locations and lengths to map the flame stability, flame temperature, and pollutants. The gap lengths and positions affect the heat recirculation and heat losses of the porous burner. The results showed that the temperature profile is similar for different gap lengths, and the flame location moves to the burner exit with the increase of gap length. However, the authors noticed that the flame temperature decreases with the increase of gap length or with the decrease the foam region after the gap. The maximum stable flame range was reached using the gap length of 15 mm and located between the silicon carbide foams and packed alumina pellets. Ghorashi et al. [2020] evaluate experimentally the flame characteristics of a premixed natural gas/air mixture in a porous-free flame burner where a hole is created at the center of the porous foam, and it is also compared to a conventional porous burner. In this non-conventional formulation, the burner extends the rich limit of the flame. Vandadi et al. [2017] studied a two-layered porous burner with an external preheater and a radiation corridor imposing lean propane/air mixtures. The results showed a record radiation efficiency of 37%.

Ellzey et al. [2019] in their review suggests that new methods would create possibilities for both manufacture and research of reactors. Sobhani et al. [2018] evaluated experimentally and numerically a porous burner, having a spatially graded porous matrix. Results from the 1D volume-averaged simulations model presented an important improvement in flame stability between step and graded topology matrix. The graded matrix was tested experimentally, and the results qualitatively confirmed an enhancement of the flame stability compared to the traditional design. Recently, the same group explored the feasibility of three tailored PMBs experimentally [Sobhani et al., 2020]. The results has shown that the model with graded pore diameter and fixed porosity presents wide stable range when compared with a traditional design.

The present study evaluates the differences between two forms of creating the a similar hydrodynamic stabilization mechanism. One of them is by using a porous burner with graded porosity that progressively increases the void area for the gas flow. The other is a porous burner of constant porosity, but with a conical shape with the same increasing void area for the gas flow. The study considers a two-dimensional axisymmetric domain and the FGM reduction technique is implemented to include a detailed kinetic mechanism.

The stable range of the burners are compared and details of the two-dimensional fields are explored.

4.1.1 Problem Definition

The present study evaluates three geometries of the porous media combustor (PMC) schematically represented in Figure 4.1. All domains are axisymmetric and divided into two sections. In the upstream porous layer the solid properties and the geometric parameters are equal for the three domain investigated. The solid thermal conductivity ($k_s = 0.2 \text{ W/m.K}$), porosity ($\varepsilon = 0.835$) and pore diameter ($d_p = 0.29 \text{ mm}$) are equal to the upstream section of the burner studied by Barra et al. [2003].

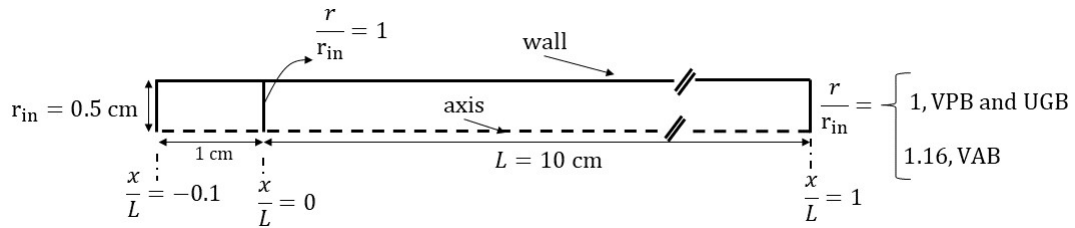


Figure 4.1 – Scheme of the numerical domains.

The downstream region porous layer is the region where the flame is stabilized. The present study evaluated three configurations in this region as shown in Figure 4.2: variable porosity burner (VPB), variable area burner (VAB), and uniform geometry burner (UGB). The last is a cylindrical burner with constant porosity and constant cross-section area. The VAB is proposed with a variable cross section area along the burner (divergent porous burner) and with uniform porosity along the burner. The VPB presents a cylindrical form and variable porosity and pore diameter along the burner. In the two cases with variable geometry (VAB and VPB), an additional mechanism for flame stabilization is introduced. The cross-section area of the burner is progressively increased, which tends to reduce the gas velocity and enhances the ability of the burner to stabilize larger flow rates. In both variable geometry, the effective area for the gas flow rate present the same variation along the burner ($\varepsilon_{VPB}A_{VPB} = A_{VAB}\varepsilon_{VAB}$ where A stands for the cross-section of the burner). The second porous layer's length (L) is equals to 10 cm and k_s is equals to 0.1 W/m.K. The d_p is estimated following Lacroix et al. [2007].

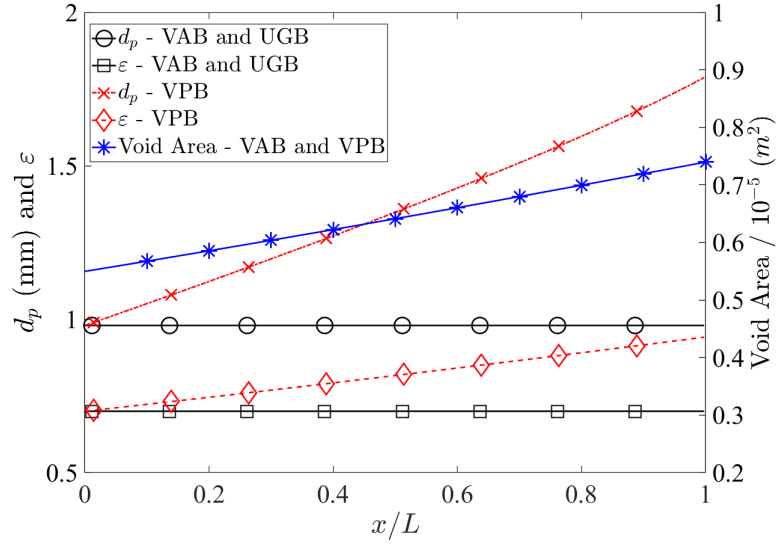


Figure 4.2 – Pore diameter, porosity and void area.

4.1.2 Mathematical formulation

To solve the proposed problem a steady state two-equation (non-equilibrium) model is adopted with, the following assumptions:

1. Gas-solid radiative heat transfer is neglected;
2. Inlet and outlet solid surfaces radiate as a continuous surface with an effective emissivity;
3. Solid thermal conductivity does not vary with temperature;
4. Catalytic effects are neglected;
5. Body forces, Soret and Dufour effects are neglected;
6. Unity Lewis number is valid for all species.

The continuity equation is given by

$$\nabla \cdot (\epsilon \rho_g \vec{u}) = 0, \quad (4.1)$$

where \vec{u} [m/s] pore level velocity of the gas flow. Gas density (ρ_g [kg/m³]) has been obtained from ideal gas equation $\rho_g = PMW_{mix}/R_u T_g$, in which P [Pa] is the pressure assumed to be constant and equal to 1 atm due to the high porosity of the solid matrix.

MW_{mix} [kg/mol] is the average molar mass, T_g [K] and R_u [J/mol.K] are gas temperature and gas constant, respectively.

The momentum equation is given by

$$\vec{\nabla} \cdot (\varepsilon \rho_g \vec{u} \cdot \vec{u}) = -\nabla(\varepsilon P) + \vec{\nabla} \cdot (\varepsilon \tau) + \varepsilon \vec{S}, \quad (4.2)$$

where τ [N/m²] is the viscosity stress tensor, and the pressure drop is evaluated using the Darcy-Forchheimer with \vec{S} [N/m³] given by

$$\vec{S} = - \left(\frac{\mu}{\alpha} + \frac{C_2 \rho_g}{2} |\vec{u}| \right) \vec{u}, \quad (4.3)$$

where $\alpha = d_p^2 \varepsilon^3 / (150(1 - \varepsilon)^2)$ is the matrix permeability and $C_2 = 3.5 d_p (1 - \varepsilon) / \varepsilon^3$ is the non-Darcian drag coefficient [Ergun, 1952].

For the solid phase, the energy transport equation is given by

$$\vec{\nabla} \cdot (k_{eff} \nabla T_s) = h_v (T_g - T_s), \quad (4.4)$$

where h_v [W/m³K] is the volumetric heat transfer coefficient between the solid and the gas. The h_v is calculated by $h_v = k_g Nu / d_p^2$, where the Nusselt number correlation is given by $Nu = C Re^m$ [Younis and Viskanta, 1993]. Data from the reference was curve fitted as shown in Figure 4.3, to take into account the variable pore diameter (Similar approach has been imposed by Horsman and Daun [2011]). The parameter k_{eff} [W/m.K] = $(1 - \varepsilon)k_s + k_r$ is the effective solid thermal conductivity of the porous medium, while the k_r is the radiative conductivity. When the radiation has a short mean free path before attenuation, in comparison with dimensions of the porous media, and the porous media absorbs and scatters isotropically, the radiation can be treated as a diffusion process. Therefore, assuming the optically thick approximation, the radiative conductivity is modeled as $k_r = 16\sigma T_s^3 / 3\kappa$ [Howell et al., 2010], like many other studies [Bouma and De Goey, 1999; Yang et al., 2009; Liu et al., 2015; Li et al., 2016]. The κ is the effective radiative extinction coefficient and it is given by κ [1/m] = $(3/d_p)(1 - \varepsilon)$ [Hsu and Howell, 1992]. The σ is the Stefan–Boltzmann constant with the value of 5.67×10^{-8} [W/(m²K⁴)].

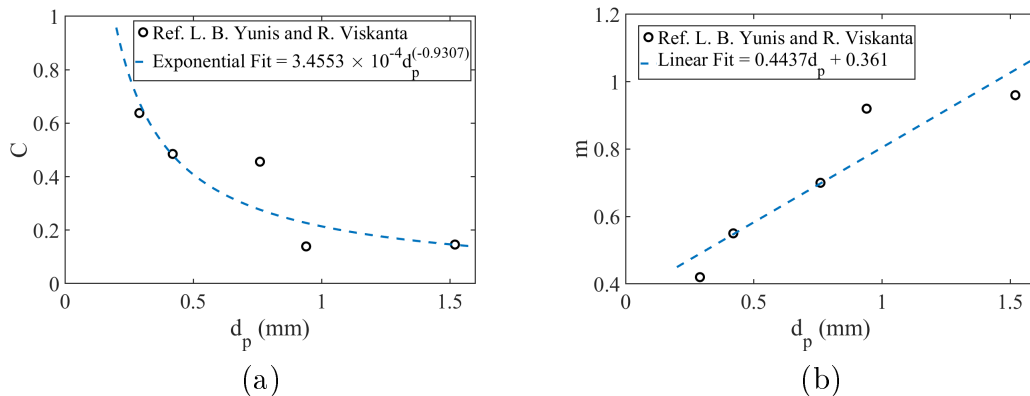


Figure 4.3 – C and m of correlation $Nu = CRe^m$ [Younis and Viskanta, 1993].

Gas phase temperature and composition are described by the Flamelet Generated Manifold (FGM) method [van Oijen et al., 2001]. This method relies on the flamelet assumption to decouple flow and chemistry. Thus, by solving one-dimensional flames with detailed kinetics, the most important aspects of the internal structure of the flame are captured and stored in a table (manifold) as a function of a few independent control variables. During runtime, transport equations for the control variables are solved and their fields are used to reconstruct the flame structure by retrieving the other thermochemical quantities from the manifold. Here lies one of the main strengths of FGM technique, complete combustion phenomena can be represented by solving a few numbers of transport equations. The gas phase energy transport is implemented using the enthalpy (h [J/kg]) formulation due to the ease of handling it as a control variable when the reduced technique FGM is implemented for premixed flame. Thus, the gas energy equation reads

$$\vec{\nabla} \cdot (\varepsilon \rho_g \vec{u} h) + \vec{\nabla} \cdot \left(\varepsilon \frac{k_g}{C_g} \nabla h \right) = h_v (T_s - T_g). \quad (4.5)$$

where C_g [J/kg.K] is the gas specific heat.

Although, the FGM can be very advantageous to describe porous burners with detailed chemistry and reduced computational time, this modelling option is scarcely found in literature [van Oijen et al., 2001; Lammers and De Goey, 2004]. In the present study, flamelet solutions are obtained for different levels of gas enthalpy and stored in a database (a manifold) as a function of h and progress variable (\mathcal{Y}). After the manifold construction is obtained, multidimensional simulations are conducted solving only the conservation of total mass, solid temperature, and the transport equations for h and \mathcal{Y} . Thereby, the

solution of the conservation equations of each chemical species is not required as in direct integration simulations. Once the convergence is achieved, the multidimensional structure of the flame is reconstructed from the manifold with the control variables solution.

The conservation equation for the \mathcal{Y} is given by:

$$\vec{\nabla} \cdot (\varepsilon \rho_g \vec{u} \mathcal{Y}) + \vec{\nabla} \cdot \left(\varepsilon \frac{k_g}{C_g} \nabla \mathcal{Y} \right) = \varepsilon \dot{\omega}_{\mathcal{Y}}. \quad (4.6)$$

In present study the definition used for \mathcal{Y} [Donini et al., 2015a] is

$$\mathcal{Y} = -\alpha_{O_2} Y_{O_2} + \alpha_{CH_4} Y_{CH_4} + \alpha_{H_2O} Y_{H_2O} + \alpha_{H_2} Y_{H_2}. \quad (4.7)$$

where the α_i is equals to $10^{-2}/MW_i$. The progress variable source term ($\dot{\omega}_{\mathcal{Y}}$) is defined as a linear combination of the chemical species source term that defines the progress variable: $\dot{\omega}_{\mathcal{Y}} = \sum_i \alpha_i \dot{\omega}_i$. Mixture thermal conductivity (k_g [W/m.K]) and μ [Pa.s] are obtained from simplified polynomial expressions as function of mixture-specific heat and temperature following [Smooke and Giovangigli, 1991a]. The chemistry is solved using the mechanism DRM22 [Kazakov and Frenklach, 1995]. The flamelet libraries was implemented considering the same approach described in section 3.2.1.

The inlet boundary condition is considered at a constant temperature of 300 K for the gas and radiative heat transfer with the environment $T_{sur} = 300$ K for the solid. The inlet velocity profile is considered uniform, and the CH_4 /air equivalence ratio are 0.65 and 1.0. On the walls, the adiabatic heat exchange condition is imposed. At the output surface, the manometric pressure is equal to zero, and radiative heat transfer with the environment ($T_{sur} = 300$ K) is considered. The complete setup about the boundaries conditions are presented in the table 4.1.

Table 4.1 – Boundary conditions imposed for momentum, T_s , \mathcal{Y} and h transport equations.

Boundaries	Inlet	Outlet	Walls
Momentum	v_{in}	$P = 0 \text{ Pa}$	No slip
T_s	$-k_{eff} \frac{\partial T_s}{\partial x} = \sigma(T_s^4 - T_{sur}^4)$	$-k_{eff} \frac{\partial T_s}{\partial x} = \sigma(T_s^4 - T_{sur}^4)$	$\frac{\partial T_s}{\partial r} = 0$
\mathcal{Y}	$\min(\mathcal{Y})$	$\frac{\partial \mathcal{Y}}{\partial x} = 0$	$\frac{\partial \mathcal{Y}}{\partial r} = 0$
h	$h(T_g = 300 \text{ K})$	$\frac{\partial h}{\partial x} = 0$	$\frac{\partial h}{\partial r} = 0$

Numerical Solution

The equation system for multidimensional simulations is solved by the Fluent 16.1 software. The transport equations for \mathcal{Y} , h and T_s , the manifold retrieval subroutine and transport properties were implemented as user defined functions. The SIMPLE algorithm is used to treat the pressure-velocity coupling. A residual error of 10^{-6} is assumed as the convergence criterion (continuity, v_x , v_r , \mathcal{Y} and h) except for the solid energy equation that achieves the convergence when imposed 10^{-8} . The under-relaxation factor necessary to start correctly the FGM method is 0.9 for \mathcal{Y} , h and T_s to avoid divergence. The other parameters used to obtain the solution are standard values of software. The mesh study showed that a cell size lower than $\Delta x = \Delta r = 0.0625$ mm is sufficient to achieve mesh independent results. Details about mesh independence is presented in the Appendix E.

Model Validation

The solid and gas temperature profiles of Liu et al. [2010] and Barra et al. [2003] are used to evaluate the numerical model implemented. The computational domain is 6.05 cm long and consists of two different porous foam layers. The upstream foam layer is 3.5 cm long ($k_s = 0.2$ W/m.K, $d_p = 0.029$ cm, $\varepsilon = 0.835$) and downstream section is 2.55 cm ($k_s = 0.1$ W/m.K, $d_p = 0.152$ cm, $\varepsilon = 0.87$). The inlet velocity considered is 60 cm/s with an equivalence ratio of 0.65. Figure 4.4 shows the three solutions close to the interface between two layers, where the flame is stabilized. Following Barra et al. [2003], the validation study employs a one-dimensional transient version of the model. A flame is considered stable when it remains in a certain position for more than 30 seconds. The differences found among the models are due to the difference among the chemical mechanism, and radiation models. The Liu et al. [2010] applied a one-step mechanism and the Rosseland model to describe the radiation (2D domain). Barra et al. [2003] solved the porous burner using detailed chemistry GRI 1.2 [Frenklach et al., 1995], and the radiation transport is described using the RTE with P-3 approximation (1D domain).

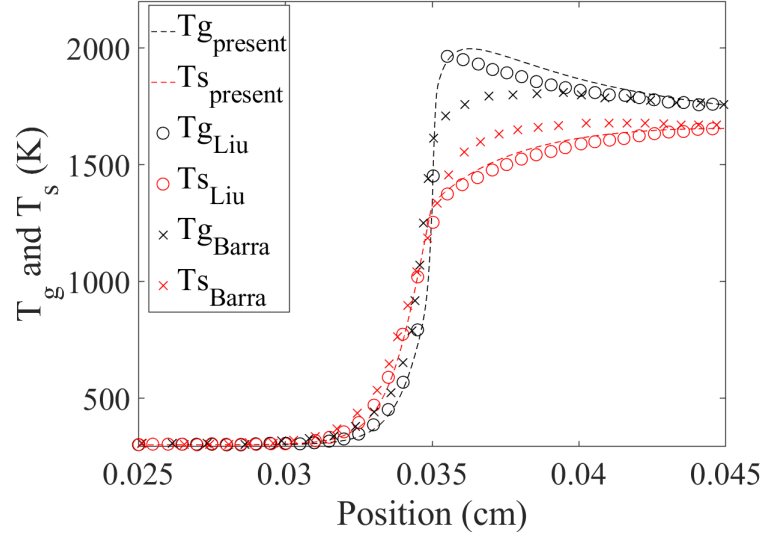
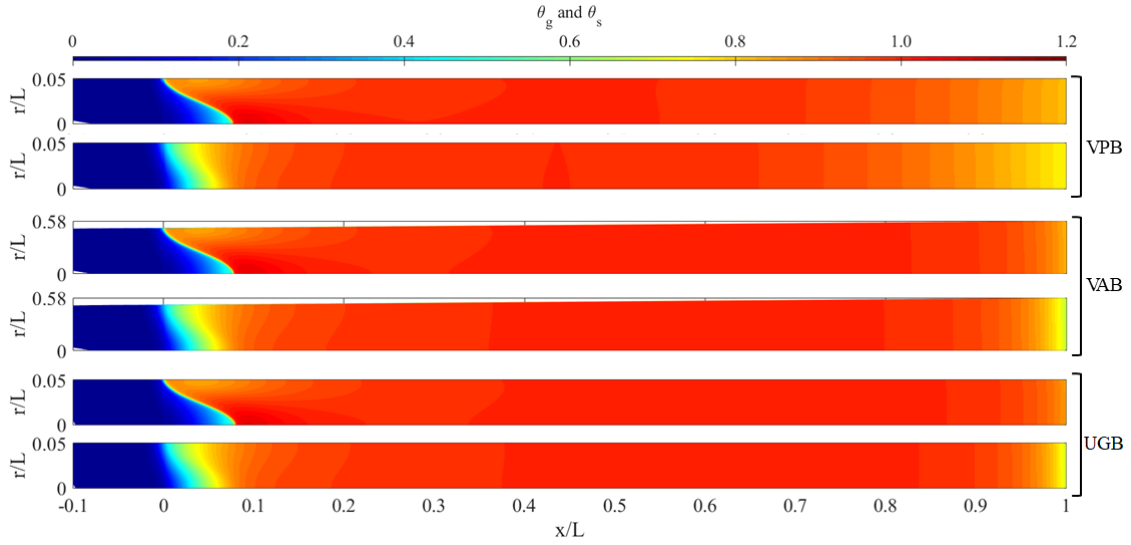


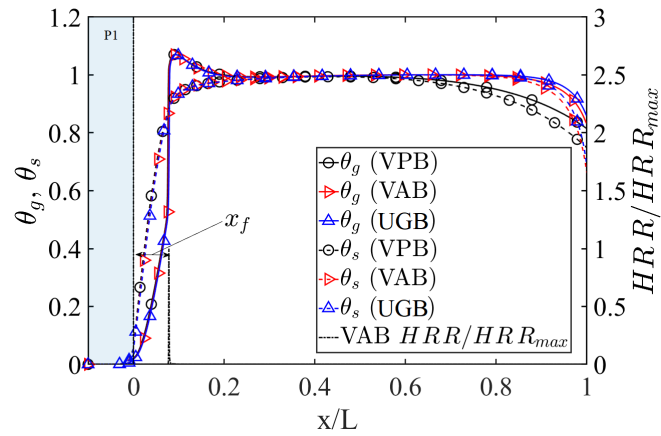
Figure 4.4 – Comparisons of gas temperature and solid temperature between the present study and previous studies (Barra et al. [2003]; Liu et al. [2010]).

4.2 Results and Discussion

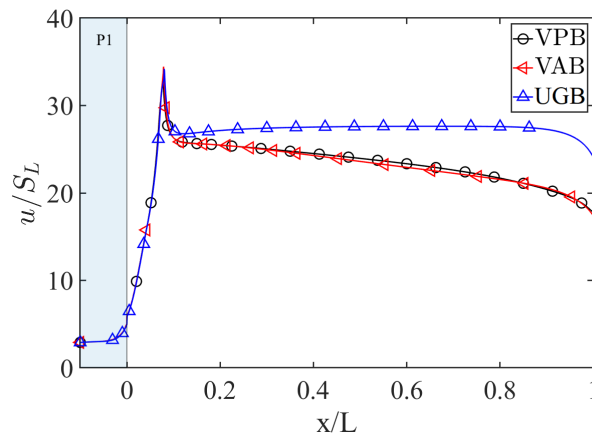
Figure 4.5 (a) presents the solid and gas normalized temperature ($\theta_{phase} = (T_{phase} - T_{g,in}) / (T_{ad,\phi} - T_{g,in})$) contours for VPB, VAB and UGB geometries considering the same inlet conditions. The stabilization occurs in the interface between two porous layers. Although the flame front profile is similar among the configurations, the gas and solid temperature profile present a smooth difference near the flame front and close to the outlet. Figure 4.5 (b) presents the θ_g and θ_s profile on the axis boundary. For these long burners with adiabatic walls, the two phases reach thermal equilibrium at the adiabatic flame temperature in the post-flame region. Only close to the outlet surface, non-equilibrium effects becomes important due to the intense heat loss by radiation. The heat release rate (HRR) normalized by its maximum value is illustrated for the VAB. In the present work, the flame front position (x_f) is defined as the distance of the maximum HRR on the centerline and the interface between the two porous burners ($x = 0$). Evaluating the normalized velocity profile along the centerline in Figure 4.5 (c), a peak of velocity on the flame front is observed due to the increase of gas temperature. Downstream of the flame front, the velocity profiles present a similar magnitude to VPB and VAB due to the same void area and similar temperature. The UGB presented a higher velocity due to minor void area along the domain.



(a)



(b)



(c)

Figure 4.5 – Comparison between VPB, VAB and UGB for $v_{in}/S_L = 2.91$ and $\phi = 1$. (a) Normalized temperature contours for the gas and solid phase. (b) Normalized gas and solid temperature and heat release rate (HRR), and (c) normalized gas velocity on the centerline.

4.2.1 Flame front position and Stability range

Figure 4.6 presents a comparative of the flame front position (x_f) for equivalence ratios 0.65 and 1 for the three burners. In the present study, the flashback is achieved when HRR_{max} crosses the interface between the two porous layers ($x/L = 0$) and the blowoff is defined when the flame leaves the downstream porous layer. For the uniform geometry burner (UGB), the flame front only stabilized on the interface between the two porous layers. The burner with variable porosity (VPB) presented a larger stability range than the burner with a variable area (VAB). In both cases, the flame remained anchored at the interface for small inlet velocities. Increasing the inlet velocity, the flame position presented an abrupt displacement downstream. From that point, on the flame front followed a smooth displacement downstream. The abrupt displacement can be explained by the porous burner proprieties imposed. The first porous layer presents a higher porosity than the second porous layer. Thus, the flow in the downstream region of the interface has lower velocity and, consequently, a wider range of stability when the velocity is increased. Evaluating the average heat transfer coefficient on the first porous layer between the positions -0.1 and 0 (\bar{h}_{v1}) and the second porous layer between the positions 0 and 1 (\bar{h}_{v2}) for the condition imposed in Figure 4.5, it is found that $\bar{h}_{v1}/\bar{h}_{v2}|_{VPB} \approx 2.29$, $\bar{h}_{v1}/\bar{h}_{v2}|_{VAB} \approx 2.47$ and $\bar{h}_{v1}/\bar{h}_{v2}|_{UGB} \approx 2.38$. This higher magnitude of \bar{h}_{v1} when compared with \bar{h}_{v2} favors the gas preheating, and this is why a higher stability range is achieved at the interface. In contrast, this condition is not favorable to avoid flashback, a condition not explored in the present work.

Figure 4.6 (b) presents the power range of each burner. It can be clearly observed that the inferior limit for each burner is almost the same for both equivalence ratio. It occurs because the geometric and physical characteristics are similar near the interface. The lower equivalence ratio (ϕ) presented the higher turn down ratio, defined as $v_{in,max}/v_{in,min}$.

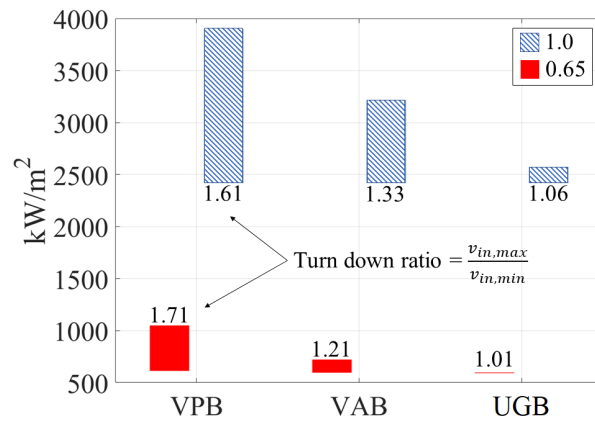
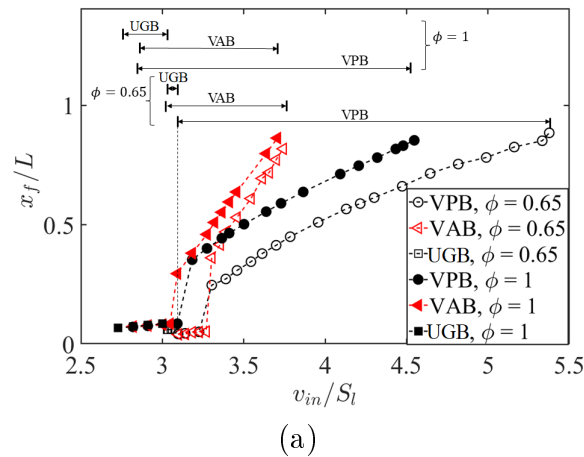


Figure 4.6 – Evaluation of (a) flame front position (x_f) for different inlet velocity, (b) turn down ratio and power range for VPB, VAB and FPV for $\phi = 0.65$ and 1.0.

Heat recirculation through gas-solid heat exchange

The heat recirculation efficiency (η_{rec}) is the fraction of the heat released by the flame that is transferred from the solid to the gas-phase in the preheating region of a porous burner. The η_{rec} is calculated as

$$\eta_{rec} [\%] = 100 \times \left| \frac{\int_{V_{ph}} q_v dV_{ph}}{\dot{m}_{CH_4,in} LHV} \right|. \quad (4.8)$$

where V_{ph} is the preheating region volume, $q_v = h_v(T_g - T_s) [W/m^3]$ is the convective heat transfer. The V_{ph} is bound by the temperature isosurface where the gas temperature has increased by 1 % of its inlet value and the isosurface defined by $\theta_g = \theta_s$. Figure 4.7 (a) shows the two dimensional distribution of q_v close to the flame surface. The preheating is

more intense close to the tip of the flame at reactants side. The preheating of reactants decreases close to the walls due to the small flow velocities in this region, which tends to equilibrate gas and solid temperature (a detailed discussion is presented in the next section). In Figure 4.7 (b) shows the distribution of q_v , θ_g and θ_s along the centerline and the wall.

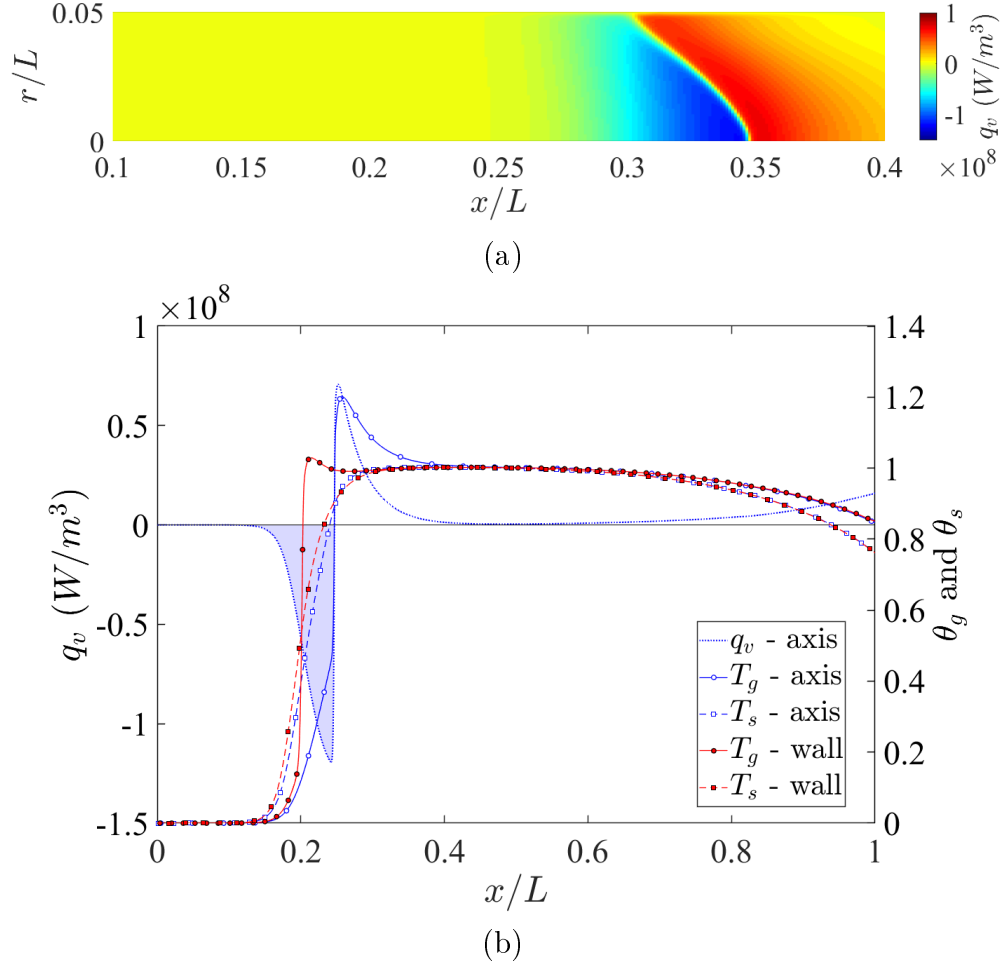


Figure 4.7 – (a) Contour of two dimensional convective heat exchange (q_v). VPB imposing $\phi = 0.65$, and velocity equals to $v_{in}/S_l = 1.20$ (c) q_v , θ_g and θ_s evaluated on the wall and axis.

Figure 4.8 presents the η_{rec} for different equivalence ratios. The qualitative behavior is similar for UGB compared with other studies [Barra et al., 2003; Li et al., 2016], i.e., the efficiency is reduced smoothly when the v_{in} increases. Moreover, greater efficiency is found when a lower equivalence ratio is imposed. For VPB and VAB, the efficiency reduces while the flame is anchored on the interface of two porous layers. When the flame detaches from the interface, the VAB presents an abrupt increase, but increasing the v_{in}

the tendency follows reducing. For VPB, tendency is switched, i.e., as the v_{in} is increased higher is the η_{rec} until outlet conditions effect becomes more relevant.

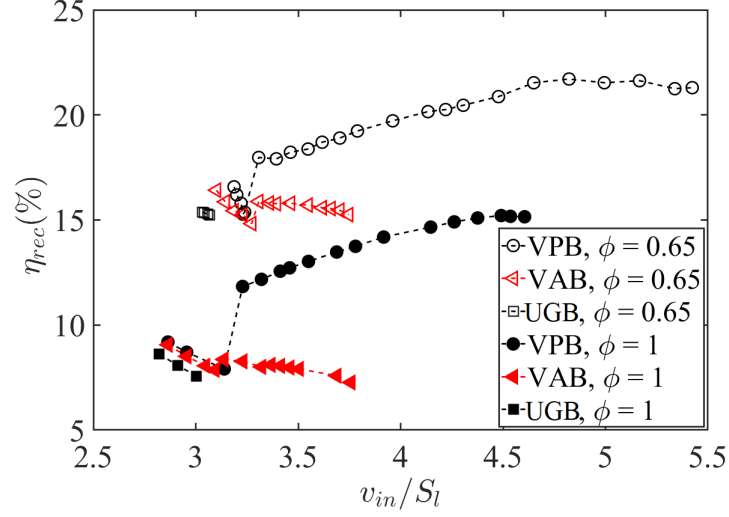
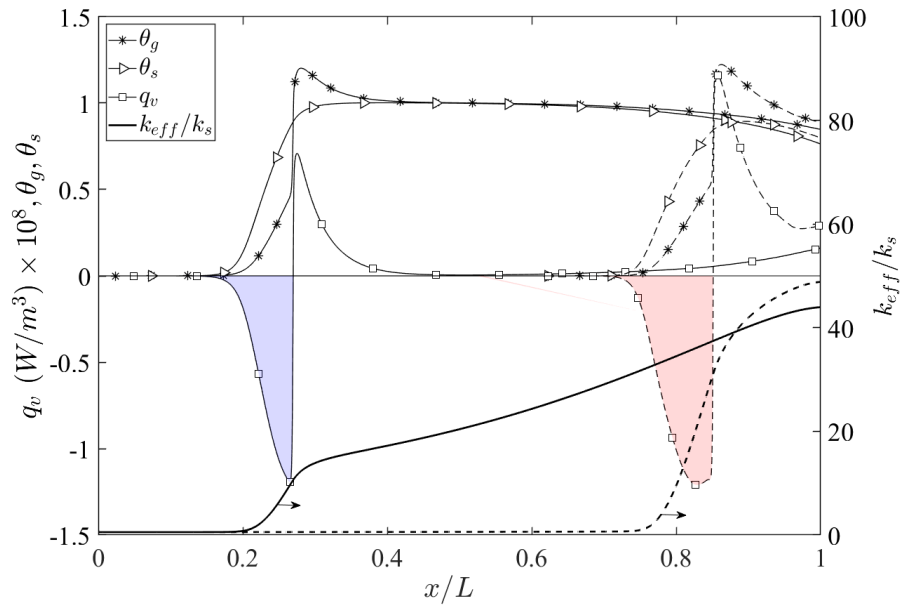
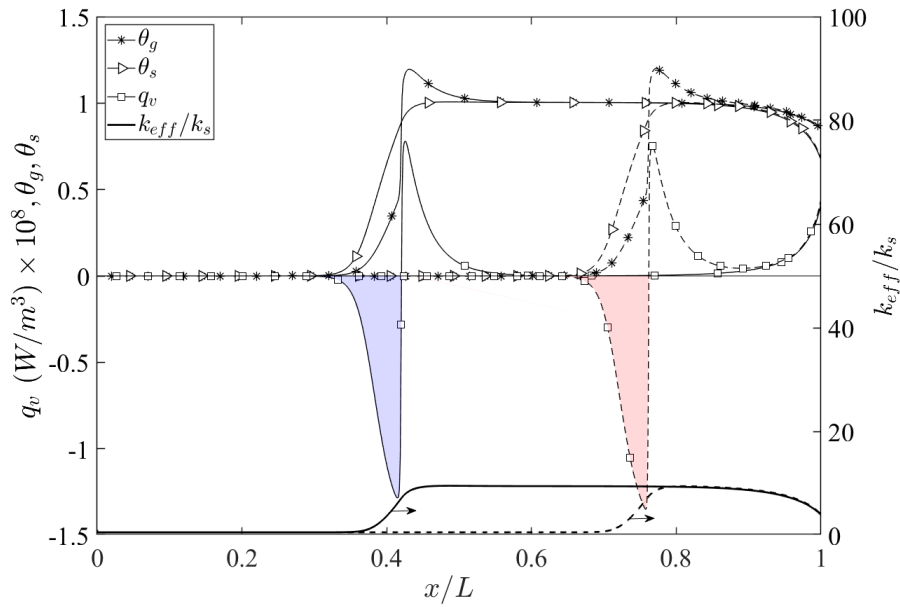


Figure 4.8 – Heat recirculation efficiency as a function of inlet velocity for equivalence ratio equals to 0.65 and 1.0.

Figure 4.9 shows the temperature (θ_g and θ_s), q_v and k_{eff}/k_s profiles on the centerline for different inlet velocities for the cases VPB and VAB. The q_v increases for VPB as the inlet velocity increases (filled region in Figure 4.9 (a)) while VAB, the q_v is very similar in both condition evaluated (Figure 4.9 (b)). Moreover, the effective solid thermal conductivity (k_{eff}) becomes dominant in both case evaluated. For the VPB, the k_{eff} is higher as the flame front stabilizes closer the outlet. A higher k_{eff} favors the gas preheating. In the present study, the k_{eff} is sensitive to pore diameter and porosity ($k_{eff} \propto d_p, (1 - \varepsilon)^{-1}$) due to the Rosseland approximation used to describe the solid-to-solid radiation. The d_p and ε are maintained constant for VAB along the domain, while for VPB the d_p and ε increase as they approach the outlet. For VPB, k_{eff} is higher the further downstream the flame is anchored. Another immediate consequence of preheating is the increase in the burning velocity. It brings the flame front upstream and amplifies the region that precedes the blowoff.



(a) VPB



(b) VAB

Figure 4.9 – Evaluation on the centerline of gas temperature (θ_g), solid temperature (θ_s), convective heat exchange (q_v), and effective solid thermal conductivity normalized (k_{eff}/k_s) for the (a) VPB considering $v_{in}/S_t = 3.35$ (- solid line) and $v_{in}/S_t = 5.33$ (- - dashed line) and (b) VAB considering $v_{in}/S_t = 3.35$ (- solid line) and $v_{in}/S_t = 3.70$ (- - dashed line). The equivalence ratio evaluated is 0.65.

4.2.2 Detailed analysis of the flame front

Figure 4.10 brings a detailed comparison of some two-dimensional fields for the VPB and VAB cases. The normalized interphase heat transfer is shown in the background color while gas flow streamlines, solid temperature iso-lines and solid-phase heat flux lines are overplotted. Figure 4.10 (a) and (c) are for lean conditions ($\phi = 0.65$) while Figure 4.10 (b) and (d) are for stoichiometric conditions. The figures reveal a higher q_v magnitude for the cases with a higher equivalence ratio. For the preheating region, before the flame front, lower values of q_v are found near the tip when compared with the region near the wall for both equivalence ratios. This is due to the higher gas velocity near the centerline which makes necessary a higher preheating to stabilize the flame. The consequence of it is that the flame becomes longer in cases with a higher equivalence ratio. The streamlines present a non-monotonic behavior around the flame front. The global structure of the flame and non-uniform temperature profile favors for the momentum components (m_x and m_r) being changed along the path.

In each panel of Figure 4.10, the heat flux by diffusion in the solid phase flows from the right to the left following the heat flux lines shown in red. At the post-flame region, θ_s contours show that lower solid-phase temperatures are found towards the wall. Thus, moving from the right to left, it is observed that the solid heat flux lines diverge to the wall as they approach the flame front. This occurs due to the high positive source term (q_v) around the flame tip and the consequent increase of θ_s in this region. After the solid heat flux lines cross the flame front, the q_v becomes a sink term for the solid energy equation ($\theta_s > \theta_g$). Hence, the solid heat flux lines are redirected towards the center. Figure 4.10 (c) presents a lean flame front stabilized more downstream of the domain. It is possible to observe that the solid heat flux lines accumulate at a point where the maximum θ_s is located.

Figure 4.10 also shows a different flame profile for each case presented. It is observed that the conditions with higher ϕ presents a higher total flame arc length. The total arc length of the flame front can be found considering that an element dl of the arc length is related to the respective elements at both axis by $dl^2 = dx^2 + dr^2$. Dividing this expression by dx^2 , isolating dl and integrating one finds

$$L_f = \int_{x_i}^{x_t} (1 + (dr/dx)^2)^{1/2} dx. \quad (4.9)$$

The iso-line equals $\theta_g = 0.7$ has been chosen to evaluate the flame front profile. The x_i is the initial position in x where the flame front starts and x_t is the position x of the tip of the flame. Figure 4.11 shows the comparison of L_f along the stable range. The results show that a higher equivalence ratio presents a higher L_f throughout the entire stability range. The VAB presents a higher L_f in almost the entire stable range when compared with VPB (except in the region where the VPB is still stabilized at the interface) imposing the same velocity. Moreover, a non-monotonic behavior of L_f is observed. This abrupt change in the flame shape at a certain velocity happens exactly when the flame leaves the interface and is no more influenced by the first porous region.

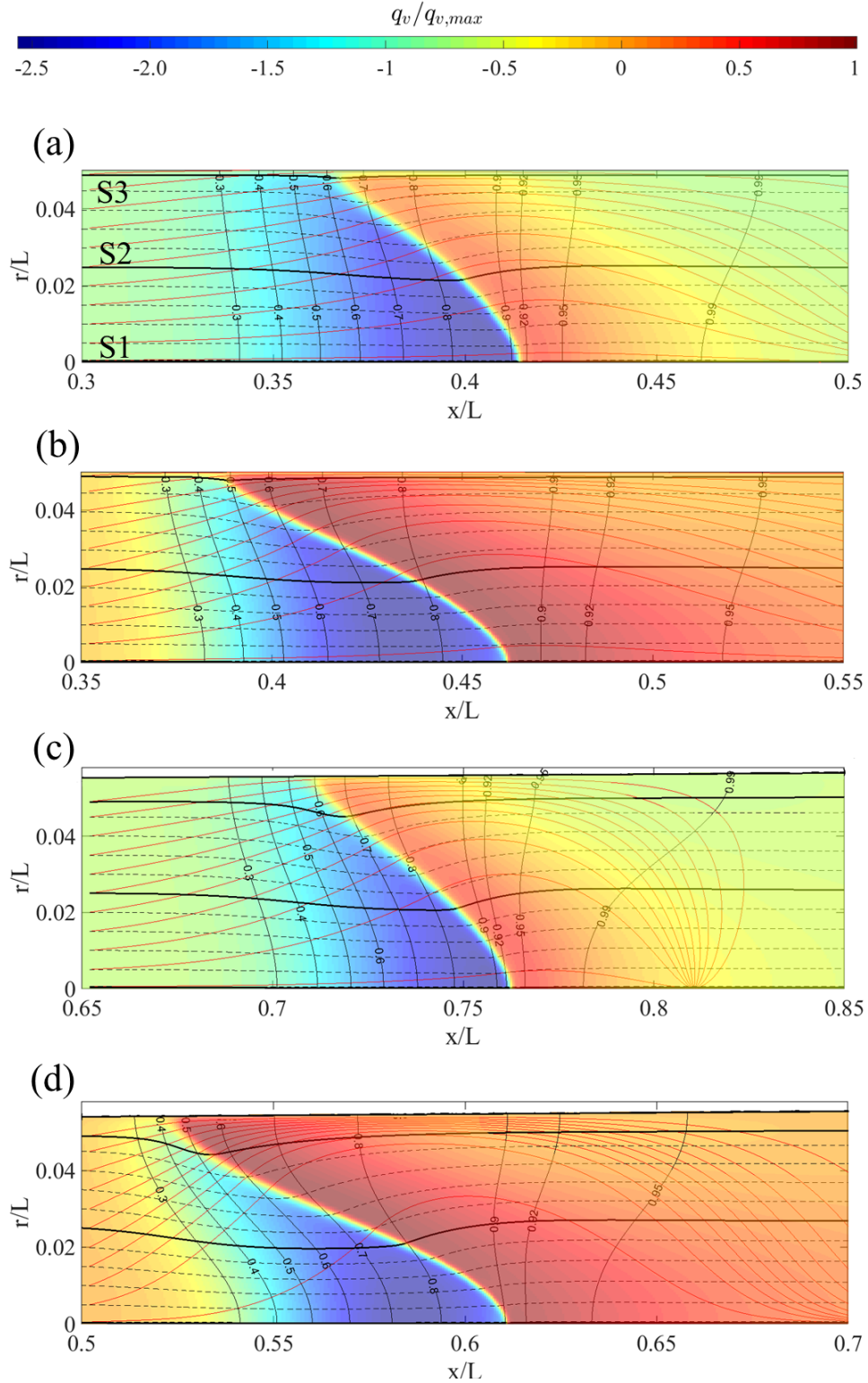


Figure 4.10 – Contour of two dimensional convective heat exchange (q_v), streamlines (black dashed line --), level curve of solid temperature (black solid lines -), solid-phase heat flux lines (red solid lines -). The bold streamlines (S1, S2 and S3) correspond to conditions for which temperature (θ_g and θ_s) and heat release rate (HRR) profiles are presented in Figure 4.12. VPB (a) $\phi = 0.65$ and $v_{in}/S_l = 3.7$ m/s. (b) $\phi = 1$ and $v_{in}/S_l = 3.41$ m/s. VAB (c) $\phi = 0.65$ and $v_{in}/S_l = 3.7$ m/s. (d) $\phi = 1$ and $v_{in}/S_l = 3.41$ m/s ($q_{v,max} = 1.1261 \times 10^8$ W/m³K).

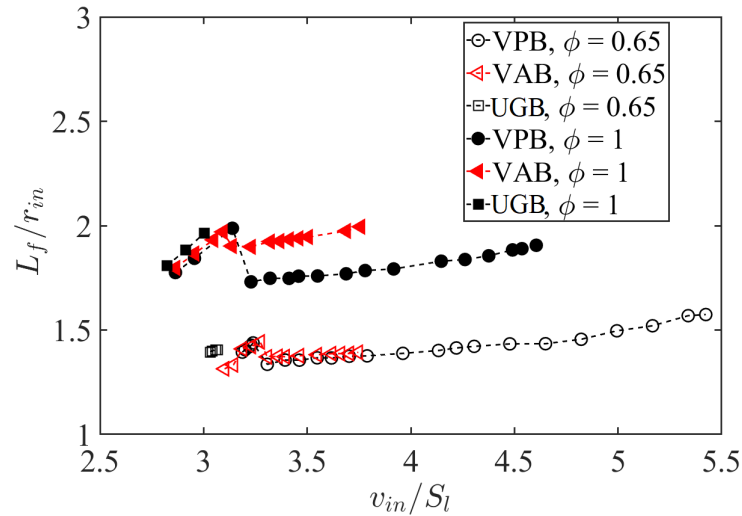


Figure 4.11 – Flame arc length (L_f) as a function of inlet velocity for ϕ equals 0.65 and 1.0.

Figure 4.12 evaluates θ_g , θ_s and HRR profile along the S1, S2, S3 streamlines for each case presented in Figure 4.10. Although the flame shape resembles that of a channel flame, the stabilization of a flame within a porous medium follows a different mechanism. In channel flames, as in Bunsen burners, the flame is anchored by the heat losses to the walls. In a porous medium, the heat transfer between gas and solid phases is present everywhere, even for adiabatic wall, as it is the case for the present study. Thus, at each position on the flame front, the kinematic equilibrium between the flame propagation velocity and the local flow velocity is reached as a result of the heat recirculation experienced by the incoming reactants following a particular streamline. The low flow velocity near the wall is balanced by the low propagation velocity in this region.

Looking at the streamline S1, which follows the centerline of the burner, the behavior of the solid and gas phases follows what is expected from one-dimensional models. The heat recirculation induced by the solid phase results in a gas phase preheating that leads to peak temperatures above the thermodynamic limit based on the incoming reactants ($\theta_g = 1$). This is the case because the streamlines and the solid-phase heat flux lines are coincident at the centerline. For the other streamlines (S2 and S3), when the solid-phase heat flux is not aligned with the flow, some particular features are observed.

Since the streamline S3 is close to the wall, this region is characterized by lower flow velocities (u_g), thus a smaller flame temperatures are necessary for reaching the cor-

respondent consumption velocity ($S_c = u_g$). Close to the flame front, the non-equilibrium between the phases is large and a proportional larger fraction of the heat released by the flame is lost to the solid-phase compared to other streamlines. However, in this region the heat flux lines at the solid phase are not aligned with the flow, instead they point towards the center. This means that part of the heat lost by the gas-phase to the solid-phase at the post-flame region is directed to the center and does not preheat the same streamline. Thus, along with S3, there is a net loss of energy that results in flame temperatures below $\theta_g = 1$ for all cases except for VPB at $\phi = 0.65$. Another interesting characteristic of the streamline S3 is that the peak temperature is not necessarily found at the flame position. For these cases, the peak is found downstream from the flame. This is due to the heat flux at the solid-phase, which tends to concentrate near the wall in the post flame region, as seen in Figure 4.10. For the streamline S3, the low gas velocity results in a thermal equilibrium between the phases in this region at a temperature that is controlled by the solid intraphase heat transfer.

For streamline S2, the non-alignment between streamline and solid-phase heat flux line is even more pronounced. However, for this streamline, the heat released by the flame is larger and a smaller proportion of it is lost to the solid phase. Additionally, this streamline is preheated by the heat flux lines that come from regions close to the walls. Then the flame temperature is determined by a complex combination of heat loss and gain to regions that are not aligned with the flow.

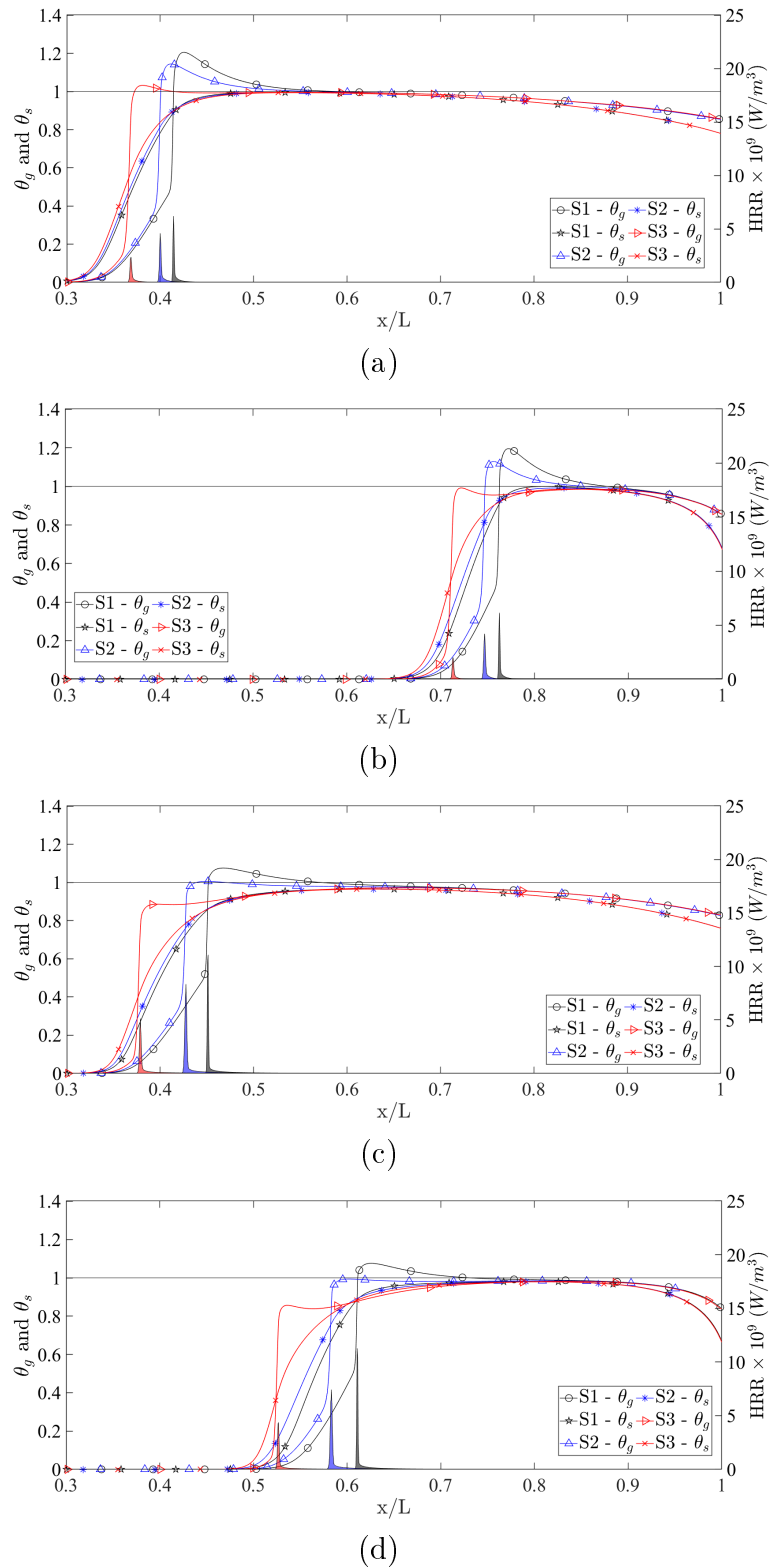


Figure 4.12 – Temperature (θ_g and θ_s) and heat release rate (HRR) from the streamlines S1, S2 and S3 highlighted in Figure 4.10. (a) VPB and (b) VAB with $\phi = 0.65$ and $v_{in}/S_l = 3.7$ m/s. (c) VPB and (d) VAB with $\phi = 1$ and $v_{in}/S_l = 3.41$ m/s.

To capture the mass flux rate locally in different positions of the domain, the axial mass flux rate $m_x = \rho u_x / \rho_{in} S_{L,\phi}$ and the radial mass flux rate $m_r = \rho u_r / \rho_{in} S_{L,\phi}$ have been evaluated. Kim and Maruta [2006] suggests that this approach can be used to distinguish the momentum change from the thermal expansion. Figure 4.13 presents m_x and m_r for the VPB. The m_x increases in the center of the pre-flame region and reduces its magnitude near the wall, showing that the flow converges to the center of the porous medium at the pre-flame region. Intense negative values of m_r are seen close to the flame front and near the wall at the pre-flame region. Intense positive values of m_r are present close to the flame front, at the post flame region, due to the gas expansion normal to the flame front. This intense gas expansion deflects the streamlines towards the walls, which explains why in the pre-flame region the flow tends to converge towards the center.

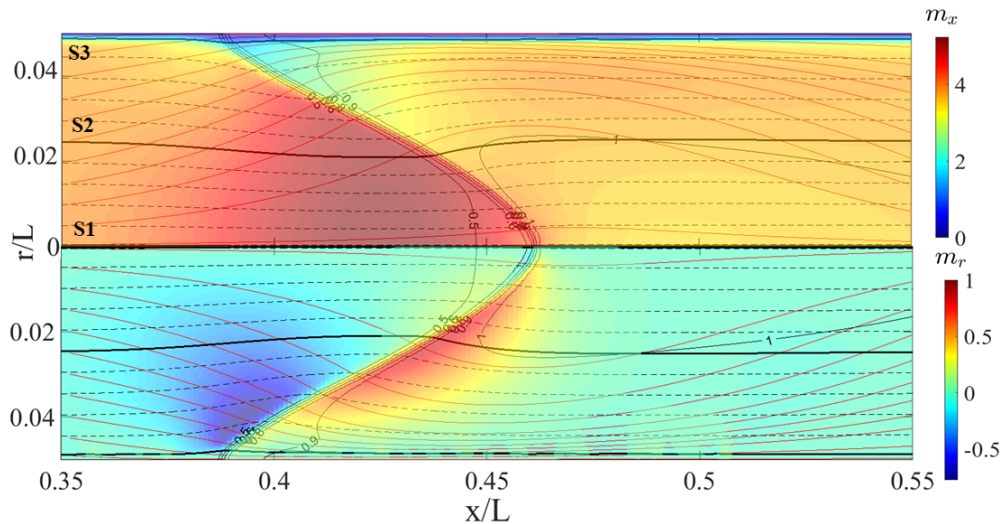


Figure 4.13 – Evaluation of contour normalized mass flow rate in axial (m_x) and radial direction (m_r). Streamlines (black dashed line --), level curve of gas temperature normalized (black solid lines -), flow line of solid heat transfer (red solid lines -). The bold streamlines (S1, S2 and S3) correspond to conditions for which m_x and m_r profiles are presented in Figure 4.14. The present case is VPB considering $\phi = 1$ and $v_{in}/S_L = 3.41$.

Figure 4.14 is observed an abrupt increase of m_x in the flame region of the streamline S1 and S2 for VPB and VAB. The behavior is inverted close to the wall, i.e., the mass flow rate presents an abrupt reduction along S3. It shows that the mass flow rate is directed toward the flame tip. Moreover, it is noted that outside the flame region, the

m_x presents a continuous reduction due to the void area increase. For the same inlet condition, the VPB flame stabilizes upstream, and the difference in the flame position is larger for $\phi = 0.65$. The peaks in m_x are larger for the VAB. This is consistent with Figure 4.10 and 4.11 which show that the flame is longer for VAB case. A longer flame results in larger positive values of m_r due to the expansion normal to the flame front and, as shown in Figure 4.13, this creates a tendency of the flow to converge to the center in the pre-flame region. These results demonstrate that some aspects of the flame can only be captured in multidimensional configuration.

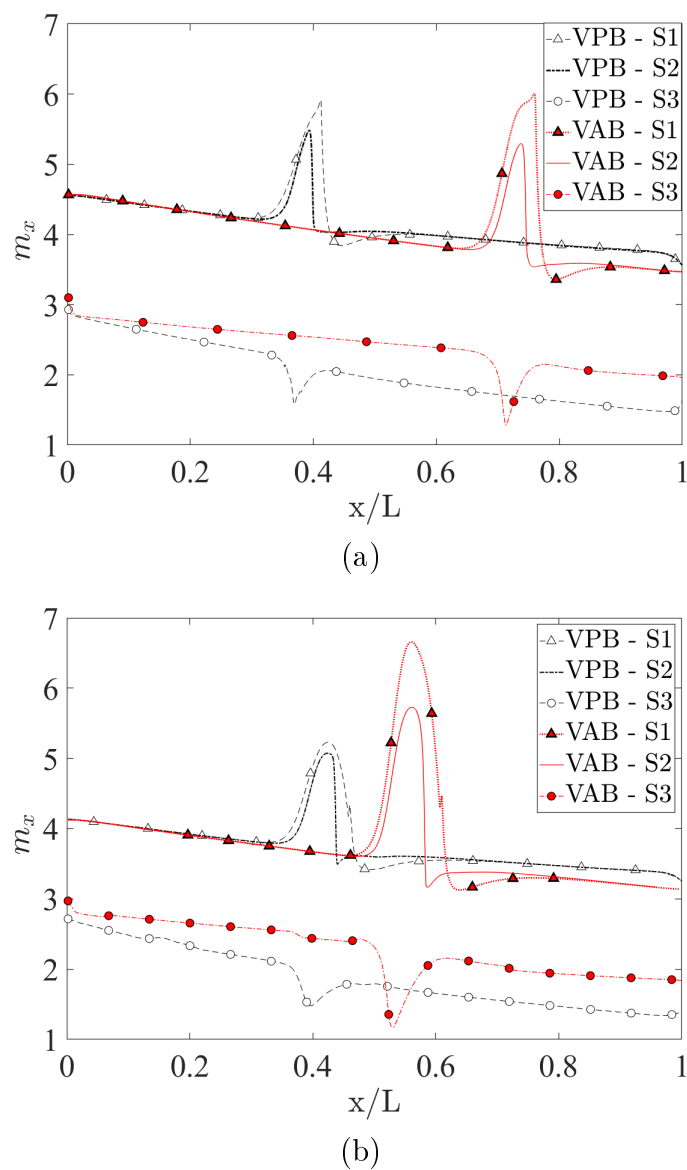


Figure 4.14 – Mass flow rate on the S1, S2 and S3 along the VPB and VAB for (a)

$\phi = 0.65$ and $v_{in}/S_l = 3.41$. (b) $\phi = 1$ and $v_{in}/S_l = 3.7$.

4.3 Conclusions

A Numerical study of flame stability within inert porous media with graded geometrical properties is evaluated. A two-dimensional axisymmetric model was implemented considering a non-equilibrium approach with detailed chemistry, which was implemented with the FGM technique. As a study case, it was evaluated the difference between two forms of creating a similar hydrodynamic stabilization mechanism. One of them is by using a porous burner with graded porosity that progressively increases the void area for the gas flow. The other is a porous burner of constant porosity, but with a conical shape with the same increasing void area for the gas flow.

The results have shown an increase in the stable range of a porous burner with graded porosity when compared with the conical burner. Moreover, the structure of the flame front submerged in a porous medium was evaluated in detail. For the lean mixture, a smooth and lower length profile was noted. It was observed that the mass flow rate was directed toward the flame tip, and the mass flow rate presented a non-uniform behavior along the flame. Although adiabatic condition was imposed on the wall, the flame temperature near the wall presented a sub-adiabatic value, contradicting the picture drawn from one-dimensional simulations. These lower temperatures next to the wall are important for the flame stabilization.

5 CONCLUSIONS AND FUTURE WORKS

In this thesis, a numerical study of stabilized flame in porous media in different configurations is evaluated. The Flamelet Generated Manifold method was implemented step-by-step in order to reduce the computational time. The validation was performed using a free premixed flame stabilized on a slot burner. The FGM method presented good qualitative and quantitative results when compared to the detailed chemistry even for a flame close to the blow-off limit. The main discrepancies occurred due to difficulties in mapping the thermochemical state of the system near the walls where combustion products at low temperatures (around 300 K) are found. Such difficulty is not a limitation for the present porous burners analysis, considering that the flame front stabilizes far from the region with low temperature. In addition, a detailed comparison of the burning velocity along the flame surface revealed the effects of the heat loss to the burner rim and the pure curvature effect at the flame tip.

Subsequently, the one-dimensional model of a porous burner was employed, assuming detailed chemistry and non-equilibrium. The FGM technique has been extended to solve the chemistry coupled with the solid phase, which includes the pre-heating of the reactants. Good quantitative results of CO mass fraction, gas and solid phase temperature in steady-state and transient were found. Secondly, it was evaluated the stable flames that precede the blowoff imposing different porosities and solid thermal conductivities. These results were considered as the initial condition to evaluate the behavior of the solid and gas phase when imposed a pulse at the inlet flow of reactants. The results show a different response time for each phase, showing a complex behavior that was evaluated in the present thesis. A characteristic displacement velocity of the flame front is identified. This velocity dictates the time for blow-off.

In the last results chapter, the model is extended to a two-dimensional simulation where it is evaluated the differences between two forms of creating a similar hydrodynamic stabilization mechanism. One of them is by using a porous burner with graded porosity that progressively increases the void area for the gas flow. The other is a porous burner of constant porosity, but with a conical shape with the same increasing void area for the gas flow. This evaluation is motivated by the new technology of additive manufacturing. This technique been able to create a porous matrix with variable pore diameter and

porosity along the domain. The results have shown an increase in the stable range of a porous burner with graded porosity when compared with the conical burner with the same void area. Moreover, the structure of two-dimensional flame front submerged in a porous medium was evaluated in detail.

In summary, the present study evaluated numerically two distinct configurations of porous burner unexplored in literature. Firstly, a transient evaluation of porous burner when imposed to a mass flux rate pulse, describing in detail the behavior of each phase, and evaluating the stable range. Secondly, the results have shown advantages when a porous burner with variable pore and porosity has been imposed. Both studies were solved using detailed chemistry using the FGM method. Such methodology has been explained in detail step-by-step in the present work in view of any literature that has been explained in details FGM method applied in porous burners configuration.

The main contributions of the present work can be divided in the following:

- a comparison of the burning velocity along the flame surface revealed that the FGM is able to capture the effects of the heat loss along the flame front;
- a detailed implementation and validation of FGM technique for a flame stabilized within a porous burner in steady and transient regime. Although it is possible to find studies using the FGM technique applied in a burner, none of them have presented the implementation of the methodology in detail;
- an evaluation of T_s , T_g , v_{in} , x_f , η_{rec} and η_{rad} in a one-dimensional burner in the conditions that precede the blowoff limit for a range of porosity and solid thermal conductivity.
- an evaluation of the transient response of porous burner when subjected a different oscillation (rectangular pulse with different period and magnitude); showing in detail the behavior of each phase in transient regime.
- a comparison between two distinct configurations with similar hydrodynamic stabilization mechanisms in a two-dimensional simulation. Moreover, a detailed discussion about the heat exchange and the flow behavior near the flame front for each configuration was evaluated.

5.1 Future work

The study carried out throughout this thesis does opens a wide range of possibilities, considering the number of freedom degrees that porous burners allow us to assess. Below are some possibilities of relevant projects and numerical implementations that could be carried out to expand the knowledge in the field:

1. To implement a semi-analytical model in a transient approach to find adimensional numbers able to clarify the weight of each parameter imposed. The results could bring insight and new possibilities of stabilizing the flame in different inlet mass flow oscillations and porous matrix properties.
2. To evaluate the flame stability within inert porous media subjected to flow oscillations in two and three-dimensional configurations. A non-uniform flame front profile, as found in the chapter 4 of the present study, when subjected to flow oscillation could bring complex physics near the flame front. Studies assessing details near the flame front in multidimensional configuration has been scarcely found in the literature [Chen et al., 2018; Wang et al., 2019a]. Moreover, a numerical study combining a flow oscillation imposed in the inlet and a porous matrix with graded porosity and pore diameter could be developed. Which could increase the knowledge and limitations involving a porous burner with graded porosity.
3. To evaluate the flame stability with porous media with graded geometrical properties using different profiles of pore diameter and porosity. The recent possibility of building a porous matrix with precise control of pore diameter and porosity gives rise to a need for new porous matrices with a wide stable range when compared with traditional approaches. An interesting approach would be the implementation of a multiparametric analysis applied in porous media recently implemented by [Fidalgo et al., 2021] to maximize the radiation efficiency. For future studies, the suggestion would be to find the pore diameter and porosity along the domain to maximize the stable range and/or maximize the radiant efficiency.
4. The numerical models implemented present some simplifications that could be explored by the group in future studies. For example, the Lewis number (Le) equals the unity. Studies involving fuels as H_2 could bring imprecise results due to the lower

Le. Improve the solid radiation model because Rosseland's approach is currently used. Moreover, it could be implementing the Neumann boundary condition for the enthalpy equation. It would allow the evaluation of scenarios as micro combustors with heat loss on the walls. To finalize, a methodology to evaluate the NO_x . A correct prediction of NO_x is essential for industrial projects.

BIBLIOGRAPHY

Akhtar, S., Piffaretti, S., and Shamim, T. Numerical investigation of flame structure and blowout limit for lean premixed turbulent methane-air flames under high pressure conditions, **Applied Energy**, vol. 228, p. 21–32, 2018.

Amatachaya, P. and Krittacom, B. Combustion Mechanism of Gas Porous Burner Installed an In-Line Tube-Bank Heat Exchanger, **Energy Procedia**, vol. 138, p. 50–55, 2017.

Bakry, A., Al-Salaymeh, A., Ala'a, H., Abu-Jrai, A., and Trimis, D. Adiabatic premixed combustion in a gaseous fuel porous inert media under high pressure and temperature: Novel flame stabilization technique, **Fuel**, vol. 90(2), p. 647–658, 2011.

Banerjee, A. and Paul, D. Developments and Applications of Porous Medium Combustion: A Recent Review, **Energy**, page 119868, 2021.

Barra, A. J., Diepvens, G., Ellzey, J. L., and Henneke, M. R. Numerical study of the effects of material properties on flame stabilization in a porous burner, **Combustion and Flame**, vol. 134(4), p. 369–379, 2003.

Bedoya, C., Dinkov, I., Habisreuther, P., Zarzalis, N., Bockhorn, H., and Parthasarathy, P. Experimental study, 1D volume-averaged calculations and 3D direct pore level simulations of the flame stabilization in porous inert media at elevated pressure, **Combustion and Flame**, vol. 162(10), p. 3740–3754, 2015.

Bongers, H., Van Oijen, J., and De Goey, L. Intrinsic low-dimensional manifold method extended with diffusion, **Proceedings of the Combustion Institute**, vol. 29(1), p. 1371–1378, 2002.

Bouma, P. and De Goey, L. Premixed combustion on ceramic foam burners, **Combustion and Flame**, vol. 119(1-2), p. 133–143, 1999.

Burcat, A. and C. Gardiner Jr, W., **Ideal Gas Thermochemical Data for Combustion and Air Pollution Use**, pages 489–538, 2000.

Burcat, A. and McBride, B. **Ideal Gas Thermodynamic Data for Combustion and Air-Pollution Use, Technion Aerospace Engineering (TAE) Report # 804 June 1997**, 1997.

Cailler, M., Darabiha, N., Veynante, D., and Fiorina, B. Building-up virtual optimized mechanism for flame modeling, **Proceedings of the Combustion Institute**, vol. 36(1), p. 1251–1258, 2017.

Catapan, R., Oliveira, A., and Costa, M. Non-uniform velocity profile mechanism for flame stabilization in a porous radiant burner, **Experimental Thermal and Fluid Science**, vol. 35(1), p. 172–179, 2011.

Chem1D. **One-dimensional Laminar Flame Code**. Eindhoven University of Technology, n.d.

Chen, L., Xia, Y.-F., Li, B.-W., and Shi, J.-R. Flame front inclination instability in the porous media combustion with inhomogeneous preheating temperature distribution, **Applied Thermal Engineering**, vol. 128, p. 1520–1530, 2018.

Coelho, P. and Costa, M. Combustão, **Edições Orion**, vol. 1, 2007.

de Goey, L. and ten Thijs Boonkcamp, J. A flamelet description of premixed laminar flames and the relation with flame stretch, **Combustion and Flame**, vol. 119(3), p. 253 – 271, 1999.

de Goey, L. P. H. and ten Thijs Boonkcamp, J. H. M. A Mass-Based Definition of Flame Stretch for Flames with Finite Thickness, **Combustion Science and Technology**, vol. 122(1-6), p. 399–405, 1997.

Djordjevic, N., Habisreuther, P., and Zarzalis, N. A numerical investigation of the flame stability in porous burners employing various ceramic sponge-like structures, **Chemical engineering science**, vol. 66(4), p. 682–688, 2011.

Djordjevic, N., Habisreuther, P., and Zarzalis, N. Porous burner for application in stationary gas turbines: an experimental investigation of the flame stability, emissions and temperature boundary condition, **Flow, turbulence and combustion**, vol. 89(2), p. 261–274, 2012.

Donini, A., Bastiaans, R., van Oijen, J., and de Goey, L. Differential diffusion effects inclusion with flamelet generated manifold for the modeling of stratified premixed cooled flames, **Proceedings of the Combustion Institute**, vol. 35(1), p. 831 – 837, 2015a.

Donini, A., Bastiaans, R., van Oijen, J., and de Goey, L. **The implementation of 5-d FGM for LES of a gas turbine model combustor with heat loss**. In *Direct and Large-Eddy Simulation X*, pages 361–366. Springer, 2018.

Donini, A., Bastiaans, R. J., van Oijen, J. A., and de Goey, L. P. H. **The implementation of five-dimensional fgm combustion model for the simulation of a gas turbine model combustor**. In *ASME turbo expo 2015: turbine technical conference and exposition*, pages V04AT04A007–V04AT04A007. American Society of Mechanical Engineers, 2015b.

Donini, A. A. **Advanced turbulent combustion modeling for gas turbine application**. PhD thesis, Technische Universiteit Eindhoven, 2014.

Efimov, D. V., de Goey, P., and van Oijen, J. A. QFM: quenching flamelet-generated manifold for modelling of flame–wall interactions, **Combustion Theory and Modelling**, pages 1–33, 2019.

Ellzey, J. L., Belmont, E. L., and Smith, C. H. Heat recirculating reactors: Fundamental research and applications, **Progress in Energy and Combustion Science**, vol. 72, p. 32–58, 2019.

EPE. **Brazilian Energy Balance 2016**. Empresa de Pesquisa Energética, Rio de Janeiro, 2017.

Ergun, S. Fluid flow through packed columns, **Chem. Eng. Prog.**, vol. 48, p. 89–94, 1952.

Fidalgo, M. F., Mendes, M. A., and Pereira, J. M. An automated method for efficient multi-parametric analysis of porous radiant burner performance, **International Journal of Thermal Sciences**, vol. 163, p. 106851, 2021.

Fiorina, B., Baron, R., Gicquel, O., Thevenin, D., Carpentier, S., Darabiha, N., et al. Modelling non-adiabatic partially premixed flames using flame-prolongation of ILDM, **Combustion Theory and Modelling**, vol. 7(3), p. 449–470, 2003.

Frenklach, M., Wang, H., Yu, C., Goldenberg, M., Bowman, C., Hanson, R., Davidson, D., Chang, E., Smith, G., Golden, D., et al. Gri-mech-1.2, an optimized detailed chemical reaction mechanism for methane combustion, **Gas Research Institute**, vol. , 1995.

Ganter, S., Straßacker, C., Kuenne, G., Meier, T., Heinrich, A., Maas, U., and Janicka, J. Laminar near-wall combustion: Analysis of tabulated chemistry simulations by means of detailed kinetics, **International Journal of Heat and Fluid Flow**, vol. 70, p. 259–270, 2018.

Gao, H., Feng, X., and Qu, Z. Combustion in a Hybrid Porous Burner Packed with Alumina Pellets and Silicon Carbide Foams with a Gap, **Journal of Energy Engineering**, vol. 143(5), p. 04017032, 2017.

Ghorashi, S. A., Hashemi, S. A., Mollamahdi, M., Ghanbari, M., and Mahmoudi, Y. Experimental investigation on flame characteristics in a porous-free flame burner, **Heat and Mass Transfer**, pages 1–8, 2020.

Gicquel, O., Darabiha, N., and Thévenin, D. Liminar premixed hydrogen/air counterflow flame simulations using flame prolongation of ILDM with differential diffusion, **Proceedings of the Combustion Institute**, vol. 28(2), p. 1901–1908, 2000.

Giovannoni, V., Sharma, R. N., and Raine, R. R. Premixed combustion of methane–air mixture stabilized over porous medium: A 2D numerical study, **Chemical Engineering Science**, vol. 152, p. 591–605, 2016.

Habib, R., Yadollahi, B., Saeed, A., Doranehgard, M. H., and Karimi, N. On the Response of Ultralean Combustion of CH₄/H₂ Blends in a Porous Burner to Fluctuations in Fuel Flow—an Experimental Investigation, **Energy & Fuels**, vol. 35(10), p. 8909–8921, 2021a.

Habib, R., Yadollahi, B., Saeed, A., Doranehgard, M. H., Li, L. K., and Karimi, N. Unsteady ultra-lean combustion of methane and biogas in a porous burner—An experimental study, **Applied Thermal Engineering**, vol. 182, p. 116099, 2021b.

Hardesty, D. and Weinberg, F. Burners producing large excess enthalpies, **Combustion Science and Technology**, vol. 8(5-6), p. 201–214, 1973.

Hashemi, S. M. and Hashemi, S. A. Numerical investigation of the flame stabilization in a divergent porous media burner, **Proceedings of the Institution of Mechanical Engineers, Part A: Journal of Power and Energy**, vol. 231(3), p. 173–181, 2017.

Horsman, A. and Daun, K. Design optimization of a two-stage porous radiant burner through response surface modeling, **Numerical Heat Transfer, Part A: Applications**, vol. 60(9), p. 727–745, 2011.

Howell, J. R., Menguc, M. P., and Siegel, R. **Thermal radiation heat transfer**. CRC press, 2010.

Hsu, P.-F., Howell, J., and Matthews, R. A numerical investigation of premixed combustion within porous inert media, **Journal of heat transfer**, vol. 115(3), p. 744–750, 1993.

Hsu, P.-f. and Howell, J. R. Measurements of thermal conductivity and optical properties of porous partially stabilized zirconia, **Experimental Heat Transfer An International Journal**, vol. 5(4), p. 293–313, 1992.

IEA. **Key World Energy Statistics**. International Energy Agency, 2017.

IEA. **Key World Energy Statistics**. International Energy Agency, 2021.

Ihme, M., Shunn, L., and Zhang, J. Regularization of reaction progress variable for application to flamelet-based combustion models, **Journal of Computational Physics**, vol. 231(23), p. 7715–7721, 2012.

Kaushik, L. K., Mahalingam, A. K., and Palanisamy, M. Performance analysis of a biogas operated porous radiant burner for domestic cooking application, **Environmental Science and Pollution Research**, pages 1–10, 2020.

Kaviany, M. **Principles of convective heat transfer**, 2013.

Kazakov, A. and Frenklach, M. **DrM22, University of California at Berkeley, Berkeley, CA**, vol. 21, p. 2017, 1995.

Keramiotis, C., Stelzner, B., Trimis, D., and Founti, M. Porous burners for low emission combustion: An experimental investigation, **Energy**, vol. 45(1), p. 213–219, 2012.

Kim, N. I. and Maruta, K. A numerical study on propagation of premixed flames in small tubes, **Combustion and flame**, vol. 146(1-2), p. 283–301, 2006.

Lacroix, M., Nguyen, P., Schweich, D., Huu, C. P., Savin-Poncet, S., and Edouard, D. Pressure drop measurements and modeling on SiC foams, **Chemical engineering science**, vol. 62(12), p. 3259–3267, 2007.

Lammers, F. and De Goey, L. A numerical study of flash back of laminar premixed flames in ceramic-foam surface burners, **Combustion and Flame**, vol. 133(1-2), p. 47–61, 2003.

Lammers, F. and De Goey, L. The influence of gas radiation on the temperature decrease above a burner with a flat porous inert surface, **Combustion and flame**, vol. 136(4), p. 533–547, 2004.

Law, C. **Combustion Physics**. Cambridge University Press, 1st edition, 2006.

Law, C. K. **Combustion physics**. Cambridge university press, 2010.

Li, J., Li, Q., Shi, J., Liu, X., and Guo, Z. Numerical study on heat recirculation in a porous micro-combustor, **Combustion and flame**, vol. 171, p. 152–161, 2016.

Liu, H., Dong, S., Li, B.-W., and Chen, H.-G. Parametric investigations of pre-mixed methane–air combustion in two-section porous media by numerical simulation, **Fuel**, vol. 89(7), p. 1736–1742, 2010.

Liu, Y., Fan, A., Yao, H., and Liu, W. Numerical investigation of filtration gas combustion in a mesoscale combustor filled with inert fibrous porous medium, **International Journal of Heat and Mass Transfer**, vol. 91, p. 18–26, 2015.

Maas, U. and Pope, S. B. Simplifying chemical kinetics: intrinsic low-dimensional manifolds in composition space, **Combustion and flame**, vol. 88(3), p. 239–264, 1992.

McBride, B. J., Gordon, S., and Reno, M. A. Coefficients for calculating thermodynamic and transport properties of individual species, vol. 1, 1993.

Mujeebu, M. A., Abdullah, M. Z., Bakar, M. A., Mohamad, A., and Abdullah, M. Applications of porous media combustion technology—a review, **Applied energy**, vol. 86(9), p. 1365–1375, 2009.

Oijen, J. v. and Goey, L. d. Modelling of premixed laminar flames using flamelet-generated manifolds, **Combustion Science and Technology**, vol. 161(1), p. 113–137, 2000.

Ortona, A., Bianchi, G., and Gianella, S. Design and additive manufacturing of periodic ceramic architectures, **Journal of Ceramic Science and Technology**, 2017.

Pantangi, V., Mishra, S. C., Muthukumar, P., and Reddy, R. Studies on porous radiant burners for LPG (liquefied petroleum gas) cooking applications, **Energy**, vol. 36(10), p. 6074–6080, 2011.

Pereira, F. M. et al. Medição de características térmicas e estudo do mecanismo de estabilização de chama em queimadores porosos radiantes, 2002.

Peters, N. Laminar diffusion flamelet models in non-premixed turbulent combustion, **Progress in Energy and Combustion Science**, vol. 10(3), p. 319 – 339, 1984.

Peters, N. **Numerical and asymptotic analysis of systematically reduced reaction schemes for hydrocarbon flames**. In *Numerical simulation of combustion phenomena*, pages 90–109. Springer, 1985.

Peters, N. and Rogg, B. Reduced kinetic mechanisms for applications in combustion systems, **Lecture Notes in Physics**, vol. 15, 1993.

Pierce, C. D. and Moin, P. Progress-variable approach for large-eddy simulation of non-premixed turbulent combustion, **Journal of fluid Mechanics**, vol. 504, p. 73–97, 2004.

Poinsot, T. and Veynante, D. **Theoretical and numerical combustion**. RT Edwards, Inc., 2005.

Pope, S. B. Computationally efficient implementation of combustion chemistry using in situ adaptive tabulation, vol. , 1997.

Popp, P. and Baum, M. Analysis of wall heat fluxes, reaction mechanisms, and unburnt hydrocarbons during the head-on quenching of a laminar methane flame, **Combustion and Flame**, vol. 108(3), p. 327–348, 1997.

Qiu, K. and Hayden, A. Premixed gas combustion stabilized in fiber felt and its application to a novel radiant burner, **Fuel**, vol. 85(7-8), p. 1094–1100, 2006.

Ramaekers, W. **Development of flamelet generated manifolds for partially-premixed flame simulations**. PhD thesis, Ph. D. Thesis, Technical University Eindhoven, The Netherlands, 2011.

Sahraoui, M. and Kaviany, M. Direct simulation vs volume-averaged treatment of adiabatic, premixed flame in a porous medium, **International Journal of Heat and Mass Transfer**, vol. 37(18), p. 2817–2834, 1994.

Sathe, S., PECK, R. E., and Tong, T. W. Flame stabilization and multimode heat transfer in inert porous media: a numerical study, **Combustion Science and Technology**, vol. 70(4-6), p. 93–109, 1990.

Smith, G. P., Golden, D. M., Frenklach, M., Moriarty, N. W., Eiteneer, B., Goldenberg, M., Bowman, C. T., Hanson, R. K., Song, S., Gardiner Jr, W. C., et al. **GRMech 3.0 reaction mechanism**, Berkeley, 2012.

Smooke, M. D. and Giovangigli, V. Formulation of the premixed and nonpremixed test problem, **Lecture Notes in Physics**, vol. 384, p. 1–28, 1991a.

Smooke, M. D. and Giovangigli, V. **Premixed and nonpremixed test problem results**. In *Reduced kinetic mechanisms and asymptotic approximations for methane-air flames*, pages 29–47. Springer, 1991b.

Smucker, M. T. and Ellzey, J. L. Computational and experimental study of a two-section porous burner, **Combustion science and Technology**, vol. 176(8), p. 1171–1189, 2004.

Sobhani, S., Mohaddes, D., Boigne, E., Muhunthan, P., and Ihme, M. Modulation of heat transfer for extended flame stabilization in porous media burners via topology gradation, **Proceedings of the Combustion Institute**, 2018.

Sobhani, S., Muhunthan, P., Boigné, E., Mohaddes, D., and Ihme, M. Experimental feasibility of tailored porous media burners enabled via additive manufacturing, **Proceedings of the Combustion Institute**, 2020.

Sobhani, S., Muhunthan, P., Boigné, E., Mohaddes, D., and Ihme, M. Experimental feasibility of tailored porous media burners enabled via additive manufacturing, **Proceedings of the Combustion Institute**, vol. 38(4), p. 6713–6722, 2021.

Somers, L. **The simulation of flat flames with detailed and reduced chemical models**. PhD thesis, 1994.

Somers, L. M. and De Goey, L. A numerical study of a premixed flame on a slit burner, **Combustion science and technology**, vol. 108(1-3), p. 121–132, 1995.

Takeno, T. and Sato, K. An excess enthalpy flame theory, **Combustion Science and Technology**, vol. 20(1-2), p. 73–84, 1979.

Tonse, S. R., Moriarty, N. W., Brown, N. J., and Frenklach, M. PRISM: Piecewise reusable implementation of solution mapping. An economical strategy for chemical kinetics, **Israel Journal of Chemistry**, vol. 39(1), p. 97–106, 1999.

Turns, S. R. et al. **An introduction to combustion**. volume 499. McGraw-hill New York, 1996.

van Oijen, J. and de Goey, L. Modelling of premixed counterflow flames using the flamelet-generated manifold method, **Combustion Theory and Modelling**, vol. 6(3), p. 463–478, 2002.

Van Oijen, J., Donini, A., Bastiaans, R., ten Thije Boonkkamp, J., and De Goey, L. State-of-the-art in premixed combustion modeling using flamelet generated manifolds, **Progress in Energy and Combustion Science**, vol. 57, p. 30–74, 2016.

Van Oijen, J., Lammers, F., and De Goey, L. Modeling of complex premixed burner systems by using flamelet-generated manifolds, **Combustion and Flame**, vol. 127(3), p. 2124–2134, 2001.

van Oijen, J., Lammers, F., and de Goey, L. Modeling of complex premixed burner systems by using flamelet-generated manifolds, **Combustion and Flame**, vol. 127, p. 2124 – 2134, 2001.

van Oijen, J. A. **Flamelet-Generated Manifolds: development and application to premixed laminar flames**. PhD thesis, Eindhoven University of Technology, 2002.

van Oijen, J. A. and de Goey, L. P. H. Modelling of Premixed Laminar Flames using Flamelet-Generated Manifolds, **Combustion Science and Technology**, vol. 161(1), p. 113–137, 2000.

Vandadi, V., Wu, H., Kwon, O. C., Kaviany, M., and Park, C. Multiscale thermal nonequilibria for record superadiabatic-radiant-burner efficiency: Experiment and analyses, **International Journal of Heat and Mass Transfer**, vol. 106, p. 731–740, 2017.

Verhoeven, L., Ramaekers, W., Van Oijen, J., and De Goey, L. Modeling non-premixed laminar co-flow flames using flamelet-generated manifolds, **Combustion and Flame**, vol. 159(1), p. 230–241, 2012.

Versteeg, H. K. and Malalasekera, W. **An introduction to computational fluid dynamics: the finite volume method**. Pearson Education, 2007.

Voss, S., Mendes, M., Pereira, J., Ray, S., Pereira, J., and Trimis, D. Investigation on the thermal flame thickness for lean premixed combustion of low calorific H₂/CO mixtures within porous inert media, **Proceedings of the Combustion Institute**, vol. 34(2), p. 3335–3342, 2013.

Wang, G., Tang, P., Li, Y., Xu, J., and Durst, F. Flame front stability of low calorific fuel gas combustion with preheated air in a porous burner, **Energy**, vol. 170, p. 1279–1288, 2019a.

Wang, W., Zuo, Z., and Liu, J. Experimental study and numerical analysis of the scaling effect on the flame stabilization of propane/air mixture in the micro-scale porous combustor, **Energy**, vol. 174, p. 509–518, 2019b.

Williams, F. A. **Combustion theory**. CRC Press, 1994.

Yakovlev, I. and Zambalov, S. Three-dimensional pore-scale numerical simulation of methane-air combustion in inert porous media under the conditions of upstream and downstream combustion wave propagation through the media, **Combustion and Flame**, vol. 209, p. 74–98, 2019.

Yang, H., Minaev, S., Geynce, E., Nakamura, H., and Maruta, K. Filtration combustion of methane in high-porosity micro-fibrous media, **Combustion science and technology**, vol. 181(4), p. 654–669, 2009.

Younis, L. and Viskanta, R. Experimental determination of the volumetric heat transfer coefficient between stream of air and ceramic foam, **International journal of heat and mass transfer**, vol. 36(6), p. 1425–1434, 1993.

Yu, B., Kum, S.-M., Lee, C.-E., and Lee, S. Combustion characteristics and thermal efficiency for premixed porous-media types of burners, **Energy**, vol. 53, p. 343–350, 2013.

Zeng, H., Wang, Y., Shi, Y., Ni, M., and Cai, N. Syngas production from CO₂/CH₄ rich combustion in a porous media burner: Experimental characterization and elementary reaction model, **Fuel**, vol. 199, p. 413–419, 2017.

Zheng, C., Cheng, L., Saveliev, A., Luo, Z., and Cen, K. Numerical studies on flame inclination in porous media combustors, **International journal of heat and mass transfer**, vol. 54(15-16), p. 3642–3649, 2011.

APPENDIX A – Mathematical formulation of premixed laminar flames

A.1 Introduction

This appendix presents the equations required to describe the combustion of laminar premixed flames. In the first part, some relations and the equation of state are described. In the second part, the conservation of mass, momentum, species and energy are presented. Many authors present the detailed derivation [Versteeg and Malalasekera, 2007; Poinso and Veynante, 2005; Turns et al., 1996; Coelho and Costa, 2007; Law, 2010; Williams, 1994], therefore they are presented only in their final form.

A.2 Properties of gaseous mixtures and equation of state

In the present work, mass fraction and molar fraction will be presented by Equations A.1a and A.2a, respectively. Note that, by definition, the sum of all molar and mass fraction must be unity (Equations A.1b and A.2b).

$$Y_i = \frac{m_i}{m_t}, \quad (\text{A.1a})$$

$$\sum_{i=1}^{N_s} Y_i = 1 \quad (\text{A.1b})$$

and

$$X_i = \frac{n_i}{n_t}, \quad (\text{A.2a})$$

$$\sum_{i=1}^{N_s} X_i = 1. \quad (\text{A.2b})$$

In these equations m_i [kg] is the mass of the species i and m_t [kg] is the total mass of the system. The number of species is defined by N_s . The symbol n_i is the number of the mols of the species i and n_t is the total number of mols of the system. In combustion, the gases can be treated as ideal gases, according to

$$pV = n_t R_o T, \quad (\text{A.3})$$

where V [m^3] is the volume, $R_o = 8314$ [J/mol.K] is the ideal gas constant, T [K] is the temperature and p [Pa] is the thermodynamic pressure. The average molar mass MW

[kg/mol] is defined as

$$MW = \left(\sum_{i=1}^N \frac{Y_i}{M_i} \right)^{-1}, \quad (\text{A.4})$$

where the MW_i is molar mass of species i . The absolute enthalpy of a substance can be obtained by the sum of the enthalpy of formation h_{ref}° [J/kg] and sensible enthalpy $\Delta h_i(T)$ [J/kg] as

$$h_i = h_{ref}^\circ + \Delta h_i(T). \quad (\text{A.5})$$

Considering an ideal gas, the $\Delta h_i(T)$ is obtained by

$$\Delta h_i(T) = \int_{T_{ref}}^T c_{pi} dT. \quad (\text{A.6})$$

The c_{pi} are specific heat capacity at constant pressure of species i and T_{ref} is the reference temperature. For gaseous mixture, the specific heat c_p [J/kg.K] can be calculated as

$$c_p = \sum_{i=1}^N Y_i c_{pi}. \quad (\text{A.7})$$

The value of the specific heats of the species i are obtained using a five degree polynomials [McBride et al., 1993; Burcat and McBride, 1997]

$$c_{pi} = (a_1 + a_2 T + a_3 T^2 + a_4 T^3 + a_5 T^4) \frac{R_o}{M_i}. \quad (\text{A.8})$$

The coefficient a_i are obtain by NASA polynomials and are stored in on the GRIMECH files [Smith et al., 2012].

The enthalpy of the mixture h [J/kg] is given by

$$h = \sum_{i=1}^N Y_i h_i. \quad (\text{A.9})$$

The equivalence ratio ϕ represents the relation between the fuel (m_f) and the oxidant (m_o) in the mixture in relation to the stoichiometry mixture, being defined as

$$\phi = \frac{\left(\frac{m_f}{m_o} \right)}{\left(\frac{m_f}{m_o} \right)_s}. \quad (\text{A.10})$$

If ϕ is equal to one, there is a stoichiometry mixture. In the case of $\phi < 1$, the mixture is considered poor, which mean that the oxidant quantity is higher than the necessary to burn all the fuel. On the other hand, when $\phi > 1$ the oxidant is below than

the necessary to a stoichiometric combustion, and the mixture is called rich.

A.3 Conservation equations

Continuity equation

The continuity equation expresses the mass conservation of the system. In the differential form, it is represented by

$$\frac{\partial \rho}{\partial t} + \frac{\partial(\rho u_k)}{\partial x_k} = 0, \quad (\text{A.11})$$

where t [s] is the time, u_k [m/s] is the mixture velocity and x_k is the spatial coordinates with k representing the three cartesian.

Momentum equation

The momentum conservation is described by the Navier-Stokes equations, which can be written as equation A.12. The two first terms are responsible for inertial forces. The term $-\frac{\partial p}{\partial x_i}$ is the pressure gradient and the last term (S_u [N/m^3]) is commonly used to modeling external forces, like gravity or magnetic forces (Lorentz forces, for example).

$$\frac{\partial(\rho u_k)}{\partial t} + \frac{\partial(\rho u_j u_k)}{\partial x_j} = -\frac{\partial p}{\partial x_k} + \frac{\partial \tau_{kj}}{\partial x_j} + S_u. \quad (\text{A.12})$$

The tensor stress τ_{kj} [N/m^2] is given by

$$\tau_{kj} = -\frac{2}{3}\mu \frac{\partial u_k}{\partial x_k} \delta_{kj} + \mu \left(\frac{\partial u_k}{\partial x_j} + \frac{\partial u_j}{\partial x_k} \right). \quad (\text{A.13})$$

The δ_{kj} is called Kronecker delta and the symbol μ [Pa.s] is the dynamic viscosity. To calculate it with reduced computational cost, the following equation is considered [Smooke and Giovangigli, 1991a]:

$$\mu/c_p = 1.67 \times 10^{-8} (T/298)^{0.51}. \quad (\text{A.14})$$

Species transport equation

One form to represent the species conservation equation is through the equation A.15 where the first two terms represent, respectively, the temporal variation the chemical

and the advective transport of specie i .

$$\frac{\partial(\rho Y_i)}{\partial t} + \frac{\partial(\rho u_k Y_i)}{\partial x_k} = -\frac{\partial j_{k,i}}{\partial x_k} + \dot{\omega}_i. \quad (\text{A.15})$$

The mass diffusion of species has three contributions (temperature, pressure and concentration gradients). The mass diffusion by temperature gradient (Soret effect) is only important for species with low molecular weight as in hydrogen combustion, thus it will be neglected in the present study. The effects of pressure are neglected due to the small pressure gradient. The effects of concentration gradients are considered. This contribution is modeled by Fick's Law

$$j_{k,i} = -\rho D_{i,M} \frac{\partial Y_i}{\partial x_k}. \quad (\text{A.16})$$

The Lewis number Le [-] is defined as

$$Le_i = \frac{k}{\rho D_{i,M} c_p}. \quad (\text{A.17})$$

The diffusion coefficient of species i into the mixture being $D_{i,M}$ [m^2/s]. If the Le_i can be considered constant and by using the equation A.16, it is possible to rewrite the equation A.15 as

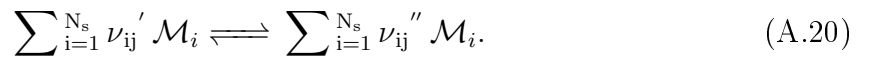
$$\frac{\partial(\rho Y_i)}{\partial t} + \frac{\partial(\rho u_k Y_i)}{\partial x_k} = \frac{\partial}{\partial x_k} \left(\frac{k}{Le_i c_p} \frac{\partial Y_i}{\partial x_k} \right) + \dot{\omega}_i. \quad (\text{A.18})$$

Combustion Chemistry

The species transport equation is introduced, but the chemical source term $\dot{\omega}_i$ [kg/m^3s] are not specified yet. They contain the contribution of all chemical reactions. It can be determined by

$$\dot{\omega}_i = M_i \sum_{j=1}^{N_r} (\nu''_{ij} - \nu'_{ij}) r_j, \quad (\text{A.19})$$

with N_r being the number of reactions, ν''_{ij} and ν'_{ij} are the stoichiometry coefficients of *reactants* and *products* respectively, which indicate how many molecules of specie i take part in reaction j . The generic form can be written:



The \mathcal{M}_i represents species i . The r_j [mol/m^3s] described in equation A.19 is the reaction rate for elementary reaction j . It is written on form:

$$r_j = \mathbf{k}_j^f \prod_{i=1}^{N_s} \left[\frac{\rho Y_i}{M_i} \right]^{\nu'_{ij}} - \mathbf{k}_j^b \prod_{i=1}^{N_s} \left[\frac{\rho Y_i}{M_i} \right]^{\nu''_{ij}}, \quad j = 1, N_r \quad (\text{A.21})$$

here \mathbf{k}_j [-] is the reaction rate coefficient and superscripts f and b refer respectively to *forward* and *backward* (on the chemical reaction). A classical expression to determine \mathbf{k}_j [-] is given by Arrhenius equation:

$$\mathbf{k}_j = A_j T^{\beta_j} \exp\left(\frac{-E_{a,j}}{RT}\right), \quad (\text{A.22})$$

where A_j is the pre-exponential constant, β_j [-] the temperature exponent and $E_{a,j}$ [J] the activation energy. They are obtained of elementary reaction and stored [Smith et al., 2012].

Energy equation

The energy conservation is formulated in terms of the specific enthalpy h as

$$\frac{\partial(\rho h)}{\partial t} + \frac{(\rho u_k h)}{\partial x_k} = \frac{\partial q_k}{\partial x_k} + S_h. \quad (\text{A.23})$$

In the present combustion modeling, the pressure material derivative (DP/Dt) and viscous dissipation ($\tau_{kj} \partial u_k / \partial x_j$) are neglected for low Mach number [Coelho and Costa, 2007]. The diffusive heat flux q_k [W/m^2] has three contributions:

$$q_k = q_k^c + q_k^D + q_k^d \quad (\text{A.24})$$

being:

$$q_k^c = -\frac{k}{c_p} \frac{\partial h}{\partial x_k}. \quad (\text{A.25})$$

The term represents heat diffusion term expressed by Fourier's Law. The parameter k [W/m.K] is the thermal conductivity and it can be obtained with reduced computational time using [Smooke and Giovangigli, 1991a]:

$$k/c_p = 2.58 \times 10^{-5} (T/298)^{0.69}. \quad (\text{A.26})$$

The q_k^D is called *Dufour effect*, it is caused by the concentration gradient and it is negligible in combustion processes. The q_k^d [W/m^2] is the contribution of enthalpy flux due the mass

diffusion

$$q_k^d = \sum_{i=1}^N h_i j_{k,i}. \quad (\text{A.27})$$

Reorganizing the A.23, A.25, A.16, A.27 and A.17 the energy equation can be written as

$$\frac{\partial(\rho h)}{\partial t} + \frac{(\rho u_k h)}{\partial x_k} = \frac{\partial}{\partial x_k} \left(\frac{k}{c_p} \frac{\partial h}{\partial x_k} + \frac{k}{c_p} \sum_{i=1}^N \left(\frac{1}{Le_i} - 1 \right) h_i \frac{\partial Y_i}{\partial x_k} \right) + S_h. \quad (\text{A.28})$$

APPENDIX B – Volume averaging method

The solution of fundamental set of transport equations, presented in Appendix A, for a porous burner requires a high computational time, because of the necessity to apply direct numerical simulation. Thereby, the present study regards the method of volume averaging with assumptions that bring the advantage of treating the porous burner as a homogeneous medium with effective properties. It allows a reduced computational time, a more simple mathematical formulation, and to avoid the creation of a complex mesh (pore scale). The present Appendix shows the main steps of the volume-averaged method applied in solid energy equation. More details about the methodology and a detailed deduction of the intermediate steps can be found in Kaviany [2013].

The volume-averaged method is based to average the property of the interest (ψ) in a volume of integration (V) defined as

$$\langle \psi \rangle = \frac{1}{V} \int_V \psi dV, \quad (\text{B.1})$$

where $\langle \rangle$ denotes volume averaging. To calculate the average of a solid-phase property ψ_s over the solid-phase volume is applied

$$\langle \psi \rangle^s = \frac{1}{V_s} \int_V \psi_s dV = \frac{\langle \psi_s \rangle}{1 - \varepsilon}. \quad (\text{B.2})$$

where ε is defined as the porosity as

$$\varepsilon = \frac{V_g}{V_g + V_s} = \frac{1 - V_s}{V}. \quad (\text{B.3})$$

One of the assumptions of the volume averaging method is $l_p \ll l_V \ll L$, where l_p is the pore characteristic length-scale, l_V is the characteristic length-scale of the control volume and L is the characteristic length-scale of the domain considered. Moreover, phenomenological scales have to be separated. For instance, for conduction heat transfer, it is required that

$$\Delta T_{l_p} \ll \Delta T_V \ll \Delta T_L \quad (\text{B.4})$$

where ΔT is the maximum temperature difference across respective length-scale. When the combustion phenomena is involved, this condition around the flame region could not

be obeyed because the flame thickness may be of the same order or smaller than the pore diameter. This condition represents a severe limitation to the volume-averaging modeling of combustion in porous media.

By Comparing a two dimensional domain imposing a direct simulation and the volume-averaged models for the combustion in porous media, it is possible to show that multiple flame velocities exist as the flame is displaced within a pore, a behavior not predicted by homogeneous models. Additionally, the flame temperature is under-predicted by the volume-averaged model [Sahraoui and Kaviany, 1994]. Studies using a numerical simulations in pore-scale with detailed simulation in a complex domain can be found [Yakovlev and Zambalov, 2019; Djordjevic et al., 2011].

The final form the gradient of scalar ψ_s and divergent of vector $\vec{\phi}_s$ when the volume averaging is applied, can be written as

$$\langle \nabla \psi \rangle^s = \nabla \langle \psi \rangle^s + \frac{1}{V_s} \int_{A_{gs}} \psi_s dA \quad (\text{B.5})$$

and

$$\langle \nabla \cdot \vec{\phi}_s \rangle^s = \nabla \cdot \langle \vec{\phi} \rangle^s + \frac{1}{V_s} \int_{A_{gs}} \vec{\phi} \cdot \hat{n}_{gs} dA. \quad (\text{B.6})$$

To exemplify the steps involved in the volume average method, it is considered the solid energy equation in the transient regime

$$(\rho c_p) \frac{\partial T}{\partial t} = \nabla \cdot (k_s \nabla T). \quad (\text{B.7})$$

Applying of method in each term, the result is

$$(\rho_s C_s) \frac{\partial \langle T \rangle^s}{\partial t} = \nabla \cdot (k_s \nabla \langle T \rangle^s + \frac{k_s}{V_s} \int_{A_{gs}} \hat{n}_{gs} T_s dA) + \frac{1}{V_s} \int_{A_{gs}} (k_s \nabla T_s) \cdot \hat{n}_{gs} dA \quad (\text{B.8})$$

\hat{n}_{gs} is the unitary normal vector on interface between the solid and gas phase (A_{gs})

When the gas and solid phase can be treated as a continuum, but the local thermal non-equilibrium is desired, i.e., $\langle T \rangle^s \neq \langle T \rangle^g$, the local temperature for solid phase can be decomposed as

$$T_s = \langle T \rangle^s + T'_s. \quad (\text{B.9})$$

T'_s is defined as a local deviation from the intrinsic phase-averaged value $\langle T \rangle^s$. This approach is applied to capture temperature variations on the face of control volume (integrals in the equation B.8). To simplify the notation, it is defined

$$\langle \nabla \psi \rangle^{A_{gs}} = \frac{1}{A_{gs}} \int_{A_{gs}} \psi dA \quad (\text{B.10})$$

in the equation B.8. Now, the solid energy equation is represented as

$$(\rho c_p) \frac{\partial \langle T \rangle^s}{\partial t} = \nabla \cdot (k_s \nabla \langle T \rangle^s) + \frac{k_s}{V_s} A_{gs} \langle \hat{n}_{gs} T'_s \rangle^{A_{gs}} + \frac{A_{gs}}{V_s} \langle \hat{n}_{gs} \cdot k_s \nabla T'_s \rangle^{A_{gs}} \quad (\text{B.11})$$

The T'_s term brings new unknowns terms. The problem is closed proposing a set of closure constitutive equations that combines the transformation functions and direct simulation. Some steps of application of transformation functions and algebraic manipulation have been omitted, but it can be found in Kaviany [2013]. Thus, solid energy equation assumes the form

$$\frac{\partial \langle T \rangle^s}{\partial t} = \frac{\langle \alpha \rangle^s}{(1 - \varepsilon)} \nabla \cdot (\nabla \langle T \rangle^s) + \frac{A_0 \alpha_s}{(1 - \varepsilon) d} \langle Nu \rangle^{sg} (\langle T \rangle^g - \langle T \rangle^s). \quad (\text{B.12})$$

This simplification does not consider the hydrodynamic dispersion in the fluid phases, among the other coupling mechanisms. Now, the $\langle \alpha \rangle^s$ is function of k_f , k_s , ε and structure parameters. Normally, the coefficients ($\langle Nu \rangle^{sg}$) have to be measured experimentally, and their range of application is narrow due to the large complexity of each configuration involved.

To simplify the notation, the present study considered a final form of solid energy, gas enthalpy (h), momentum and continuity equation as

$$(1 - \varepsilon) \rho_s C_s \frac{\partial T_s}{\partial t} = \nabla \cdot (k_{eff} \nabla T_s) + h_v (T_g - T_s), \quad (\text{B.13})$$

$$\nabla \cdot (\varepsilon \rho_g \vec{u} h) + \nabla \cdot (\varepsilon \frac{k_g}{C_g} \nabla h) = h_v (T_s - T_g), \quad (\text{B.14})$$

$$\frac{\partial (\varepsilon \rho_g \vec{u})}{\partial t} + \nabla \cdot (\varepsilon \rho_g \vec{u} \cdot \vec{u}) = -\nabla (\varepsilon p) + \nabla \cdot (\mu \nabla \vec{u}) + \varepsilon S \quad (\text{B.15})$$

and

$$\frac{\partial (\varepsilon \rho_g)}{\partial t} + \nabla (\varepsilon \rho_g \vec{u}) = 0, \quad (\text{B.16})$$

where h_v is the volumetric convective heat transfer coefficient, $k_{eff} = (1 - \varepsilon)k_s$ effective solid thermal conductivity, k_g gas thermal conductivity, S momentum source term, μ dynamic viscosity, ρ_g gas density and C_g gas specific heat.

Although simplifications to implement the methodology are needed, a large number of studies have imposed this formulation, and satisfactory numerical results has been obtained.

APPENDIX C – Flamelet Generated Manifold Technique

C.1 Introduction

Combustion presents a stiff non-linear coupling among chemical kinetics, fluid dynamics, and heat transfer processes. Thus, modeling flames in practical industrial applications using detailed reaction mechanisms is still prohibitive due to the high CPU-time required to solve a large number of species equations. This is why there is long-standing interest to develop reliable combustion models with high accuracy, but low computation time. Chemical reduction techniques intend to meet these requirements for numerical simulations of flames. One alternative is the reduction of chemical mechanisms assuming steady-state and partial equilibrium [Peters, 1985; Peters and Rogg, 1993]. In this approach, it is required a good knowledge about the reaction paths and time scales in order to select species and reactions to be eliminated from the set of equations. Additional difficulty is that species which can be assumed in steady-state at low temperatures, may not be in steady-state at high temperatures. This evaluation can be exhaustive and the results may not be accurate outside the range of conditions for which it is developed.

Other reduction methods assume that the flow time scale is much higher than the chemical time scales, hence flow and chemistry are decoupled. Two of the most popular applications of this assumption are the ILDM developed by Maas and Pope [1992] and the steady laminar flamelet model developed by Peters [1984]. However, the former is pointed out to lose accuracy in colder regions of the flame [van Oijen, 2002] while the later does not have the ability to describe ignition or extinction processes.

Thereby, van Oijen [2002] proposed the FGM technique to overcome these problems. In the FGM framework, a database representing the combustion process is built storing a set of laminar one-dimensional flames solved with detailed chemical kinetic (*flamelets*) as function of some control variables. In some cases, this method can be a hundred times faster than the direct integration of the conservation equations [van Oijen, 2002; Donini et al., 2015b] without losing much accuracy. Similar approaches as the FGM are FPV proposed by Pierce and Moin [2004] and the FPI proposed by Gicquel et al. [2000].

The benefits of the FGM have led to many studies in different configurations and the evaluation of different phenomena. Premixed flames were explored by van Oijen

and de Goey [2000] and Van Oijen et al. [2001]. Partially premixed and non-premixed flames were studied by Bongers et al. [2002]; Ramaekers [2011]; Verhoeven et al. [2012]. Furthermore, the FGM has also been applied in industrial configuration [Donini et al., 2018; Akhtar et al., 2018].

In this appendix, it is presented each part of the FGM technique implementation applied in this work. It will be presented in detail the flamelet formulation, the tabulation strategy and the interpolation procedures. Lastly, it is shown the implementation of the multidimensional modeling in a CFD code. It is emphasized that the present implementation has focus on the laminar premixed flames with heat losses in steady-state condition.

C.2 Application of FGM

The FGM is a chemistry reduction method that combines the advantages of chemistry reduction and flamelet methods. By solving one-dimensional flames with detailed kinetics, the most important aspects of the internal structure of the flame fronts are captured and stored as a function of a few independent control variables, for which transport equations are solved during run-time. Here lies one the main strengths of FGM technique, a complete combustion phenomena can be represented by solving a few number of transport equations.

The four steps to implement the FGM technique are shown in Figure C.1. In the first part, an ensemble of unidimensional laminar flames is calculated using detailed kinetics with the purpose to obtain scalars that represent the thermochemical state of the flame as temperature, composition, density, specific heat, etc. (**flamelets**). These scalars are tabulated in a manifold as a function of the progress variable (\mathcal{Y}) and enthalpy (h). They could be divided into two groups: the transport properties and additional scalars. The former is accessed during the multidimensional solution, while the additional scalars are retrieved only in the post-processing step. Thus, all scalars of interest are function of the control variables (**tabulation**). In the next step, a multidimensional laminar flow is solved with two additional transport equations (\mathcal{Y}, h). Thereby, the species conservation equations are no longer solved. The values of the transport properties are retrieved from the database by interpolation in each iteration. The simulation ends when the convergence of all differential equations are obtained (**multidimensional solution**). The final part

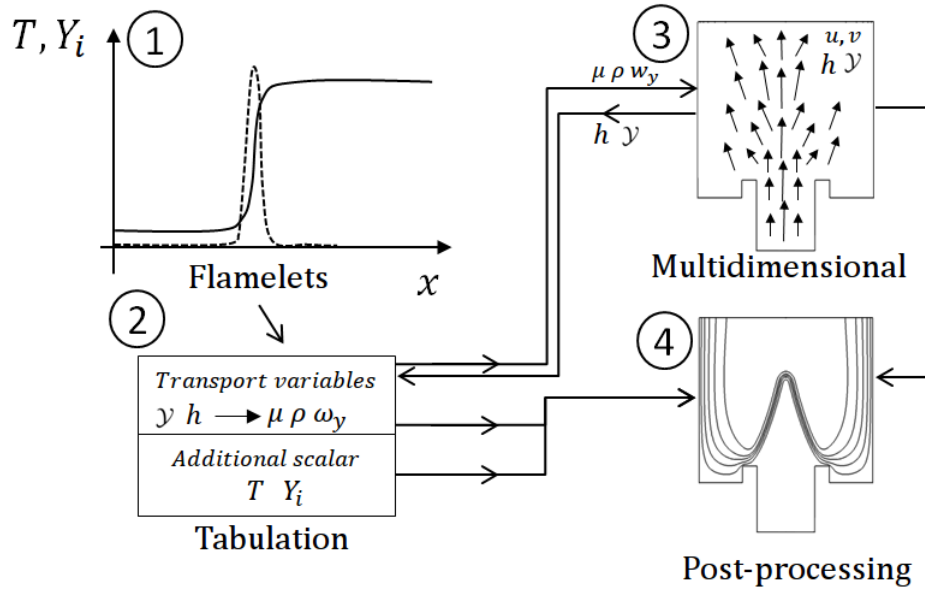


Figure C.1 – Flowchart of the implemented methodology.

is the post-processing step. Parameters like temperature and mass fractions (Y_i) are retrieved from the FGM database ($T(\mathcal{Y}, h)$) and ($Y_i(\mathcal{Y}, h)$) and the detailed flame structure is reconstructed (**post-processing**).

C.2.1 Flamelets formulation

In order to include heat loss effects in the manifold, the flame enthalpy have to be somehow controlled. In this section, it is presented a way to impose the enthalpy variation to the flamelets. Considering a free flame, the flamelets with different levels of enthalpy are obtained changing the inlet temperature and the inlet mass fraction composition.

Flamelets using free flames

Planar, laminar, freely-propagating, premixed, adiabatic flames are solved through the specialized software Chem1D [van Oijen, 2002; Chem1D, nd]. It solves different types of flames which are based on the finite volume method in a one-dimensional domain. The conservation equations, neglect curvature, stretch and tangential diffusion. The present work also assumes unity Lewis number and steady-state regime. The continuity equation then reads:

$$\frac{\partial m}{\partial s} = 0, \quad (\text{C.1})$$

where m [kg/m^2s] is the mass burning rate and s [m] is the distance perpendicular to the flame surface. The species transport equation is given by

$$\frac{\partial(mY_i)}{\partial s} - \frac{\partial}{\partial s} \left(\frac{\lambda}{c_p} \frac{\partial Y_i}{\partial s} \right) = \dot{w}_i, \quad i = 1, N_s - 1 \quad (C.2)$$

The specific enthalpy h [J/kg] is represented by

$$\frac{\partial(mh)}{\partial s} - \frac{\partial}{\partial s} \left(\frac{\lambda}{c_p} \frac{\partial h}{\partial s} \right) = 0. \quad (C.3)$$

The boundary conditions imposed to solve the equations (C.1)-(C.3) are shown on the Table C.1.

Unburnt Side (<i>Left</i>)	Burnt Side (<i>Right</i>)
$Y_i(-\infty) = Y_i$	$\frac{\partial Y_i}{\partial s}(\infty) = 0$
$h(-\infty) = h$	$\frac{\partial h}{\partial s}(\infty) = 0$
$u(-\infty) = m/\rho(-\infty)$	

Table C.1 – Boundaries condition imposed to solve a free flame.

The mass burning rate (m) is an eigenvalue of the problem and the solution of the set of equations (C.1) - (C.3) is called a flamelet. The Chem1D uses an exponential finite-volume discretization in space and the set of equations are solved using a fully implicit, modified Newton technique [Somers, 1994]. The grid is adaptative to increase the resolution around the flame front. Details about how the one-dimensional flamelet equations are derived can be accessed in de Goey and ten Thijs Boonkcamp [1997] and de Goey and ten Thijs Boonkcamp [1999].

C.2.2 Tabulation

In this study, two control variables are employed, the progress variable (\mathcal{Y}) and the enthalpy (h). Figure C.2 presents a schematic space created by the ensemble of flamelets (f_1, f_2, f_3 and f_n). For each combination of \mathcal{Y} and h one thermochemical variable value $\xi(\mathcal{Y}, h')$ is associated. These thermochemical variables may be temperature (T), mass fractions (Y_i), dynamic viscosity (μ), etc. The information is stored in a database also known as a manifold. When the exact value is not found on the manifold, it is used a

bilinear interpolation procedure is used to obtain the value.

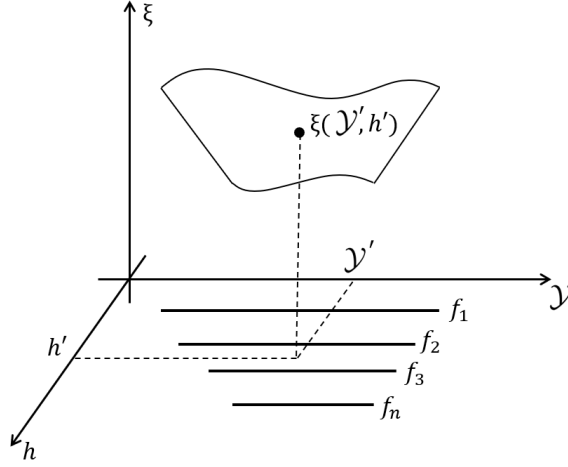


Figure C.2 – Schematic representation of space of generic thermochemical variable ξ as a function of progress variable (\mathcal{Y}) and enthalpy (h).

Reaction progress variable (\mathcal{Y})

The reaction progress variable is used to map the composition of the flame. Usually, the $\min(\mathcal{Y})$ is the fresh gases and the $\max(\mathcal{Y})$ is the burned gases. It does not have only one way to be defined, but Ihme et al. [2012] suggest some rules: (1) the definition should result in a transport equation possible to solve in a combustion modelling; (2) it should be independent from other CVs (control variables); (3) the reactive scalars from which progress variable is constructed should all evolve on comparable time scales; (4) it should result in unique point for each combination of control variables. In the present study, the \mathcal{Y} is defined using a sum of mass fractions weighted by the inverse of their molar masses:

$$\mathcal{Y} = \sum_{i=1}^{N_s} \alpha_i Y_i \quad \text{and} \quad \alpha_i = 1/MW_i. \quad (\text{C.4})$$

Enthalpy (h)

For predicting heat losses, the flamelets are solved for a range of enthalpy values, which implies that enthalpy becomes a control variable. The easiest way to change the mixture enthalpy is by changing its initial temperature. Thus, the flamelets are calculated for initial temperatures varying from T_{max} to T_{min} in steps of ΔT . The limitation of

T_{min} occurs because lower temperatures are not realistic (below than 240 K). In the literature, there are a couple of ways to solve this problem [van Oijen, 2002; Donini, 2014]. In the present work, we followed the approach of converting a fraction of the reactants (CH_4 and O_2) into the corresponding products (CO_2 and H_2O) at the same initial temperature. This conversion of species respects the fuel/oxidant stoichiometric proportion, thus, the enthalpy of the mixture is decreased, due to the low enthalpy of formation of the saturated products, while the pool of atoms of the mixture is preserved. Hence, we changed the composition, increasing the molar fraction of CO_2 (H_2O) in steps until the flame extinguishes.

The enthalpy range covered by the decrease of the initial temperature and the dilution of the reactants with products is shown in Figure C.3. Unfortunately, these two methods are not able to reproduce the cold states close to the walls, where reactions are negligible. For this region an extrapolation procedure is necessary [van Oijen, 2002]. Here the lowest enthalpy composition is approximated for the one point obtained from equilibrium calculations (cold equilibrium) imposing the initial composition equal to that obtained for the last flamelet solution with the maximum progress variable.

It is relevant to note that one of difference from the FGM technique implemented for laminar premixed flames stabilized in a slot burner and the implementation carried out in porous burners is related with enthalpy levels. Due to the gas preheating that occurs in the region that precedes the flame front, it is necessary to raise the superior enthalpy level of the database.

The final step of implementation is the database, as shown in table C.2. In the first column, the progress variable value is presented and the second is the enthalpy. In the other columns the transport variables and additional scalars are stored.

\mathcal{Y}	h	T	c_p	...
-0.687	-1.45e+05	400	1111	...
-0.679	-1.45e+05	411	1111	...
-0.670	-1.45e+05	422	1112	...
...
1.031	-2.99e+06	300	1117	...

Table C.2 – FGM database structure.

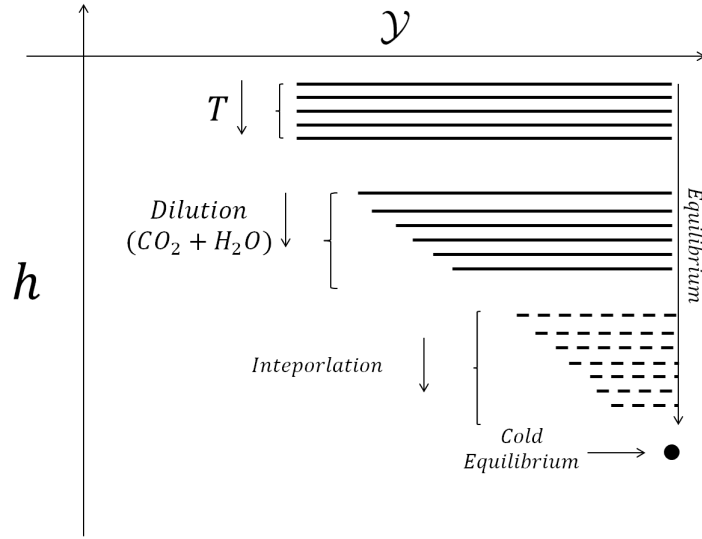


Figure C.3 – Schematic representation of 2D manifold with the different approaches for distinct regions.

Bi-linear interpolation

To retrieve the data from the database, it is used a bi-linear interpolation. Consider a point in a bi-dimensional domain coordinate (x,y) , which has a value $f(x,y)$ that needs to be interpolated, as shown in Figure C.4. The rectangle formed by four points could be divided into four sub-rectangles. The area of rectangle and sub-rectangles were defined as A_t and $w_{01}, w_{10}, w_{01}, w_{11}$, respectively. It is possible to show that

$$f(x,y) = \frac{w_{00}f_{00} + w_{01}f_{01} + w_{10}f_{10} + w_{11}f_{11}}{A_t}. \quad (\text{C.5})$$

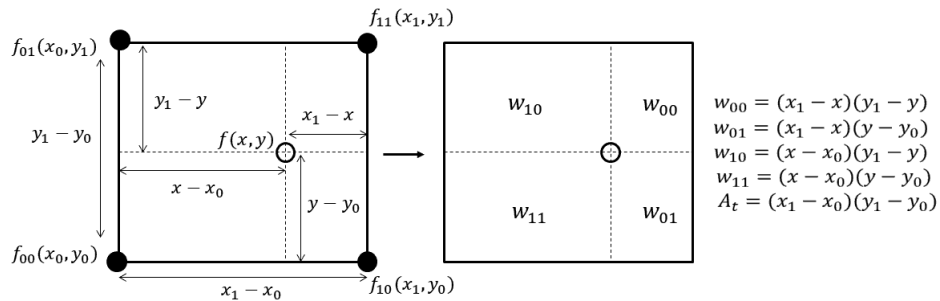


Figure C.4 – Illustration of bi-dimensional interpolation.

During the run-time, the fields of \mathcal{Y} and h are calculated by their conservation

equations. With the pair (\mathcal{Y}, h) , it is possible to obtain the value of each scalar of interest, after, this bi-linear interpolation is applied. The algorithm is developed using User-Defined Functions (UDFs).

C.2.3 Multidimensional simulation

In addition of continuity and momentum equations, transport equations for the progress variable and for the enthalpy are introduced

$$\frac{\partial}{\partial x_i} \left(\rho u \mathcal{Y} - \frac{\lambda}{c_p} \frac{\partial \mathcal{Y}}{\partial x_i} \right) = \dot{\omega}_{\mathcal{Y}} \quad (\text{C.6})$$

and

$$\frac{\partial}{\partial x_i} \left(\rho u h - \frac{\lambda}{c_p} \frac{\partial h}{\partial x_i} \right) = 0 \quad (\text{C.7})$$

where $\lambda [W/mK]$ and $c_p [J/kgK]$ is the thermal conductivity and specific heat, respectively. The $\dot{\omega}_{\mathcal{Y}}$ is source term of the progress variable, $u [m/s]$ is the velocity component and $\rho [kg/m^3]$ is defined as the density. These two equations are solved in place of the $(N_s - 1)$ species conservation and energy equations required by the detailed mechanism. The equation system for multidimensional simulations is solved by CFD software.

APPENDIX D – Flowchart of FGM implementation in a porous burner

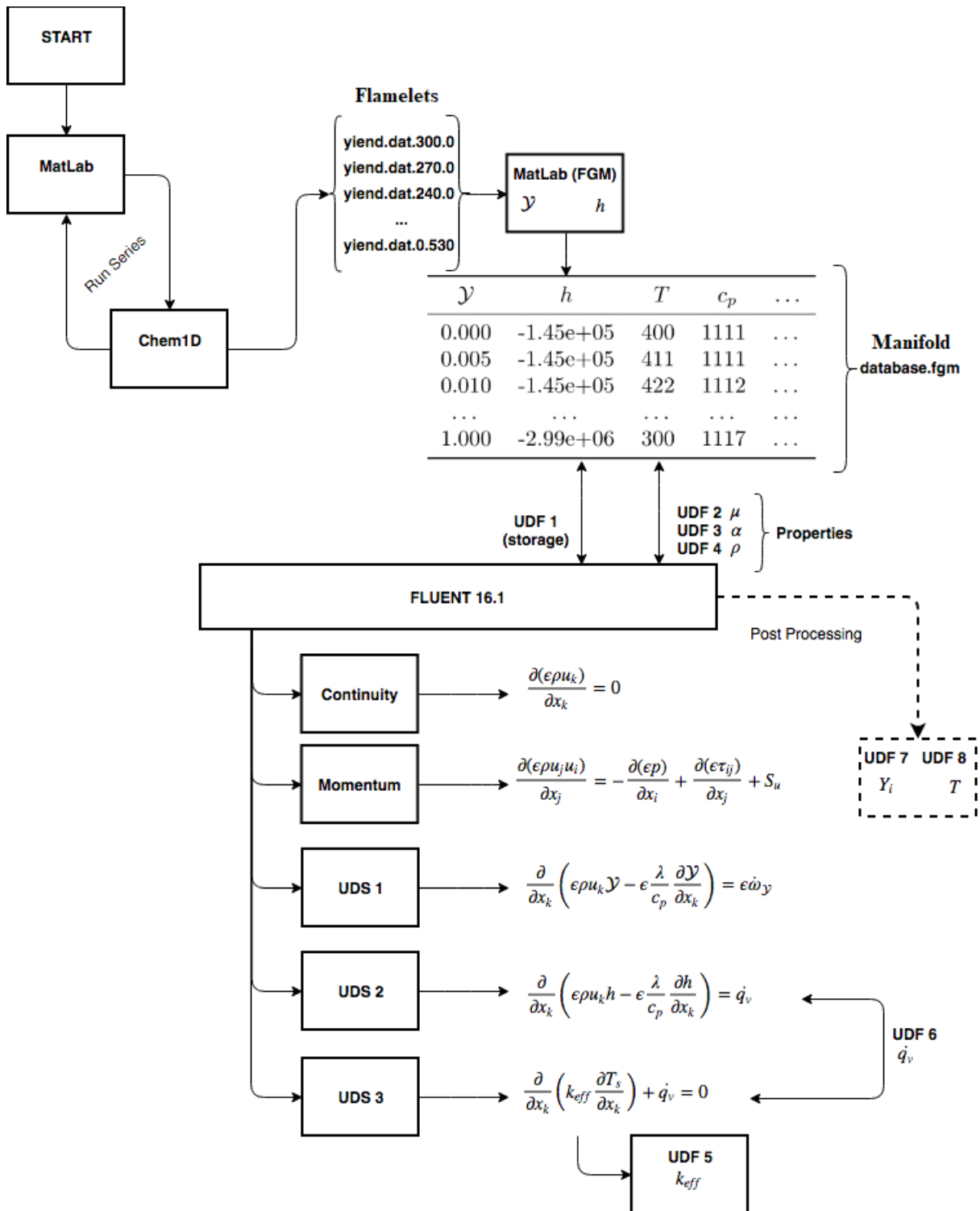


Figure D.1 – Flowchart of FGM implementation.

APPENDIX E – Mesh evaluation

The computational domain is discretized with quadrilateral cells as presented in Figure E.1 (a). The gas temperature with different levels of discretization are presented in Figure E.1 (b). The evaluation is conducted for five different meshes from $\Delta x = 0.5 \text{ mm}$ to 0.0313 mm . These sizes are considered in the axis region because close to the walls, the volumes considered are even smaller. The mesh with $\Delta x = 0.0625 \text{ mm}$ is chosen.

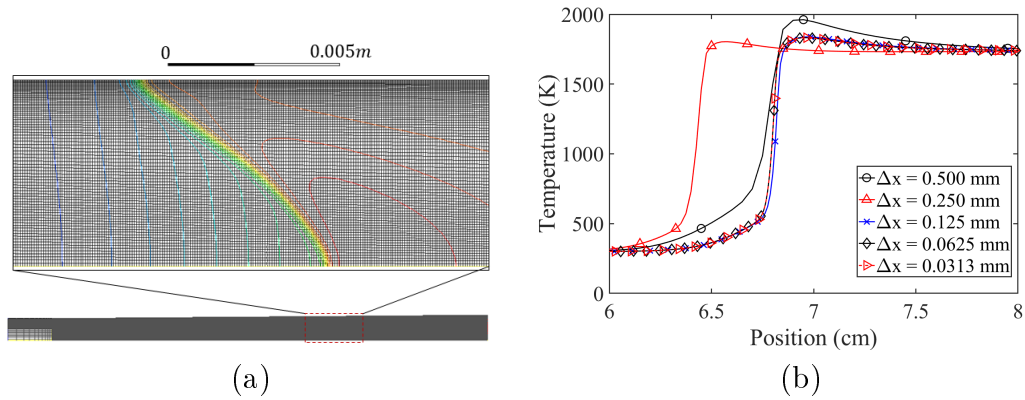


Figure E.1 – Mesh evaluation, (a) generated mesh with 35000 volumes, (b) gas temperature results imposing different mesh refinement. Simulation test with VPB imposing $v_{in}/S_l = 4.30$ and $\phi = 0.65$.

APPENDIX F – Curriculum Vitae

André Carlos Contini - andrecarloscontini@gmail.com

2000-2002	High School, E. E. Prof. Irmã Teofânia, Garibaldi/Brazil
2004-2007	B.Sc. Physics, UFRGS, Porto Alegre/Brazil
2008-2011	M.Sc. Metallurgical Engineering, UFRGS, Porto Alegre/Brazil
2016-2021	Ph.D. Mechanical Engineering, UFRGS, Porto Alegre/Brazil

Publications and Preprints

- 1 - Contini, A.C. and Pereira, F. M. Numerical study of flame stability within inert porous burner media subjected to flow oscillations, (*to be submitted*), 2022.
- 2 - Contini, A.C. and Pereira, F. M. Numerical study of flame stability within inert porous burner media with graded geometrical properties, (*to be submitted*), 2022.
- 3 - Contini, A.C., Donatti, L.S., Hoerlle, C.A., Zimmer, L., Pereira, F. M. Numerical study of the laminar premixed flame stabilization on a slot burner: comparison between detailed and FGM models. J Braz. Soc. Mech. Sci. Eng. 42, 189 (2020). <https://doi.org/10.1007/s40430-020-2267-9>.
- 4 - Silva, F. N. R. ; Hoerlle, C. A. ; Contini, A. C. ; Pereira, F. M. . Implementation of heat loss modeling for laminar diffusion CH_4 flames in the FGM method. In: COBEM, 2019, Uberlandia.
- 5 - Donatti, L. S. ; Contini, A. C. ; Hoerlle, C. A. ; Zimmer, L. ; Maders, L. ; Pereira, F. M. . Implementation of the flamelet-generated-manifold for premixed laminar flames with heat loss. In: Encit, 2018, Águas de Lindóia.
- 6 - Contini, A. C.; Zimmer, L. ; Hoerlle, C. A. ; Maders, L. ; Pereira, F. M. . Implementation of the Flamelet Generated Manifold (FGM) for premixed turbulent flames. In: COBEM, 2017, Curitiba.